

FACULTY FOR PHYSICS AND ASTRONOMY

UNIVERSITY OF HEIDELBERG

Diploma Thesis

in Physics
submitted by

Robert Grajcarek

born in Krasnik, Poland

2009

**Feasibility study on determining the average radiation thickness
 X/X_0 of the ALICE Transition Radiation Detector from CERN
testbeam data**

This diploma thesis has been carried out by Robert Grajcarek at the
Physikalisches Institut
under the supervision of
Helmholtz Young Investigator
Dr. Kai Schweda

Feasibility study on determining the average radiation thickness X/X_0 of the ALICE Transition Radiation Detector from CERN testbeam data

The Transition Radiation Detector (TRD) is a subdetector of the ALICE experiment at the LHC identifying electrons with momenta above 1 GeV/ c . Its effective radiation thickness serves as an essential input for physics analyses. By measuring the energy distribution of electrons after traversing the TRD, it is in principle possible to determine the average radiation thickness.

In this thesis data from a testbeam with several fixed momenta in a range of $p = 0.3$ GeV/ c to $p = 6.0$ GeV/ c at the Proton Synchrotron at CERN (PS) with tagged electrons and pions impinging on one of the eighteen supermodules of the TRD has been analyzed. The resulting electron energy has been measured by a lead glass Cherenkov calorimeter. In order to fully describe the data, detailed Monte Carlo simulations were performed. The result for the lower limit of the radiation thickness X/X_0 is $X/X_0^{\text{low}} = 18\%$ and for the upper limit $X/X_0^{\text{up}} = 39\%$.

Studie über die Möglichkeit einer Bestimmung der effektiven Strahlungsdicke des Übergangstrahlungsdetektors (Transition Radiation Detector, TRD) aus Teststrahlendaten aufgenommen am CERN

Der TRD (Transition Radiation Detector) ist ein Subdetektor des ALICE Experiments am LHC, der Elektronen mit Impulsen oberhalb von 1 GeV/ c identifiziert. Seine effektive Strahlungsdicke dient als unverzichtbarer Input für physikalische Analysen. Misst man die Energieverteilung der Elektronen nach Durchqueren des TRD, ist es prinzipiell damit möglich, die effektive Strahlungsdicke zu bestimmen.

In dieser Diplomarbeit wurden Daten vom Proton-Synchrotron (PS) am CERN eines neuartigen Teststrahls aus Pionen und Elektronen mit festen Impulsen im Bereich von $p = 0.3$ GeV/ c bis $p = 6.0$ GeV/ c , der durch ein von insgesamt achtzehn Supermodulen des TRD geschossen wurde, analysiert. Die Energie der Elektronen nach Durchqueren des TRD wurde mit einem Bleiglas-Cherenkov Kalorimeter gemessen. Um die Daten vollständig zu beschreiben, wurden detaillierte Monte-Carlo Simulationen durchgeführt. Das Ergebnis für die untere Grenze der Strahlungsdicke X/X_0 ist $X/X_0^{\text{low}} = 18\%$ und für die obere Grenze $X/X_0^{\text{up}} = 39\%$.

Contents

1	Introduction	1
2	Interaction of particles and matter	4
2.1	The Bethe-Bloch Formula	5
2.2	Energy loss of electrons and positrons	7
2.2.1	Modified Bethe-Bloch Formula	7
2.2.2	Bremsstrahlung	8
2.2.3	Properties of Bremsstrahlung radiation	11
2.3	Energy loss of photons	13
2.4	Energy loss of hadrons	15
2.5	Transition radiation	17
2.6	Cherenkov radiation	18
3	Particle detectors	20
3.1	Calorimeters	20
3.2	Cherenkov detectors	24
4	The Large Hadron Collider	26
5	The Transition Radiation Detector	29
5.1	The TRD working principle	30
5.2	Estimated radiation length	31
6	Testbeam 2007 at CERN PS	35
6.1	Experimental setup	35
6.2	Data selection and analysis	38
6.2.1	Cherenkov data	39
6.2.2	Silicon strip detectors data	40
6.2.3	Lead glass calorimeter data	43
7	Simulation of the Testbeam data	52
7.1	Software framework	53
7.1.1	AliRoot	53
7.1.2	GEANT3	55
7.2	Simulated experimental setup	55
7.3	Results of the Monte-Carlo simulations	58
7.3.1	Fast simulation	59
7.3.2	Full simulation	61

8 Monte Carlo - data comparison	69
8.1 Fast simulation	70
8.2 Full simulation	73
9 Summary and Outlook	84
Bibliography	87

1 Introduction

Matter in nature is found in different aggregate states. Water for example occurs in liquid, gaseous or solid state. There are also exotic physical conditions of matter like the plasma state or the Bose-Einstein condensate. The aim of heavy-ion physics is to investigate different states of nuclear matter. Quantum Chromodynamics (QCD) predicts an exotic state of nuclear matter, the so called *quark gluon plasma* (QGP), at either very high temperatures, e.g. shortly after the Big Bang, or at very high densities, e.g. in neutron stars. In that phase of matter quarks and gluons are freed from their hadronic boundary forming a deconfined phase of matter. Such conditions can be achieved when ions of heavy elements like lead or gold collide in huge particle accelerators like the **R**elativistic **H**eavy **I**on **C**ollider (RHIC) with a center-of-mass energy of up to $\sqrt{s_{\text{NN}}} = 200$ GeV or the **L**arge **H**adron **C**ollider (LHC) with a center-of-mass energy of up to $\sqrt{s_{\text{NN}}} = 5.5$ TeV per nucleon-nucleon pair.

Quarkonia consisting of heavy quarks such as e.g. the J/ψ , a bound state of an c-quark and an \bar{c} -quark, play a key role in research for the quark gluon plasma. Frequent interactions at the partonic stage cause the c-quarks to participate in collective motion [1, 2, 3] and finally kinetically equilibrate. This lead to the idea of statistical hadronization of charm quarks [4] in the quark gluon plasma. Calculations predict significant changes in the production of the J/ψ [5]. In 1986, Satz and Matsui [6] suggested that the high density of gluons in a quark gluons plasma should destroy charmonium systems, in a process analogous to Debye screening of the electromagnetic field in a plasma through the presence of electric charges. However, more advanced models predict that after the destruction of the charmonium systems a (re)generation of them takes place either through statistical hadronization at the phase boundary [4, 7] or coalescence of charm quarks in the plasma [8, 9, 10, 11, 12]. The influence of this (re)generation process crucially depends on the initial amount of produced c-quarks in a collision. If the energy of the colliding ions is high as in case of the LHC, the number of produced charm-quark pairs is in the order of some tens to a few hundred per collision. If the produced charm quarks can propagate over substantial distance, which is only possible in the quark gluon plasma consisting of deconfined and thermalized partonic matter, the charm quarks from different pairs can combine to form a J/ψ . Under these conditions, J/ψ -production scales quadratically with the number of charm quark pairs [14]. Thus an enhancement of J/ψ -production in heavy-ion collisions with respect to J/ψ -production in proton-proton collision at high collision energies as at the LHC is predicted. An experimental observation of such an enhancement would be a clear signature of the formation of a quark gluon plasma. If the collision energy of the colliding ions is rather moderate as in case of RHIC, the (re)generation rate is low and a suppression of J/ψ -production is predicted and also observed (see Fig. 1.1). In order to compare J/ψ -production in proton-proton collisions and J/ψ -production in heavy-ion

collisions on an absolute scale, the value $R_{AA}^{J/\psi}$ is introduced. It is given by

$$R_{AA}^{J/\psi} = \frac{\frac{dN_{AA}^{J/\psi}}{dp_T dy}}{\langle N_{\text{coll}} \rangle \cdot \frac{dN_{pp}^{J/\psi}}{dp_T dy}}. \quad (1.1)$$

The value $R_{AA}^{J/\psi}$ in Eq. (1.1) denotes the ratio of J/ψ -production in heavy-ion collisions $dN_{AA}^{J/\psi}$ and proton-proton collisions $dN_{pp}^{J/\psi}$ per pseudorapidity and transverse momentum interval $dp_T dy$. The proton-proton yield is scaled by the averaged number of binary nucleon-nucleon collisions N_{coll} . Figure 1.1 shows the predictions within the statistical model [14] for the ratio $R_{AA}^{J/\psi}$ as a function of the number of participating nucleons N_{part}

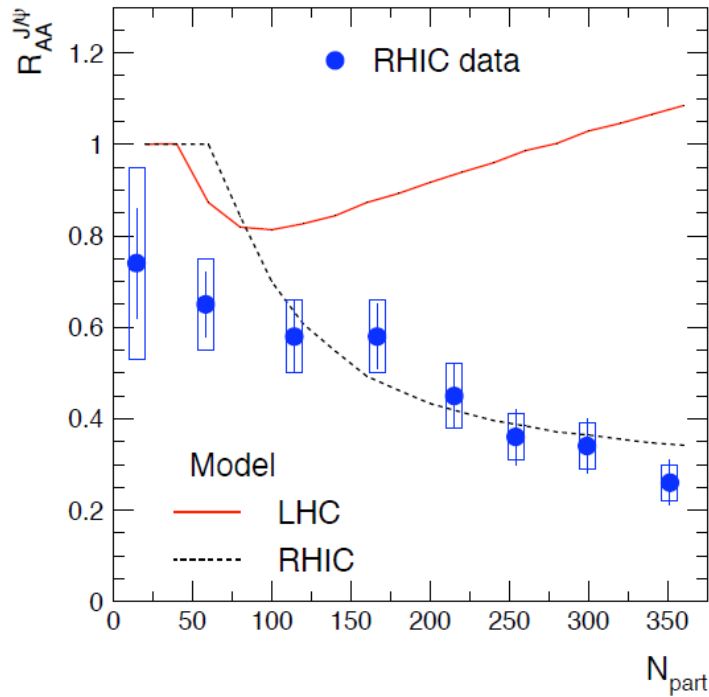


Figure 1.1: Statistical model predictions for J/ψ -production in heavy-ion collisions relative to proton-proton collisions as function of the number of participating nucleons for RHIC (black dashed line) and LHC (red solid line). The blue data points are for top RHIC energies as measured by the PHENIX collaboration [13]. This figure has been taken from [14].

in heavy-ion collisions. The dashed black line is a prediction for this ratio at a collision energy achieved at RHIC and the red solid line at the maximum collision energy that will be available at the LHC in the future. The blue data points have been measured by the PHENIX collaboration at RHIC. For a number of participating nucleons $N_{\text{part}} > 100$ the statistical model prediction is in good agreement with the RHIC data within the experimental accuracy.

A **L**arge **I**on **C**ollider **E**xperiment (ALICE) at the LHC was designed and constructed for investigations of lead-lead collisions and thus for studies of the quark gluon plasma. Besides a large number of decay products contributing to the understanding and characterization of

the quark gluon plasma, ALICE will measure e.g. the decay products of J/ψ . The ALICE **T**ransition **R**adiation **D**etector (TRD) measures the production of J/ψ by identifying electrons and positrons from electromagnetic decays over a large momentum range.

The physics analysis of the experimental data requires the knowledge of the detector efficiency. This efficiency is calculated with detailed Monte-Carlo simulations taking into account the detector geometry and the response function of the detector electronics. An essential ingredient to the Monte-Carlo simulations is the precise knowledge of the material budget each particle experiences when traversing the detector. The total material budget is commonly given in fraction of the radiation length X/X_0 , also called the radiation thickness X/X_0 . The aim of this thesis is to investigate, whether the radiation thickness X/X_0 of the ALICE Transition Radiation Detector is extractable from experimental data taken during the TRD Testbeam 2007 and thus measuring the contribution of the TRD to the full material budget of the ALICE-detector.

This thesis is organized as follows. Chapter 2 gives an overview of the relevant interactions of particles with the detector material, which are important for this thesis. Chapter 3 describes the working principle of Cherenkov detectors and calorimeters. During the Testbeam 2007 these two types of detectors were used for identification of electrons and for energy measurements. Chapter 4 summarizes basic facts about the LHC. Chapter 5 is dedicated to the Transition Radiation Detector of the ALICE-experiment. The working principle and an estimation of the material budget of the TRD are given. Chapters 6, 7, 8 and 9 describe the roadmap of the effort to determine the radiation thickness of the TRD. In Chap. 6 the analysis of the recorded data of the TRD Testbeam 2007 is described. Chapter 7 describes the development and the results of detailed Monte Carlo Simulations, which were performed in order to reproduce the obtained data of the Testbeam 2007 and thus to determine the radiation thickness of the TRD. In Chap. 8 the recorded experimental data of the Testbeam 2007 and Monte Carlo simulations are compared. A summary is given in Chap. 9 followed by an outlook suggesting an experiment, which allows for a precise measurement of the radiation thickness X/X_0 of the Transition Radiation Detector.

2 Interaction of particles and matter

The energy of particles relevant for this thesis ranges from some keV to some GeV. In this range, particles and their interactions can be subdivided by looking at their most important interaction processes with the detector material as described below. A schematic sketch of this subdivision is shown in Fig. 2.1. The most important property of a particle in context of particle detectors is its charge. Charged particles are traceable within an

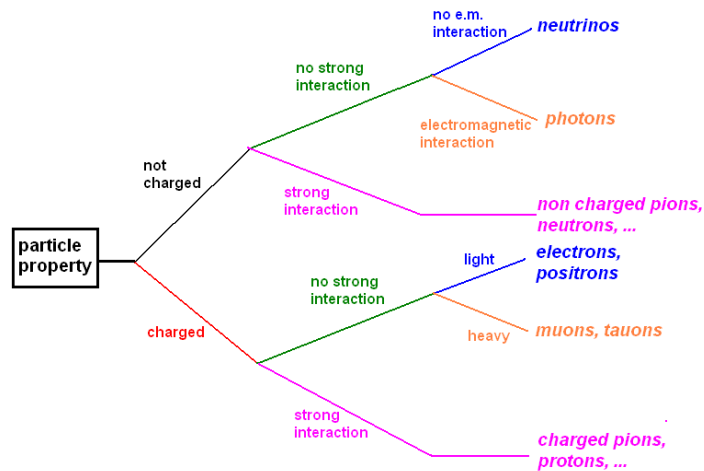


Figure 2.1: Schematic view of particles and their interactions with the detector material.

active detector volume since they ionize atoms along their path through the detector material. Neutral particles are not tracked but detected when they produce charged particles, e.g. a photon undergoing pair creation of a positron and an electron or a neutrino inducing an inverse β -decay within the detector material. Another important property is whether the considered particle experiences strong interaction. Strongly interacting particles such as neutrons or protons are detected in hadronic calorimeters in contrast to non-strongly interacting particles. Finally, charged particles are subdivided into heavy and light particles. In context of Bremsstrahlung, which is discussed in more detail below, electrons and positrons are light particles. All other particles are considered as heavy particles. This subdivision in context of Bremsstrahlung is due to the fact that for electrons and positrons Bremsstrahlung is an important energy-loss process, whereas energy-loss due to Bremsstrahlung is negligible for all other particles in the energy range relevant for this thesis.

2.1 The Bethe-Bloch Formula

Charged particles interact with the shell electrons of the atoms of the traversed material. The atoms are ionized or excited. This energy loss along the particle trajectories provides information for tracking in active detector materials. The process is described in the framework of quantum electrodynamics, resulting in a mean energy-loss rate given by the Bethe-Bloch Formula [15]

$$-\frac{dE}{dx} = K z^2 \frac{Z}{A} \frac{1}{\beta^2} \left[\ln \frac{2m_e c^2 \beta^2 \gamma^2}{I} - \beta^2 - \frac{\delta}{2} \right] \quad (2.1)$$

with $K = 4\pi N_A r_e^2 m_e c^2$, r_e denoting the classical electron radius, ze the charge of the incident particle, N_A Avogadro's number, Z the atomic number of the absorber, A the atomic mass of absorber, β the relativistic velocity, γ the Lorentz-factor, c the speed of light, m_e the electron mass, I the mean excitation energy and δ the density effect correction to ionization energy loss.

This formula has a minimum at around $\beta\gamma \approx 3.5 \pm 1$ for all target materials. A value of $\beta\gamma = 3.5$ corresponds to different momenta for each particle due to different rest masses. In Fig. 2.2 the mean energy loss as a function of $\beta\gamma$ ($= p/mc$) is shown for a number of particle species propagating in media with different atomic numbers Z and atomic masses A . The highly energetic part of the energy distribution for a value of $\beta\gamma > 4$

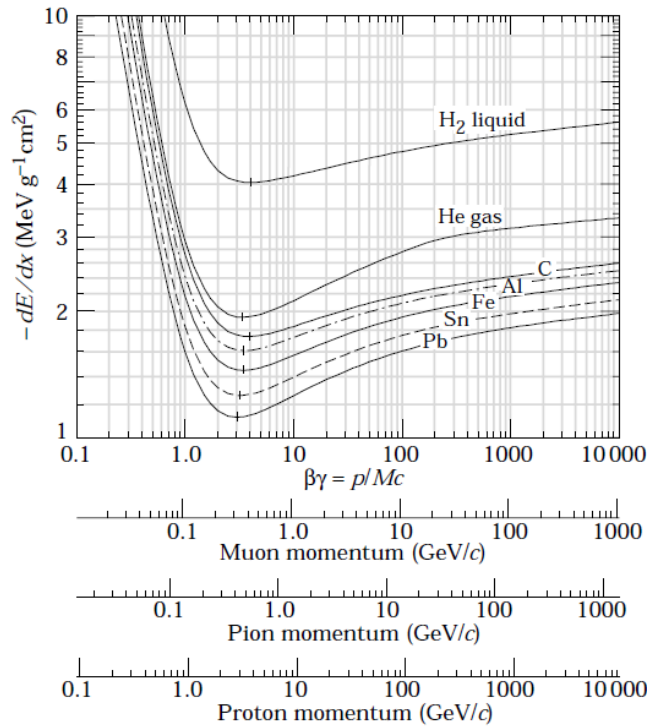


Figure 2.2: Mean energy loss for different materials and particle species as a function of $\beta\gamma$. This figure has been taken from [16].

is weakly dependent on the momentum of a particle. In this part the energy loss of a

particle increases at most a factor of 1.7 over several decades of momentum and levels off at a constant value - the Fermi Plateau. In this momentum range the main energy loss of pions and protons is due to hadronic processes and not due to ionization anymore. Muons remain over several decades of their momentum range so called minimum ionizing particles and Bremsstrahlung processes become important for them only at very high momenta, namely for $p > 1 \text{ TeV}/c$. Electrons and positrons, however, behave differently because their energy loss is modified due to indistinguishability of projectile and target in case of electrons and due to radiative processes, which start to dominate for both electrons and positrons at rather moderate momenta, namely for $p > \text{few MeV}/c$. This radiative processes are described in more detail in Sec. 2.2.

Knock-on electrons (δ -rays)

The energy loss formula given in Eq. (2.1) due to ionization represents a mean value. In reality, there exists a certain probability distribution around the most probable energy loss value. In case of thick absorbers this is a Gaussian function. However, in case of thin absorbers so called *knock-on electrons* become important and the probability distribution is modified. These are electrons which are scattered with small scattering angles at the incident charged particle and therefore carry away a large fraction of the incident energy. The energy spectrum of these knock-on electrons is given by [16]

$$\frac{dN}{dE_{kin}} = \xi \cdot \frac{F(E_{kin})}{E_{kin}^2} \quad ; \quad \text{for } I \ll E_{kin} \leq E_{kin}^{max} \quad (2.2)$$

with ξ see Eq. (2.4), F denoting a spin dependent factor, which is ≈ 1 for $E_{kin} \ll E_{kin}^{max}$ and for I see Eq. (2.1).

E_{kin}^{max} is the maximum energy that can be imparted on a shell electron. In case of an incident electron it is half the kinetic energy because of the indistinguishability of projectile and target. In case of all other charged particles E_{kin}^{max} is given by

$$E_{kin}^{max} = \frac{E^2}{E + \frac{1}{2} \cdot \frac{m_0}{m_e} \cdot m_0 c^2} \quad (2.3)$$

with m_0 the mass of the incident particle.

Hence, only for $E \gg \frac{1}{2} \frac{m_0}{m_e} m_0 c^2$ the incident particle can impart its full energy on the shell electron.

Because of frequent high energy deposits in thin absorbers caused by the knock-on electrons described above the probability distribution changes from a Gaussian function to a Landau distribution. There does not exist an analytical solution for the Landau distribution, but an acceptable approximation for it is given by [28]

$$L(\lambda) = \frac{1}{\sqrt{2\pi}} \cdot \exp \left\{ -\frac{1}{2} \left(\lambda + e^{-\lambda} \right) \right\} \quad (2.4)$$

with L denoting the probability, $\lambda = \frac{\Delta E - \Delta E^{MPV}}{\xi}$, ΔE the real energy loss in absorber with thickness Δx , ΔE^{MPV} the most probable energy loss in absorber with thickness Δx , $\xi = 2\pi N_A r_e^2 m_e c^2 z^2 \frac{Z}{A} \cdot \frac{1}{\beta^2} \cdot \rho \cdot \Delta x$.

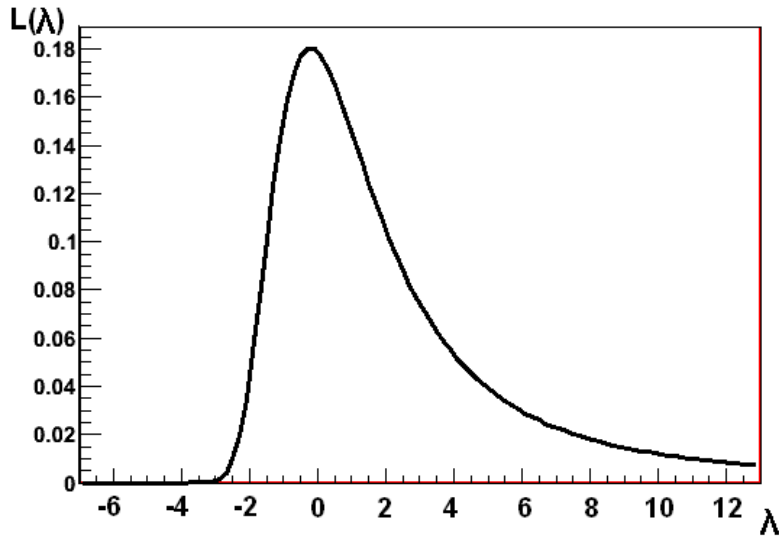


Figure 2.3: Landau distribution.

An example for a Landau distribution is shown in Fig. 2.3 for a realistic set of parameters the parameter ξ in Eq. (2.4) depends on. In contrast to a symmetric Gaussian function the Landau distribution consists of a peak at $\lambda = 0$ and a long branch extending to high values of λ caused by knock-on electrons.

2.2 Energy loss of electrons and positrons

Since energy-loss processes for electrons and positrons play a key role in this thesis, a detailed section is dedicated to their interaction with matter. In the following, some basic distributions and formulae concerning different energy-loss processes of electrons and positrons such as ionization or Bremsstrahlung are discussed.

2.2.1 Modified Bethe-Bloch Formula

The energy loss of electrons and positrons due to ionization has to be treated differently than the energy loss of heavy particles. The reason for this is the low mass of electrons and positrons which is identical with the mass of the shell electrons. Therefore, spin-spin interactions have to be taken into account and the kinematics is different than in the case of an incident heavy particle. Moreover, in case of electrons the incident and the shell electron are indistinguishable. For positrons, the positron annihilation process also contributes. If all contributions except Bremsstrahlung are considered, rather complicated formulae for the energy loss are the consequence, which are given in [17, 18]. They are not given here because they are very complicated and do not contribute to the understanding of the energy loss of electrons/positrons due to ionization. Instead of that Fig. 2.4 illustrates qualitatively the different contributions to the total energy loss of positrons and electrons. According to Fig. 2.4 the main energy loss above an energy of some tens of MeV is Bremsstrahlung. This is discussed in more detail in the next subsection.

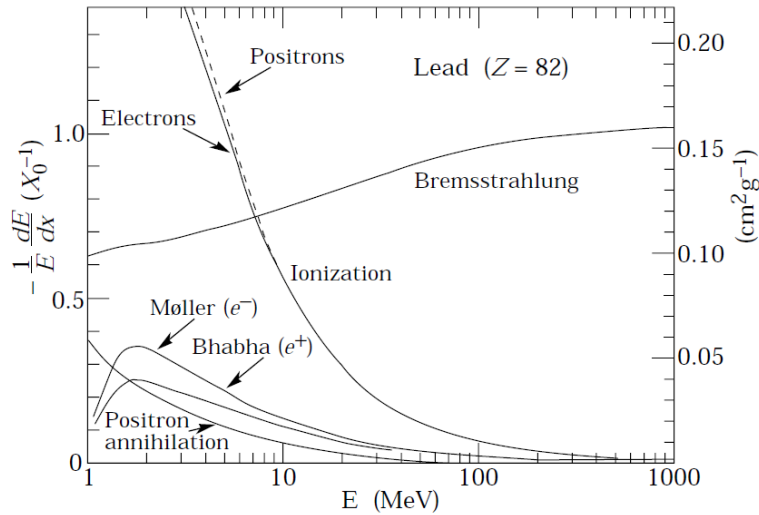


Figure 2.4: Fractional energy loss per radiation length in lead as a function of the electron or positron energy. This figure has been taken from [16].

2.2.2 Bremsstrahlung

Fast charged particles interact with the electromagnetic field of the nucleus and lose energy by emitting photons. This process is called *Bremsstrahlung* and becomes the main energy loss mechanism for electrons and positrons above some tens of MeV for heavy target materials with electric charge $Z > 10$. For all other charged particles this process is negligible over many decades of energy range and becomes important not until very high energies, namely for $E > 1 \text{ TeV}/c$. The Feynman graph for Bremsstrahlung is shown in Fig. 2.5. According to this graph, the incident electron/positron exchanges a virtual

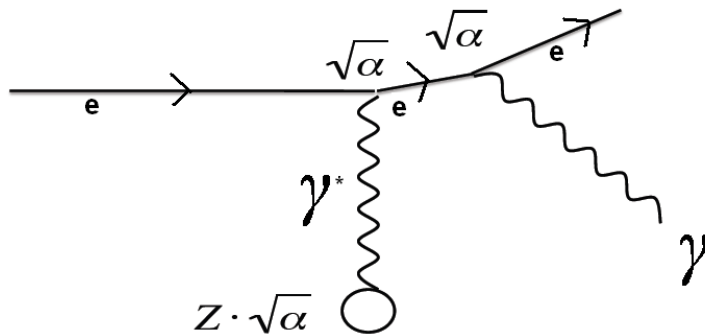


Figure 2.5: Feynman graph depicting the Bremsstrahlung process. This figure has been taken from [19].

photon with the target nucleus and then emits a real photon. The exchange of the virtual photon is necessary, so that energy and momentum are conserved. The cross section for

Bremsstrahlung and the energy loss is therefore proportional to Z^2

$$M \propto \sqrt{\alpha} \cdot \sqrt{\alpha} \cdot Z \cdot \sqrt{\alpha} = Z \cdot \alpha^{3/2} \rightarrow P \propto |M|^2 \propto Z^2 \alpha^3. \quad (2.5)$$

with M denoting the transition matrix, P the transition probability, Z the atomic number of absorber and α the fine structure constant.

However, the incident electron does not only interact with the electromagnetic field of the nucleus but also with the electromagnetic field of the shell electrons. Moreover, the nucleus is screened by the shell electrons. Therefore the incident electron experiences a screened nucleus charge. The influence of the screening effect depends on the energy of the incident electron. Generally, the energy loss due to Bremsstrahlung is parameterized by the following formula [21]

$$-\frac{dE}{dx} = 4\alpha \frac{N_A}{A} r_e^2 \cdot E \cdot \left[Z^2 \Phi_{rad}^{(n)} + Z \Phi_{rad}^{(e)} \right] \quad (2.6)$$

with E denoting the energy of the incident electron, $\Phi_{rad}^{(n)}$ the nucleus scattering contribution including the screening effect and $\Phi_{rad}^{(e)}$ the shell electrons scattering contribution. There is no expression for the energy loss due to Bremsstrahlung in the literature that covers the whole energy range because the two contributions $\Phi_{rad}^{(e)}$ and $\Phi_{rad}^{(n)}$ in Eq. (2.6) depend on energy. An expression often used for highly energetic electrons with $E > 100$ MeV is given by [29]

$$-\frac{dE}{dx} = 4\alpha N_A \cdot \frac{Z^2}{A} \cdot E \cdot \ln \frac{183}{Z^{1/3}}. \quad (2.7)$$

This formula can also be written as

$$-\frac{dE}{dx} = \frac{E}{X_0}. \quad (2.8)$$

Integration of the formula gives

$$E(x) = E_0 \cdot e^{(-x/X_0)}. \quad (2.9)$$

The variable X_0 , which is defined by the formula given in Eq. (2.7), is known as the *radiation length* and defines the path length of traversed material after which the initial energy E_0 of the incident electron or positron is reduced by a factor e^{-1} . Since Eq. (2.7) is only an approximation, it is clear that the radiation length X_0 depends on which formula is used for the energy loss. The formula most often used for the radiation length is the formula of Tsai [34]. Calculated values for some materials are given in Tab. 2.1. The formula depends on the target material and will not be given here. Instead of, a good fit to it is given here by [16]

$$X_0 = \frac{716.4 \text{ g cm}^{-2} \cdot A}{Z(Z+1) \ln(287/\sqrt{Z})}. \quad (2.10)$$

This fit agrees with Tsai's values to better than 2.5% for all target elements except helium, where the result is about 5% low.

Another important parameter for Bremsstrahlung is the *critical energy*. It is the energy

Material	Z	A	X_0 [g/cm^2]	ρ_0 [g/cm^3], [g/l] for gases
Hydrogen	1	1.0	63.04	0.071
Helium	2	4.0	94.32	0.169
Carbon (graphite)	6	12.0	42.70	2.21
Nitrogen	7	14.0	37.99	0.807
Aluminium	13	27.0	24.01	2.699
Oxygen	8	16.0	34.24	1.141
Iron	26	55.8	13.84	7.874
Lead Glass	-	-	7.87	6.220
Copper	29	63.5	12.86	8.960

Table 2.1: Radiation length of different materials [16].

at which energy loss due to Bremsstrahlung starts to exceed the energy loss due to ionization. As shown in Fig. 2.4 for lead this happens at around 10 MeV where the ionization curve and the Bremsstrahlung curve intersect. Seltzer and Berger [20] give the following approximation for the critical energy

$$E_c = \frac{800 \text{ MeV}}{Z + 1.2}. \quad (2.11)$$

Rossi [22] gives 2 different approximations for gases and solids and both are shown in Fig. 2.6. As in case of ionization, the energy loss given in Eq. (2.7) due to Bremsstrahlung

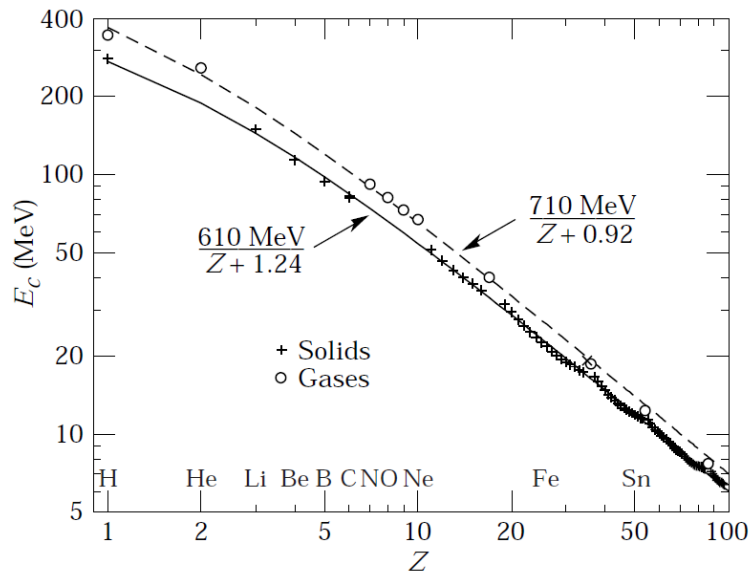


Figure 2.6: Critical energy of electrons for the chemical elements according to Rossi. This figure has been taken from [16].

is just a mean value. The energy-loss straggling-function for a given energy loss ΔE and absorber thickness Δx has been calculated by Bethe and Heitler [18] using an approximate

expression for the Bremsstrahlung cross-section

$$f(\Delta x, \Delta E) = \frac{1}{\Gamma(c)} \left(-\ln \left(\frac{E_0 - \Delta E}{E_0} \right) \right)^{c-1} \quad (2.12)$$

with E_0 denoting the energy of incident electron, $c = \frac{\Delta x}{X_0 \ln 2}$.

This function is plotted in Fig. 2.7 for different absorber thicknesses as a function of the parameter $z = \frac{E_0 - \Delta E}{E_0}$. The curve is sensitive to the so-called *radiation thickness* $X/X_0 = \Delta x/X_0 = c \cdot \ln 2$. A clear rise of the probability $f(z)$ for $z < 1$ is noticeable if the radiation thickness X/X_0 is enhanced. This curve is feasible for an experimental

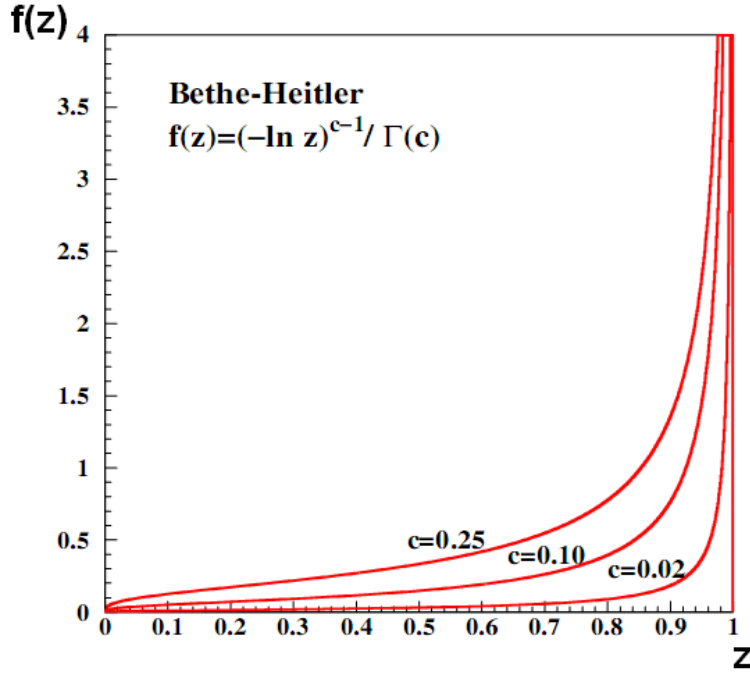


Figure 2.7: The Bethe-Heitler energy-loss straggling-function for different absorber thicknesses. The meaning of z is: $z = \frac{E_0 - \Delta E}{E_0}$. This figure has been taken from [27].

determination of the radiation thickness X/X_0 of a block of material by fitting it to a measured energy distribution of electrons/positrons after traversing this block. The radiation thickness X/X_0 is a free fit parameter within Eq. (2.12) in this case and the value of X/X_0 is determinable by applying a standard fit procedure. This works only if the energy of the impinging electrons/positrons is well above the critical energy (see Fig. 2.6) and thus the energy-loss due to ionization is negligible.

2.2.3 Properties of Bremsstrahlung radiation

When computing the spectrum of the emitted Bremsstrahlung photons, the differential cross section for Bremsstrahlung $\frac{d\sigma}{dk}$, whereas k denotes the energy of the emitted photon, has to be calculated. As shown in Eq. (2.6), the cross section depends on the energy of the incident electron. Seltzer and Berger [20, 21] have calculated and tabulated the cross

sections for an electron energy range of 10 keV to 10 GeV. In their papers they refer amongst others to Tsai [34] who gives an approximation for the differential cross section for high electrons energies $E > 100$ MeV

$$\frac{d\sigma}{dk} = \frac{A}{X_0 N_A k} \left(\frac{4}{3} - \frac{4}{3}y + y^2 \right) \quad (2.13)$$

with X_0 the radiation length as given in Eq. (2.7), k the energy of emitted photon, $y = \frac{k}{E}$, and E the energy of the incident electron.

In Fig. 2.8 the calculated Bremsstrahlung spectrum for incident electrons energies in the range of 10 GeV to 10 PeV is shown. According to this figure, the probability for emission of Bremsstrahlung photons carrying a large fraction of the incident electron energy rises with increasing electron energy. In other words, the spectrum becomes harder with rising incident electron energy. Tsai [34] also gives a formula for the double differential cross

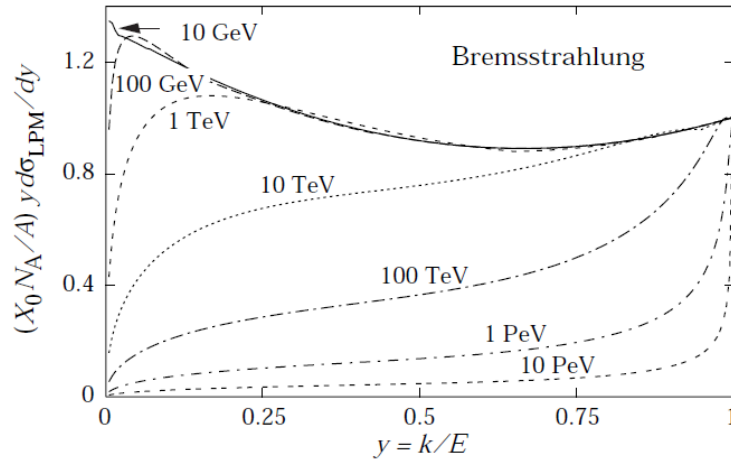


Figure 2.8: The normalized Bremsstrahlung cross section in lead versus the fractional photon energy $y=k/E$. The vertical axis has units of photons per radiation length. This figure has been taken from [16].

section of Bremsstrahlung in his paper. The first differential is dk as given in Eq. (2.13) and the second $d\Omega$, which is the solid angle when the photon is emitted. Thus, this formula describes the angular distribution of the emitted Bremsstrahlung photons with respect to the direction of the incident electron momentum. This formula given in [34] is rather lengthy and complicated and is not given here. According to this formula, the cross section depends only on the polar angle Θ and is independent of azimuth Φ . Hence, the Bremsstrahlung photons are emitted isotropically in Φ forming a cone. The probability distribution as a function of the polar angle Θ is shown in Fig. 2.9. This distribution was simulated with GEANT3 which uses the formula of Tsai [34] for sampling the polar angle Θ . The incident particles were 50.000 electrons with an energy of 1 GeV which traversed one supermodule of the ALICE Transition Radiation Detector (TRD) with an average radiation thickness of $X/X_0 \approx 25\%$. The TRD is described in Chap. 5. According to this distribution the polar emission angle Θ is rather small and 99% of the photons are emitted with a polar angle $\Theta < 1$ deg.. The FWHM of this distribution is in the order of 0.4 deg..

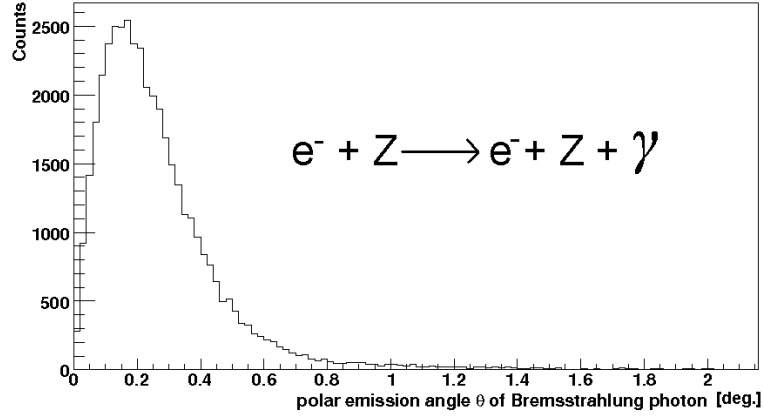


Figure 2.9: Polar angle Θ distribution for Bremsstrahlung photons, for $E_{\text{phot}} > 1$ MeV. This distribution was simulated with GEANT3 which uses the formula of Tsai [34] for sampling the angle Θ . The incident particles were 50.000 electrons with an energy of 1 GeV which traversed the material of the TRD with an averaged radiation thickness of $X/X_0 \approx 25\%$.

2.3 Energy loss of photons

Photons may lose their energy by three different processes.

- Photoelectric effect ($\gamma + \text{atom} \rightarrow \text{atom}^+ + e^-$). The photon disappears; this process dominates within the energy range of some eV to 100 keV.
- Compton effect ($\gamma + e^- \rightarrow \gamma' + e^-$). The photon is scattered and loses energy; this process dominates within the energy range of 100 keV to some MeV depending on the target material.
- Pair production ($\gamma + \text{atom} \rightarrow \text{atom} + e^+ + e^-$). The photon disappears; this process dominates above some MeV depending on the target material.

The cross sections for the processes can be found in the literature [22, 25, 26]. For small photon energies ($\epsilon = E_\gamma/m_e c^2 \ll 1$) the photoelectric cross section is given by [26]

$$\sigma_{\text{p.e.}} = \frac{8}{3} \pi r_e^2 \alpha^4 Z^5 \left(\frac{32}{\epsilon^7} \right)^{1/2}, \quad \text{for } \epsilon = E_\gamma/m_e c^2 \ll 1. \quad (2.14)$$

If the photon energy reaches values that match the excitation or ionization energies of the considered atom E_i , Eq. (2.14) has to be modified by a function $f(E_\gamma, E_\gamma^{E_i})$.

For high photon energies ($\epsilon \gg 1$) however, the photoelectric cross section is different

$$\sigma_{\text{p.e.}} = 4\pi r_e^2 Z^5 \alpha^4 \cdot \frac{1}{\epsilon}, \quad \text{for } \epsilon = E_\gamma/m_e c^2 \gg 1. \quad (2.15)$$

For both cases the cross section is strongly dependent on the atomic number of the absorber Z . It is proportional to Z^5 . Therefore, if an experimental setup requires efficient absorption of low energetic photons, materials with high Z , e.g. Xenon, are used. Another property of the photoelectric cross section is its strong dependency on the photon energy.

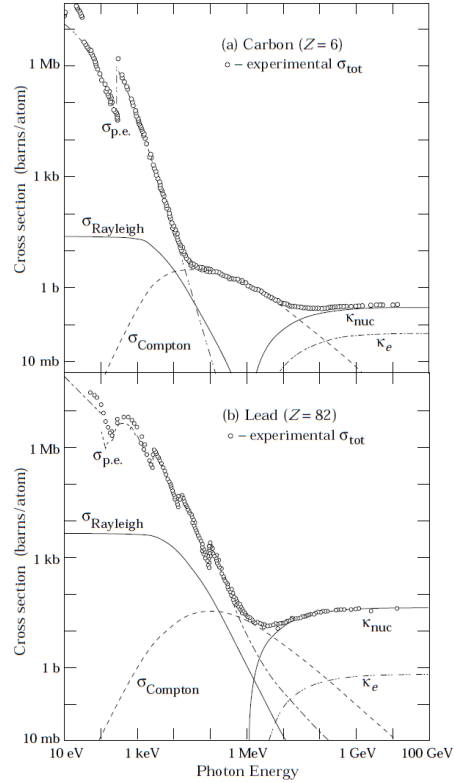


Figure 2.10: The total cross sections of photons as a function of energy in carbon and lead, showing the contributions of the photoelectric effect, Compton scattering and pair creation. The different processes and their energy dependency are described in the text. σ_{Rayleigh} , which is not explained in the text, is the cross section for elastic Rayleigh scattering during which photons do not lose any energy. This figure has been taken from [16].

For $\epsilon = E_\gamma/m_e c^2 \ll 1$ the cross section is proportional to $1/\epsilon^{3.5}$ and the dependency weakens for $\epsilon \gg 1$. In that energy range the cross section is proportional to $1/\epsilon$. The photon cross section as a function of energy is depicted in Fig. 2.10 for carbon in the upper part of the figure and for lead in the lower part. For energies well below 1 MeV the photoelectric cross section dominates and the strong dependency on the energy is visible. For photon energies around 1 MeV the cross section for Compton scattering dominates. According to Klein-Nishina [25], the cross section for Compton scattering is given by

$$\sigma_{\text{Compton}} = Z \cdot 2\pi r_e^2 \left[\left(\frac{1+\epsilon}{\epsilon^2} \right) \left\{ \frac{2(1+\epsilon)}{1+2\epsilon} - \frac{1}{\epsilon} \ln(1+2\epsilon) \right\} + \frac{1}{2\epsilon} \ln(1+2\epsilon) - \frac{1+3\epsilon}{(1+2\epsilon)^2} \right]. \quad (2.16)$$

This cross section is less dependent on the atomic charge Z in comparison to the photoelectric cross section. It is only proportional to the atomic charge Z . The energy dependence is rather complex and the cross section as a function of photon energy is depicted in Fig. 2.10. For photon energies well above 1 MeV pair production dominates. As in the case of the photoelectric effect, two energy regions have to be considered. Moreover, pair creation can occur in the electromagnetic field of the nucleus and in the electromagnetic field of the shell electrons. However, the latter case is strongly suppressed with respect to the former due to the rest mass difference between the shell electrons and the nucleus. Therefore cross sections for pair creation in the field of the nucleus will only be given here. For photon energies in the range $2 < \epsilon < \frac{1}{\alpha Z^{1/3}}$ the photon has to come near to the nucleus in order to perform pair production and therefore experiences the bare electromagnetic

charge of the nucleus. The cross section in this case is given by [25]

$$\kappa_{\text{nuc}} = 4\alpha r_e^2 Z^2 \left(\frac{7}{9} \ln(2 \cdot \epsilon) - \frac{109}{54} \right), \text{ for } 2 < \epsilon < \frac{1}{\alpha Z^{1/3}}. \quad (2.17)$$

For high photon energies ($\epsilon \gg \frac{1}{\alpha Z^{1/3}}$) pair production is also possible at large distances from the nucleus. In that case the photon experiences the screened nucleus charge. The cross section is given by

$$\kappa_{\text{nuc}} = 4\alpha r_e^2 Z^2 \ln \frac{183}{Z^{1/3}} \approx \frac{7}{9} \cdot \frac{A}{N_A} \cdot \frac{1}{X_0}, \text{ for } \epsilon \gg \frac{1}{\alpha Z^{1/3}}. \quad (2.18)$$

An advantage of this cross section is, that it is independent of the photon energy. Only the energy split among the produced e^-e^+ pair is energy dependent, as shown in Fig. 2.11. Finally, in order to compare the energy loss of photons and electrons, it is worth to men-

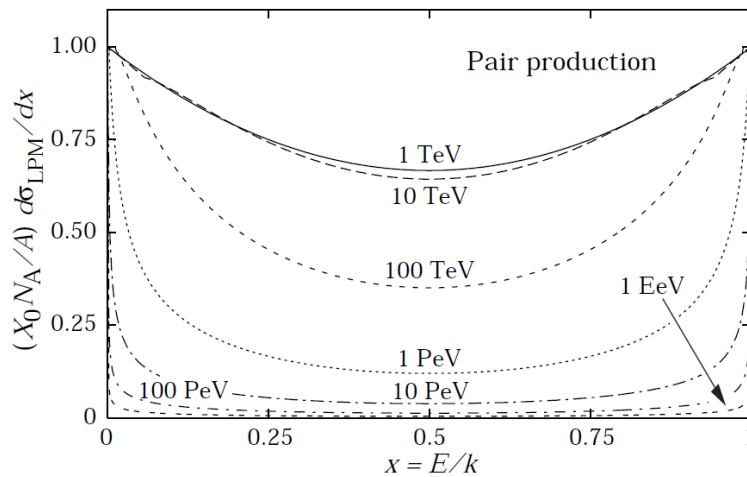


Figure 2.11: The normalized pair production cross section as a function of the fractional electron energy $x=E/k$ with k denoting the energy of incident photon and E the energy of the created electron and positron. For rising energy of the incident photon the probability for a symmetric split of the photon energy among the created electron and positron drops. For very high energies the energy of the incident photon is carried away either by the created electron or positron. This figure has been taken from [16].

tion that one radiation length X_0 of path length in a material of a highly energetic photon is around $\frac{7}{9}$ of its *mean free path* according to Eq. (2.18). The mean free path is the mean path length a highly energetic photon travels in an absorber material before it creates an electron positron pair and disappears. In Fig. 2.10 the cross sections for pair creation in the electromagnetic field of the nucleus κ_{nuc} and in the electromagnetic field of the shell electrons κ_e are depicted. Above some MeV both cross sections are independent of the photon energy according to Eq. (2.18).

2.4 Energy loss of hadrons

Charged hadrons lose energy due to ionization and due to hadronic interactions. Neutral hadrons lose energy only due to hadronic interactions. At high energies above some GeV

where charged hadrons are minimum ionizing particles, hadronic interactions dominate. In these terms it is not precise to call hadronic interactions an "energy-loss" mechanism. If a hadron undergoes an inelastic reaction with the traversed material, it might completely vanish and new hadrons are created. Hadronic interactions are complicated and so is the energy dependence of the cross sections.

The cross section of hadrons can roughly be separated in two parts

$$\sigma_{\text{total}} = \sigma_{\text{elastic}} + \sigma_{\text{inelastic}}. \quad (2.19)$$

The elastic cross section describes interactions without excitation of intrinsic degrees of freedom of hadrons. The inelastic cross section describes interactions during which kinetic energy is transferred to the intrinsic degrees of freedom of hadrons. In Fig. 2.12 the proton-antiproton elastic and total cross section as a function of energy are shown. If considering

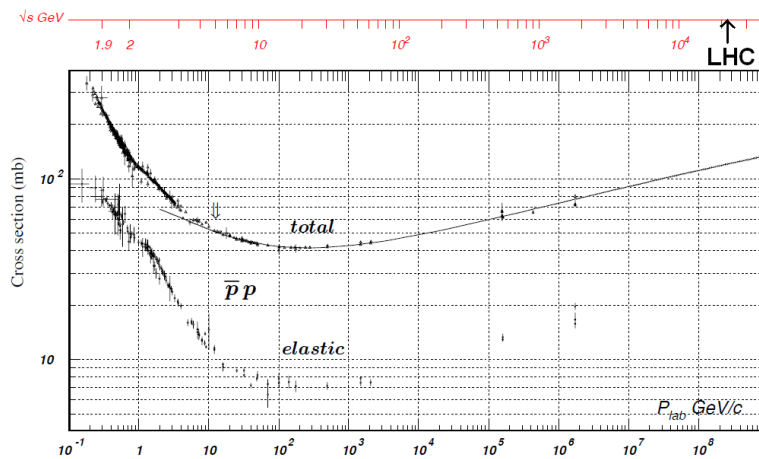


Figure 2.12: Proton-antiproton total and elastic cross section as a function of beam momentum (lower black abscissa) and as a function of center-of-mass energy (upper red abscissa). The center of mass energy available at the LHC in the future $\sqrt{s} = 14$ TeV is indicated at the upper red abscissa. This figure has been taken from [16].

a beam of highly energetic hadrons crossing some path length Δx in an absorber material, the initial number of hadrons N_0 in the beam decreases due to inelastic interactions during which hadrons interact with the material inelastically and disappear

$$N = N_0 \cdot e^{-\Delta x / \lambda_{\text{abs}}}, \quad (2.20)$$

where λ_{abs} is the path length after which the number of primary hadrons has decreased to a factor of e^{-1} because of inelastic interactions. It is called the *absorption length*, sometimes also the *interaction length*, and is defined by

$$\lambda_{\text{abs}} = \frac{A}{N_A \cdot \rho \cdot \sigma_{\text{inelastic}}}, \quad (2.21)$$

whereas the *collision length* is defined by

$$\lambda_{\text{coll}} = \frac{A}{N_A \cdot \rho \cdot \sigma_{\text{total}}}. \quad (2.22)$$

The *collision length* is the mean length after which a hadron interacts with the absorber material either elastically or inelastically. Tabular 2.2 summarizes both lengths $\lambda_{i,\text{neutrons}}$ in the energy range of 80 GeV to 200 GeV, where the two lengths are only weakly dependent on the energy, for neutrons for different materials. If comparing the radiation lengths in

Material	Z	A	$\lambda_{\text{abs}} \cdot \rho$ [g/cm ²]	$\lambda_{\text{coll}} \cdot \rho$ [g/cm ²]	ρ [g/cm ³]
Hydrogen	1	1.0	52.0	42.8	$0.071 \cdot 10^{-3}$
Helium	2	4.0	71.0	51.8	$0.169 \cdot 10^{-3}$
Carbon (graphite)	6	12.0	85.8	59.2	2.21
Nitrogen	7	14.0	89.7	61.1	$0.807 \cdot 10^{-3}$
Aluminium	13	27.0	107.2	69.7	2.699
Oxygen	8	16.0	90.2	61.3	$1.141 \cdot 10^{-3}$
Iron	26	55.8	132.1	81.7	7.874
Lead Glass	-	-	158.0	95.9	6.220
Copper	29	63.5	137.3	84.2	8.960

Table 2.2: Collision and interaction lengths for a number of materials [16] for neutrons in the energy range of 80 GeV to 200 GeV.

Tab. 2.1 with the nuclear interaction lengths of the considered materials, it is observed that for elements with a atomic number $Z > 6$ the nuclear interaction lengths exceed the radiation lengths. In order to build calorimeters, solids with high densities are needed because the radiation and nuclear interaction lengths have to be kept small in order to keep the calorimeter small. This is described in more detail in Chap. 3. Solid materials with high densities are only found among those with high Z values. Since the nuclear collision length exceed the radiation length for high- Z materials, e.g. for iron they differ by a factor 10, the dimensions of hadronic calorimeters always exceed the dimensions of electromagnetic calorimeters.

2.5 Transition radiation

When a charged particle crosses the boundary of two materials with different dielectric constants, the polarisation cloud around the particle changes. As the field is continuous at the transition, as given in Maxwell's equations, a field change and emission of radiation are the consequences. This radiation is called *transition radiation*. Compared with the energy loss due to ionization or Bremsstrahlung, this kind of energy loss is negligible. However, it plays a key role in particle identification. A schematic sketch of this process is shown in Fig. 2.13. When considering a particle crossing such a boundary, the intensity I per frequency interval $d\nu$ and polar angle interval $d\Theta$ is given by [23, 24]

$$\frac{d^2 I}{d\Theta d\nu} = \frac{2\alpha\hbar\Theta^3}{\pi} \cdot \left(\frac{1}{1/\gamma^2 + \Theta^2 + \omega_1^2/\nu^2} - \frac{1}{1/\gamma^2 + \Theta^2 + \omega_2^2/\nu^2} \right)^2 \quad (2.23)$$

with ν denoting the photon frequency, $\omega_i = \sqrt{(1 - \epsilon_i)\nu^2}$ the plasma frequency, ϵ_i the dielectric constant and γ the Lorentz-factor.

Hence, the emission is isotropic in the azimuthal angle Φ around the flight direction of

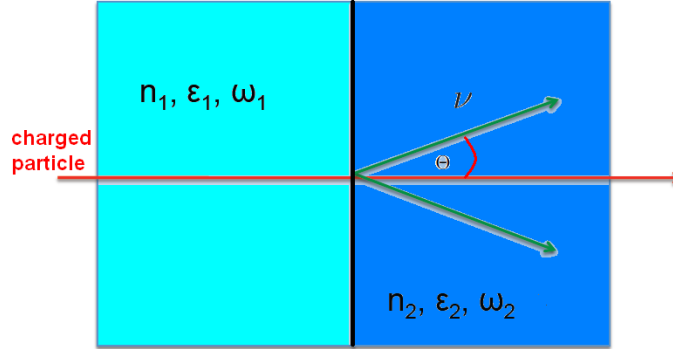


Figure 2.13: Emission of Transition Radiation due to two different dielectric constants. The meaning of the constants is as follows. ϵ_i is the dielectric constant, $n_i = \sqrt{\epsilon_i}$ is the refractive index, ν denotes the photon frequency and $\omega_i = \sqrt{(1 - \epsilon_i)}\nu^2$ the plasma frequency. This figure has been taken from [19].

the particle and the mean emission polar angle Θ is about $1/\gamma$. Integrating over full polar angle Θ and frequencies gives

$$I = \int \int \left(\frac{d^2 I}{d\Theta d\nu} \right) d\Theta d\nu = \frac{\alpha \hbar (\omega_1 - \omega_2)^2}{\omega_1 + \omega_2} \cdot \gamma. \quad (2.24)$$

Thus the intensity of transition radiation is proportional to the Lorentz-factor γ . Therefore, transition radiation is useful in order to separate light charged particles, e.g. electrons, from other charged particles such as charged pions, protons or charged kaons. In the energy range of some GeV of the incident electron transition radiation photons have a typical energy in the X-ray range, namely between 100 eV and 250 keV. However, the intensity in this energy region is in the order of $I \approx 10^{-2} \cdot \gamma$ eV for one transition. In order to get a sufficient yield of photons, some hundred transitions are essential. This is achieved by a radiator with a stack of several hundred layers of the proper materials as it is done in the case of the Transition Radiation Detector in the ALICE-experiment. With this setup, in the energy range of some GeV, an electron produces on average one transition radiation photon, whereas in case of all other particles with a Lorentz-factor γ at least a factor 200 lower the probability for emitting a transition radiation photon is practically zero.

2.6 Cherenkov radiation

When a charged particle propagates in a medium with a refractive index n at a velocity $v > \frac{c}{n}$, *Cherenkov radiation* is emitted. In case of $v > \frac{c}{n}$ the atoms around the particle track are polarized that way, that a resulting dipole moment emerges. Therefore electromagnetic radiation is emitted. In case of $v < \frac{c}{n}$ the electromagnetic waves emitted by the individual atoms interfere destructively and no radiation is emitted. As in case of transition radiation, this kind of energy loss is negligible compared to the total energy loss. However, Cherenkov radiation is used for particle identification, calorimetry and even particle tracking.

The Cherenkov photons are emitted isotropically in the azimuthal angle Φ around the flight direction of the charged particle with an polar angle Θ_c , which is given by

$$\cos \Theta_c = \frac{1}{n\beta} \quad \left(\begin{matrix} \leq \\ \leq 1 \end{matrix} \right). \quad (2.25)$$

This equation implies an energy threshold for Cherenkov photon emission because the relativistic velocity β depends only on the energy of a particle with a fixed rest mass. The amount of emitted Cherenkov photons per wavelength interval $d\lambda$ is given by [15]

$$\frac{dN}{d\lambda} = \frac{2\pi\alpha}{\lambda^2} L \left(1 - \frac{1}{\beta^2 n(\lambda)^2} \right) \quad (2.26)$$

with L denoting the path length of the charged particle in the considered medium with the refraction index $n(\lambda)$ depending on the wavelength λ .

If the dependency of the refractive index on the wavelength is neglected and a mean value n_0 with $n(\lambda) \approx n_0$ for the refractive index is taken, an integral over the optical wavelength spectrum from 400 nm to 700 nm is given by

$$N = 2\pi\alpha L \cdot \left(1 - \frac{1}{\beta^2 n_0^2} \right) \cdot \int_{400\text{nm}}^{700\text{nm}} \frac{d\lambda}{\lambda^2} = 490 \cdot L \cdot \left(1 - \frac{1}{\beta^2 n_0^2} \right). \quad (2.27)$$

In Fig. 2.14 the number of emitted Cherenkov photons per unit length as a function of energy for electrons traversing lead glass with $n_0 = 1.7$ is shown. The amount of emitted

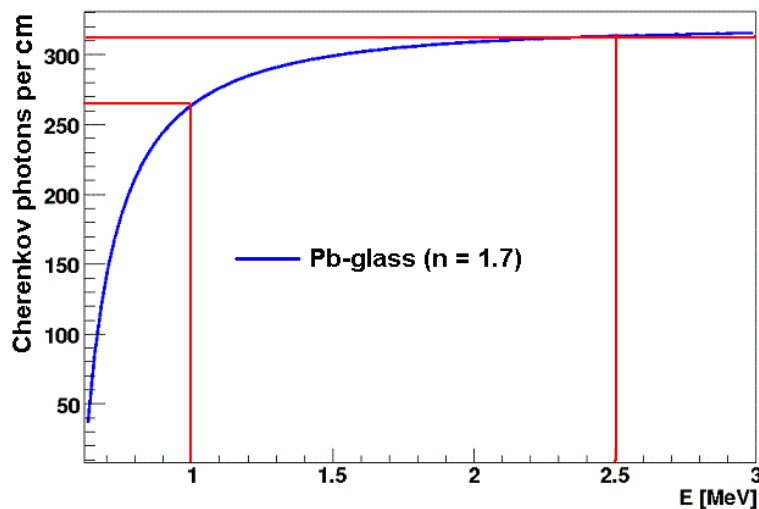


Figure 2.14: The number of emitted Cherenkov photons per unit length as a function of the electron energy in lead glass. Above 2.5 MeV the amount of emitted Cherenkov photons saturates around a constant value of 310.

Cherenkov photons rises from 0 at $E = 620$ keV, which is the threshold for Cherenkov radiation emission, up to 265 at $E = 1$ MeV. Above 1 MeV the rise is rather moderate and not more than 20%. Finally, the curve saturates at a constant value around 310 above an energy of 2.5 MeV.

3 Particle detectors

In this chapter some basic facts about Cherenkov detectors and electromagnetic calorimeters are given since they played an important role during the TRD Testbeam 2007 at CERN.

3.1 Calorimeters

In order to measure the total energy of a highly energetic particle, it has to be completely stopped and the deposited energy within the detector volume has to be measured. This kind of energy measurement is called *calorimetry* and detectors which perform this kind of measurement are therefore called *calorimeters*. The basic property of a feasible calorimeter is

$$\text{Signal} \propto \text{deposited energy } E_{\text{dep}} \propto \text{particle energy } E_{\text{particle}}. \quad (3.1)$$

In general, there are two types of calorimeters

- hadronic calorimeters
- electromagnetic calorimeters.

The basic principle of these two types of calorimeters is similar. In both cases the highly energetic particles hit the detector volume and showers are generated by cascades of interactions. After that, the secondary charged particle tracks create a signal. Either the created charge of the charged shower tracks is measured or the radiation of the secondary tracks, e.g. scintillation light or Cherenkov radiation, is registered.

Hadronic calorimeters measure the energy of highly energetic hadrons such as protons, pions or kaons. The main process that creates the particle shower is the strong interaction. Electromagnetic calorimeters measure the energy of highly energetic photons, electrons and positrons. Here, the main processes involved in shower creation are Bremsstrahlung and pair creation.

Moreover, calorimeters are classified in two more basic types

- homogeneous calorimeters
- sampling calorimeters.

Homogeneous calorimeters are built up of one single block of the same detector material and the whole shower occurs inside this block. Some devices, e.g. photo cathodes, mirrors, readout electronics etc., are located at the boundaries of this block in order to detect e.g. the secondary charge or the secondary soft radiation. Thus the whole detector material is used for signal creation and energy absorption.

Sampling calorimeters are built up like a sandwich. Dead absorbing detector material with

high density, e.g. lead or tungsten, and active detector material, mostly gas, alternate. In the active detector material the signal is created. In Fig. 3.1 and Fig. 3.2 sketches of both detector types are shown.

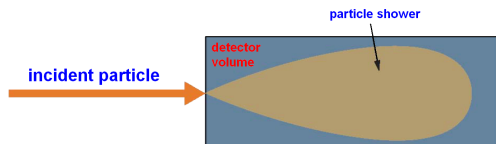


Figure 3.1: Working principle of a homogeneous calorimeter. The detector volume serves as an absorber and for active signal creation. This figure has been taken from [40].

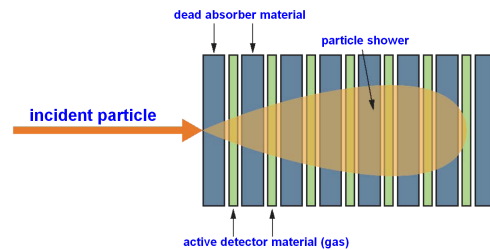


Figure 3.2: Working principle of a sampling calorimeter. Only the active detector volumes serve as sources for the signal. The dead detector material is needed for absorption of energy. This figure has been taken from [40].

Electromagnetic calorimeters

Electrons and positrons above some tens of MeV mainly lose energy by emitting Bremsstrahlung photons. These photons create electron-positron pairs which emit Bremsstrahlung again, i.e. a cascade is created. A sketch of such a cascade is shown in Fig. 3.3. If a

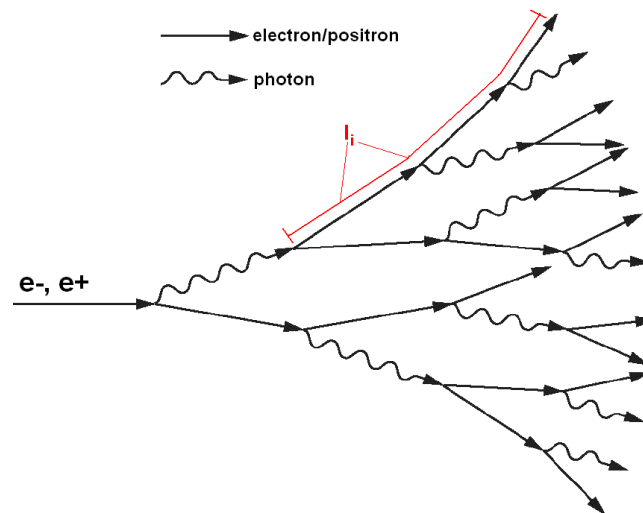


Figure 3.3: Schematic representation of an electron/positron initiated electromagnetic cascade.

highly energetic photon hits the detector volume, the same happens. The only difference is that the first created secondaries are leptons and not photons. The longitudinal dimension D_L of an electromagnetic shower within a calorimeter is calculable by using a simple model of Heitler and Rossi [29] or more precisely by Monte-Carlo simulations [31, 32, 16].

The simple model predicts

$$D_L = \frac{1}{\ln 2} \cdot \ln \frac{E_0}{E_c} \cdot X_0 \approx 1.45 \cdot \ln \frac{E_0}{E_c} \cdot X_0. \quad (3.2)$$

Detailed Monte Carlo simulations give the following result

$$D_L = 2.5 \cdot \underbrace{\left(\ln \frac{E_0}{E_c} + C_i \right)}_{\text{shower maximum}} \cdot X_0 ; \text{ with } C_\gamma = +0.5, C_e = -0.5 (\gamma, e^\pm : \text{incident particles}) \quad (3.3)$$

with E_0 denoting the energy of the incident particle and E_c the critical energy.

The broadening of the shower is mainly driven by Molière scattering since the emission angle of Bremsstrahlung and the opening angle of pair conversion are much smaller than the mean Molière scattering angle. The transversal dimension D_{TR} of the shower is characterized by the *Molière radius* R_m . 95% of the shower energy are inside a tube with twice the *Molière radius*

$$D_{TR} = 2R_m = \frac{42MeV}{E_c} \cdot X_0. \quad (3.4)$$

D_L and D_{TR} are only correct for homogeneous electromagnetic calorimeters. For sampling calorimeters these values are higher since the energy absorption in the active gaseous detector parts is very small. The knowledge of D_L and D_{TR} is essential when designing a calorimeter, especially its dimensions.

Another important issue in calorimetry is the finite energy resolution of the considered calorimeter. Here, a different approach is followed when considering homogeneous and heterogeneous calorimeters. Since during the Testbeam 2007 a homogeneous electromagnetic calorimeter was used, the resolution contributions only of this kind of calorimeters are discussed here. The sources for a finite resolution in that case are

1. statistical fluctuations in the total track length of charged particles $L = \sum l_i$ with l_i denoting the track length of one created charged particle inside the detector volume, see Fig. 3.3;
2. fluctuations in the number of directly detectable "soft" particles, e.g. Cherenkov photons, secondary electrons and ions, scintillation photons;
3. noise of the electronics;
4. dead detector regions, calibration uncertainties;
5. leakage, in case the shower does not fully remain inside the detector volume.

The most important condition for feasible calorimetry is that the signal of a calorimeter is proportional to the energy of the incident particle. In order to achieve this goal, some

requirements have to be fulfilled, so that the following proportionality chain can be built up

$$S \propto \lambda \cdot P_s \propto L \propto E_0 \quad (3.5)$$

with S denoting the signal, $\lambda \cdot P_s$ the measured yield of "soft" directly detectable particles, L the total track length of charged particles and E_0 the energy of incident particle. The first step $L \propto E_0$ is valid because L is given by [29]

$$L \approx \frac{E_0}{E_c} \cdot X_0. \quad (3.6)$$

Therefore, since the path length L fluctuates like $\frac{\sigma(L)}{L} \approx \frac{\sqrt{L}}{L}$, the contribution to the energy resolution is

$$\frac{\sigma(E)}{E} \propto \frac{\sigma(L)}{L} = \frac{1}{\sqrt{L}} \propto \frac{1}{\sqrt{E}}. \quad (3.7)$$

The second step $P_s \propto L$ is also valid and a justification will only be given here for calorimeters, which detect Cherenkov photons as "soft" directly detectable particles, e.g. with a photo cathode. All charged shower tracks produce Cherenkov photons until their kinetic energy falls below the Cherenkov emission energy threshold. The amount of emitted Cherenkov photons is almost independent of the energy over a large energy range for materials with a high refractive index, which are used for Cherenkov electromagnetic calorimeter as shown in Fig. 2.14. Only at the end of a particle track when the particle energy reaches about 1 MeV the production of Cherenkov photons decreases significantly. However, in that energy range the energy loss of electrons and positrons rises very fast because they are not minimum ionizing particles anymore and they are immediately stopped. Hence, the track length contribution below 1 MeV can be completely neglected; above all because the mean energy of a produced shower particle is in the order of the critical energy E_c , e.g. $E_c = 10$ MeV for lead glass.

The amount of "soft" detectable particles N fluctuates like $\frac{\sigma(N)}{N} \approx \frac{\sqrt{N}}{N}$. Therefore the contribution to the total energy resolution is proportional to $\frac{1}{\sqrt{E}}$ as in case of L (see Eq. (3.7)). The last proportionality step $\lambda \cdot P_s \propto S$ requiring the proportionality between the signal S and the yield of the directly detectable "soft particles" $\lambda \cdot P_s$ such as Cherenkov photons is trivial.

Moreover, the contribution of electronic noise is $\propto \frac{1}{E}$. Other influences such as calibration uncertainties or dead detector regions are energy independent and are assumed to contribute with a constant factor c_3 . Therefore, if the homogeneous electromagnetic has the proper dimensions and lateral as well as longitudinal leakage are negligible, the resolution is parameterized by

$$\frac{\sigma(E)}{E} = \sqrt{\frac{c_1^2}{E} + \frac{c_2^2}{E^2} + c_3^2}. \quad (3.8)$$

Hence, the resolution improves with rising energy and is dominated by the constant factor c_3 in the high energy range. However, if leakage is not negligible, it contributes to the total resolution, too. In case of longitudinal leakage the contribution is given by [29]

$$\frac{\sigma(E)}{E} \propto \ln E. \quad (3.9)$$

The contribution of lateral leakage is much smaller. In Fig. 3.4 the effect of leakage on the resolution is shown.

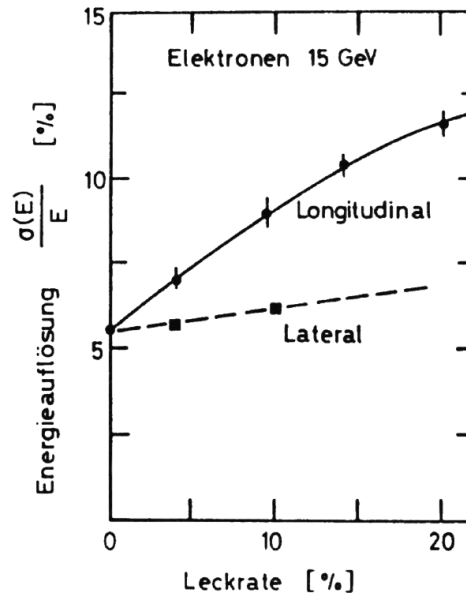


Figure 3.4: Measured relative energy resolution of a calorimeter (CHARM Collaboration) as a function of lateral and longitudinal leakage in units of per cent. The incident particles were electrons with an energy of 15 GeV. This figure has been taken from [29].

3.2 Cherenkov detectors

Detectors, which detect Cherenkov photons, are used to measure the speed of a charged particle because the Cherenkov emission angle depends on the relativistic velocity β , as given in Eq. (2.25). Also tracking by detecting Cherenkov radiation is possible. The most important application however, is particle identification. In Fig. 3.5 the energy range is

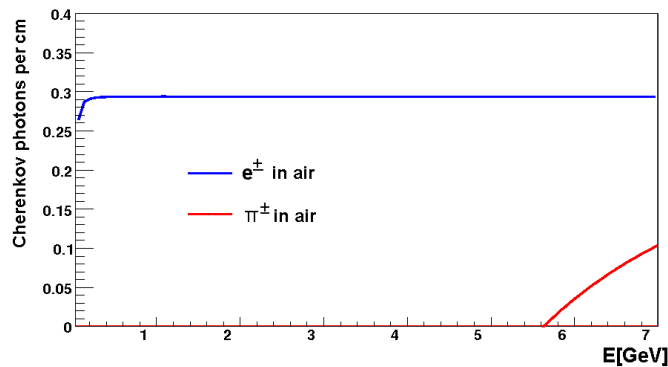


Figure 3.5: Emitted Cherenkov photons per unit length as a function of energy for electrons and charged pions in air.

shown, at which pions are efficiently suppressed when using air with a refraction index

$n = 1.0003$ as a radiator.

A big challenge for particle identification with usage of Cherenkov radiation is the separation of the photons from the background. This background mainly consists of photons, which are emitted by atoms along the particle track due to de-excitation and secondary electron recapture. Energy loss due to ionization is two to three orders of magnitude higher than due to Cherenkov light emission. However, Cherenkov photons are emitted well focused isotropically in azimuth Φ and with a fixed polar angle Θ_c (see Eq. (2.25)), whereas de-excitation photons are emitted isotropically in all directions. One possibility to measure Cherenkov light is schematically drawn in Fig. 3.6. This figure displays a simple

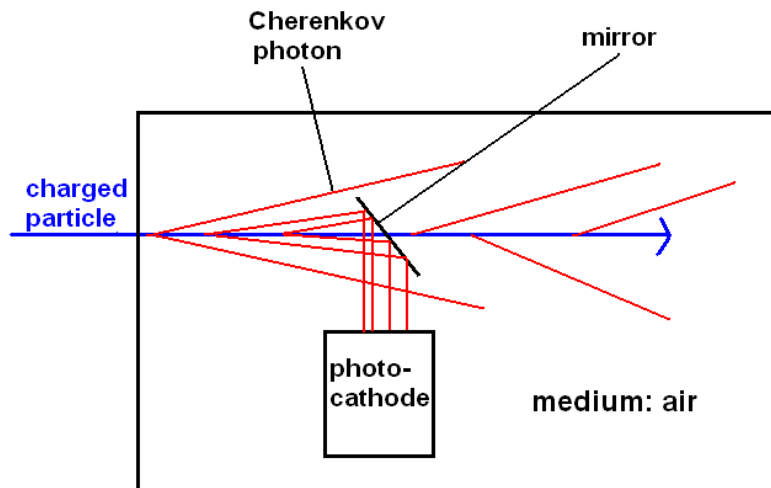


Figure 3.6: Sketch of a primitive Cherenkov detector. The Cherenkov light is deflected with a mirror and detected with a photo cathode.

Cherenkov detector. The charged particle enters the active volume of the detector filled with air. The emitted Cherenkov photons are collected with a mirror and focused onto a photo cathode, where they release electrons inducing an electrical signal.

4 The Large Hadron Collider

The **L**arge **H**adron **C**ollider (LHC) at the European organization for nuclear research (CERN) near Geneva has officially gone online on September 10th, 2008. However, the LHC is currently off-state and under repair due to an incident occurred on September 19th, 2008 resulting in a large helium leak into its circular tunnel. After the repair, the LHC will collide two counter rotating beams of protons or heavy ions at unprecedented high energy and luminosity in the circular tunnel of 27 km circumference. The LHC will provide proton-proton collisions at a design luminosity of $10^{34} \text{ cm}^2 \text{ s}^{-1}$ and a center-of-mass energy of $\sqrt{s} = 14 \text{ TeV}$. For lead-lead collisions the maximum energy is $\sqrt{s_{NN}} = 5.5 \text{ TeV}$ per nucleon pair at a design luminosity of $10^{27} \text{ cm}^2 \text{ s}^{-1}$. There are three main detectors which mainly profit from proton-proton collisions (ATLAS, CMS, LHCb) and one detector mainly profiting from lead-lead collisions (ALICE). All four experiments are located at so called interaction points where the two LHC particle tubes intersect and collisions take

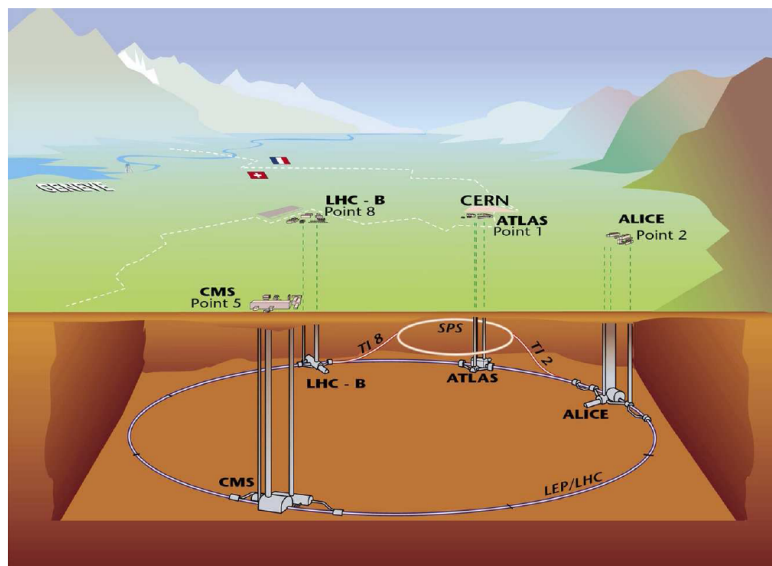


Figure 4.1: Schematic sketch of the LHC with its four main experiments ATLAS, CMS, LHCb, ALICE. This figure has been taken from [48].

place as shown in Fig. 4.1. In the following basic facts about the four experiments are given:

1. **ATLAS:**

The main goal of **A** **T**oroidal **L**HC **A**pparatus (ATLAS) experiment is the detection of the Higgs-Boson and the search for physics beyond the standard model, e.g. supersymmetric particles and extra dimensions.

2. CMS:

The **Compact Muon Solenoid (CMS)** is designed to analyze the nature of matter. In principle the CMS and the ATLAS detectors are built for the same purpose applying different detector technologies.

3. LHCb:

The **LHC beauty (LHCb)** experiment is built to observe CP violation in B-meson systems. LHCb will help to understand why the universe appears to be composed almost entirely of matter but no antimatter.

4. ALICE:

A **Large Ion Collider Experiment (ALICE)** is the dedicated heavy ion detector at

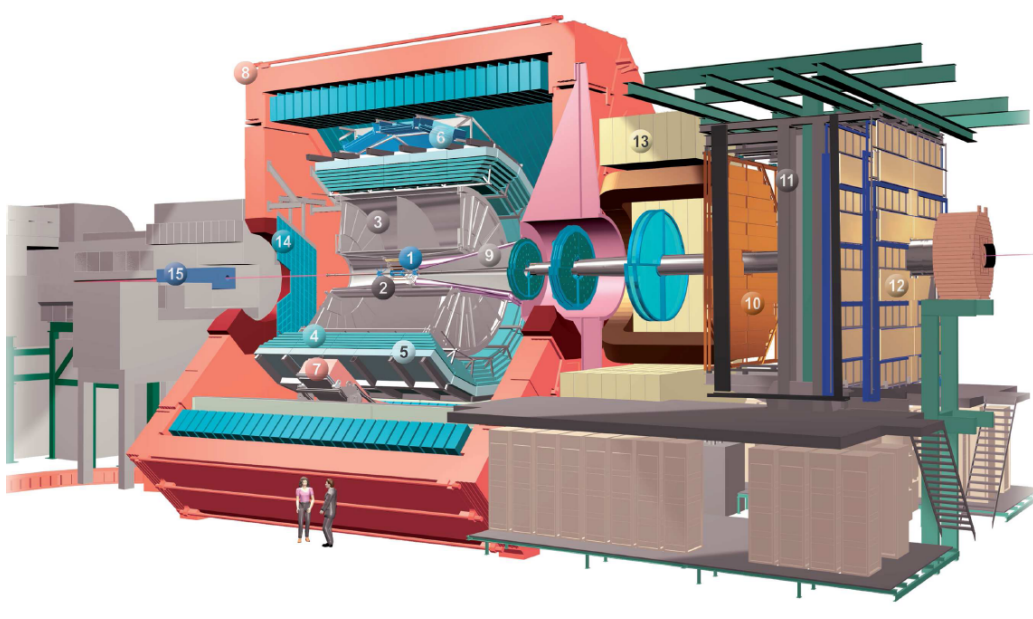


Figure 4.2: Schematic overview of the ALICE experiment. The main subdetectors are: ITS(1), TPC(3), TRD(4), TOF(5), HMPID(6) and PHOS(7). They are surrounded by the L3 magnet(8). Details about the muon arm (numbers 9 to 13) as well as about the FMD(2), PMD(14) and the Compensator Magnet(15) can be found in [51, 50]. This figure has been taken from [49].

the LHC. The ALICE detector is designed to identify and characterize the quark gluon plasma. It consists of several subdetectors, which are shown in Fig. 4.2. The most important ones are:

- **Inner Tracking System:**

The **Inner Tracking System (ITS)** is located at radii between 4 cm and 44 cm around the interaction point and consists of silicon strip, silicon pixel and silicon drift detectors. It provides highest spatial resolution and secondary vertexing capabilities.

- **Time Projection Chamber:**

The **Time Projection Chamber (TPC)** is located at radii between 85 cm and 250 cm around the interaction point and is the main tracking device of the ALICE

detector. The particle tracks are reconstructed by detecting the created charge in the gas (Ne/CO₂), which is extracted by applying a high voltage.

- **Transition Radiation Detector:**

The **T**ransition **R**adiation **D**etector (TRD) is described in detail in Chap. 5.

- **Time Of Flight:**

The **T**ime **O**f **F**light detector is placed at a radial distance of approximately 4 m and measures the time of flight of particles from the interaction point. The time information is used for particle identification.

- **High Momentum Particle Identification Detector:**

The **H**igh **M**omentum **P**article **I**dentification **D**etector (HMPID) is placed at larger radii than the TOF detector and measures the Cherenkov radiation emission angle described in Chap. 2 of charged hadrons at $p_T > 1$ GeV/ c . The measurement of this angle is used for particle identification.

- **Photon Spectrometer:**

The **P**hoton **S**pectrometer (PHOS) is an electromagnetic spectrometer and measures the energy as well as the impact parameter of photons.

5 The Transition Radiation Detector

The Transition Radiation Detector (TRD) consists of 540 drift chambers, arranged in 18 supermodules containing 5 longitudinal stacks arranged radially in 6 layers. The support structure for every supermodule is called the TRD *Babyframe*, which is shown in Fig. 5.1. The 18 Babyframes are arranged in the so-called ALICE *Spaceframe* depicted in Fig. 5.2, a superordinate support structure carrying also the ALICE TPC (see Chap. 4), covering full azimuth Φ , the pseudorapidity range $-0.9 \leq \eta \leq 0.9$ and a radial range from 2.9 m to 3.7 m. More details can be found in [36]. The TRD identifies electrons with momenta above

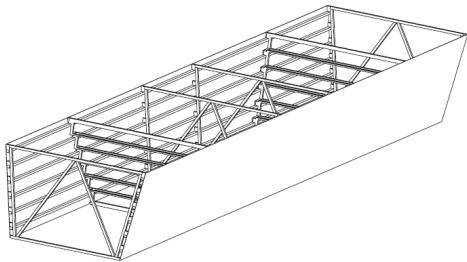


Figure 5.1: The TRD Babyframe. This figure has been taken from [36].

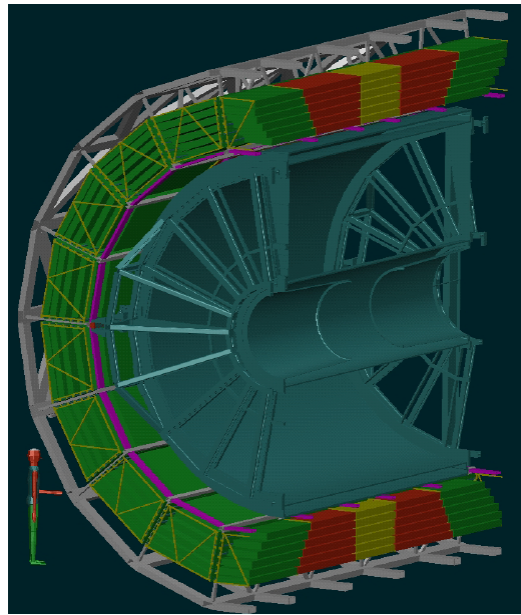


Figure 5.2: The TRD (green, red and yellow) and the TPC (blue) in the ALICE Spaceframe. This figure has been taken from [37].

1 GeV/ c by detecting their transition radiation photons, which are emitted as described in Chap. 2. While reaching an electron efficiency of 90%, the TRD achieves a pion rejection of 100:1, i.e. 90% of the detected electrons are identified properly as electrons and at the same time less than 1% of the pions are mis-identified as electrons. Moreover, the TRD provides fast ($6\mu s$) triggering capability for high transverse momentum charged particles at $p_T > 3$ GeV/ c .

5.1 The TRD working principle

The TRD chambers can be subdivided into a multiwire proportional chamber including the drift (3 cm) as well as the amplification region (0.7 cm) and in the radiator (4.8 cm). Figure 5.3 shows a schematic projection of the TRD chamber in the plane perpendicular to the wires. If a highly energetic electron with a Lorentz-factor $\gamma > 1000$ crosses the radiator,

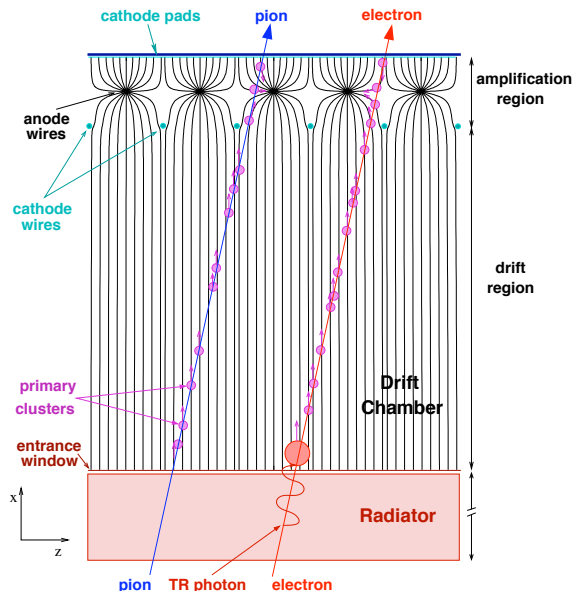


Figure 5.3: A schematic sketch of the TRD chamber as seen from the top perpendicular to the wires. The difference between pions with a low Lorentz-factor γ and electrons with a high Lorentz-factor γ thus emitting transition radiation is indicated. This figure has been taken from [36].

it produces on average one transition radiation photon, which enters simultaneously with the primary electron the drift region having a very small emission angle with respect to the electron momentum (see Chap. 2). In order to provide an efficient transition radiation photon absorption, a gas mixture based on Xenon and 15% CO_2 , needed as a quencher, is used. The transition radiation photons are absorbed within the drift region producing an electron cluster. The highly energetic electron traverses the gas producing a track of electron clusters. The produced secondary electrons drift with a constant drift velocity towards the amplification region where they are accelerated in the strong field near the anode wires. There their energies increase sufficiently that they are able to ionize gas atoms further and an avalanche process occurs. This process is called *gas gain*. The signal on the cathode pads which make up the *pad plane* of the chamber is induced by the positive ions created in the avalanche process. This signal is read out by the front-end electronics. The pads on the *pad plane* have a typical area of 6 - 7 cm^2 and cover the total active area of the TRD with approximately 1.2 millions readout channels. For the track reconstruction of electrons and other charged particles the signal on the pad plane array, which provides two coordinates in space, and the time information assuming a constant drift velocity is used. For the particle identification the large electron cluster at the beginning of the drift chamber due to the absorption of transition radiation photons is used. In Fig. 5.4 the signal as a function of time is plotted for electrons and pions. More details about signal

processing, particle identification and tracking can be found in [36].

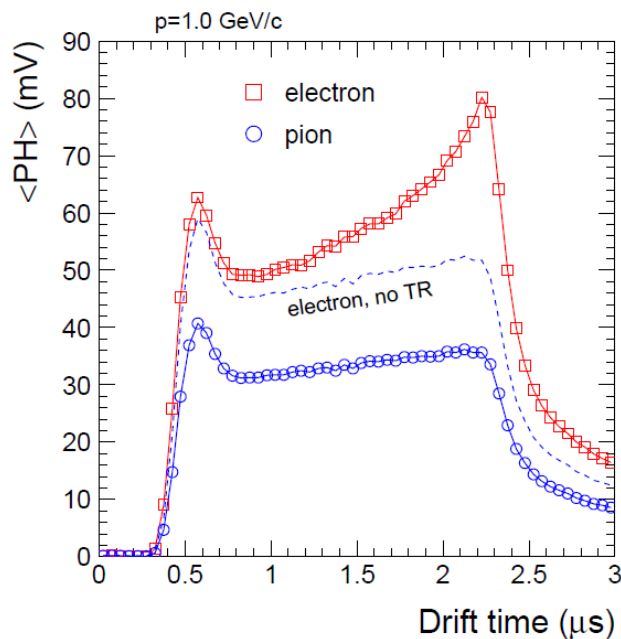


Figure 5.4: Average pulse height as a function of drift time for electrons (red, rectangles), pions (blue, circles) and electrons without TR photon absorption (blue, dashed line). The global higher signal of electrons is due to higher deposited energy of electrons in comparison to pions and the characteristic peak at a Drift Time = $2.3 \mu\text{s}$ due to transition radiation photon absorption. This figure has been taken from [36].

5.2 Estimated radiation length

The TRD supermodule consists of various materials which all contribute to the average radiation length X_0 and thus to the average radiation thickness X/X_0 of the full TRD supermodule. The formula for calculating the radiation length X_0 is the formula of Tsai described in detail in Sect. 2.2.2. When considering a mixture of different elements, e.g. water (H_2O), the following approximation is valid

$$1/X_0 = \sum w_i/X_i, \quad (5.1)$$

where w_i is the fraction of weight of the i -th element and X_i the radiation length of this element.

A detailed investigation of the radiation thickness X/X_0 of the active area of the TRD can be found in [33]. Here, a short summary of this note is presented.

The active area of the TRD can be subdivided into 3 parts.

- The top and bottom plates of the babyframe.
- The read out chambers (ROC)
 - radiator

- gas
- amplification region (wires, gas)
- pad plane.
- The electronics
 - readout board
 - multi chip module (MCM)
 - active and passive components and connectors
 - DCS board, for details see [36]
 - OASE board, for details see [36]
 - Cooling, for details see [36].

A cross section of the TRD chamber including the used materials is shown in Fig. 5.5.

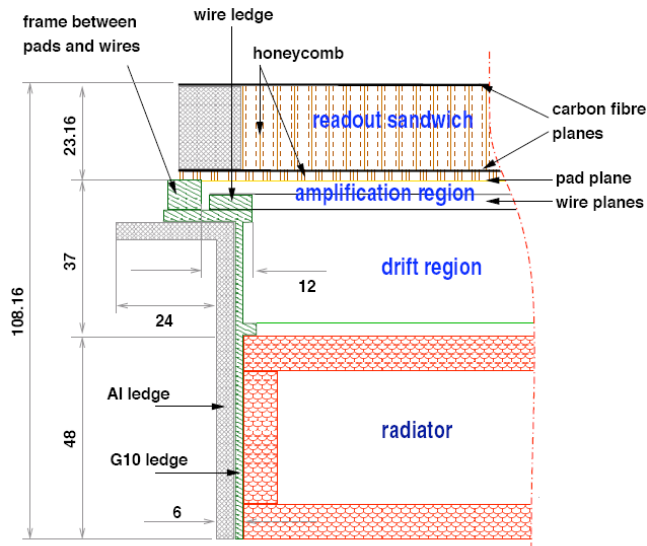


Figure 5.5: Cross Section of a TRD readout chamber. The numbers depicted in the figure are lengths in units of mm. This figure has been taken from [37].

When analyzing the composition of the single parts of the TRD one has to consider two cases.

1. The investigated material has a defined thickness, as e.g. the top and bottom plates of the supermodules, and covers the full or a defined fraction of the active area. In this case the contribution to the total radiation thickness X/X_0 of the TRD scales linearly with the thickness d and the fraction covered.
2. The investigated material does not have a defined thickness, rather the mass per unit area is known. Then the contribution scales linearly with the total mass per unit area. Such an approximation is applied e.g. in case of any kind of glue.

In Tab. 5.1 the result of the analysis for one radiator, whereas in one stack of a supermodule there are six of them, of the TRD is shown. In Tab. 5.2 the contributions of all parts for one whole supermodule are shown. The most important value in these tables is the radiation thickness $X/X_0[\%]$ of the single parts, which contribute to the total radiation thickness of one supermodule. A radiation thickness X/X_0 of 100% means that an electron with an energy E_0 crossing this amount of material loses on average $\Delta E = E_0 \cdot (1 - e^{-1})$ of its energy and a highly energetic photon with $E_{\text{phot}} > 10$ MeV traverses 7/9 of its mean-free path as described in Chap. 2. According to this analysis, the averaged ra-

part	$X_0[g/cm^2]$	$\rho_0[g/cm^3]$	$X_0[mm]$	$M[g/m^2]$	$d[mm]$	$X/X_0[\%]$
Rohacell	40.8	0.075	5440		16	0.294
fibers	45.2	0.068	6647		32	0.481
carbon fiber	42.7	1.8	237	190		0.045
mylar	45.2	0.9	503		0.024	0.005
Aluminium	24.01	2.7	88.9		0.006	0.007
Glue	42.6	1.2	354.9	150		0.035
Air	37.1	0.0012	318425.2		31.4	0.01
Sum						0.877

Table 5.1: Different parts of the radiator and their contribution to the radiation thickness of the TRD. The meaning of the variables is as follows. $X_0[g/cm^2]$ is the radiation length, calculated by using the formula of Tsai [34] and Eq. (5.1). $\rho_0[g/cm^3]$ is the density of the considered material, $X_0[mm]$ is the radiation length in millimeters, obtained by dividing the radiation thickness $X_0[g/cm^2]$ by the density. $M[g/m^2]$ denotes the mass per unit area of the considered material and $d[mm]$ is the thickness of the layer of the considered material. Finally, $X/X_0[\%]$ is the radiation thickness of the considered layer of material in per cent and thus the contribution to the total radiation thickness X/X_0^{tot} of one supermodule of the TRD.

Parts	$X/X_0[\%]$
radiators	5.262
pad planes	3.036
back panels	2.940
wires	0.090
chamber gas	1.242
readout boards	4.380
MCMs	1.116
other read out board components	1.182
spacers	0.060
mounting screws	0.372
cooling	0.948
air between chambers	0.3
top and bottom plates	4.5
Sum	25.4

Table 5.2: Parts of one supermodule and their contribution to the radiation thickness of the TRD.

diation thickness for one TRD supermodule is $X/X_0 = 25.4\%$. The radiation length is

calculable if the geometrical thickness X is known. In case of the TRD this is $X \approx 80 \text{ cm}$. Hence, the average radiation length of one TRD supermodule is $\frac{80\text{cm}}{X/X_0} = \frac{80\text{cm}}{25.4\%} = 3.15 \text{ m}$. However, this is only true for particles that cross the supermodule perpendicular to the pad plane, i.e. for $\eta = 0$. Particles traversing the TRD at a certain angle will experience a larger effective radiation thickness. The increase is proportional to the increase of the path length of the particles in the TRD.

The results of this material budget investigation are used within the ALICE Offline Framework AliRoot. Details of AliRoot are described in Chap. 7.

6 Testbeam 2007 at CERN PS

The TRD Testbeam 2007 was carried out at the Proton-Synchrotron (PS) at CERN, beam line T10. Between October and November 2007 the ALICE TRD group has successfully commissioned and operated one of the eighteen TRD supermodules placed in a beam of secondary particles. The aim was to study the performance of the TRD at several beam momenta. After the experiment the idea came up, whether the data is sufficient for determining the average radiation thickness of the TRD.

6.1 Experimental setup

The TRD of the ALICE Experiment has been designed to improve electron identification and tracking. In order to study its performance, a beam with pions and electrons at different momenta was used. For this purpose, protons were accelerated to 24 GeV at the PS at CERN and shot on a fixed target of beryllium. The secondary radiation after the target was collimated. A special dipole magnet for selecting different beam momenta was used. The magnet settings allowed measurements with a fixed secondary beam momentum of 0.3 GeV/c, 0.6 GeV/c, 1.0 GeV/c, 1.5 GeV/c, 2.0 GeV/c, 3.0 GeV/c, 4.0 GeV/c and 6.0 GeV/c. The momentum resolution was $\Delta p/p = 1\%$ for all momenta. In this setup, only negatively charged pions and electrons were selected. A schematic drawing shows the creation of the secondary beam in Fig. 6.1. The beam was directed into an experiment

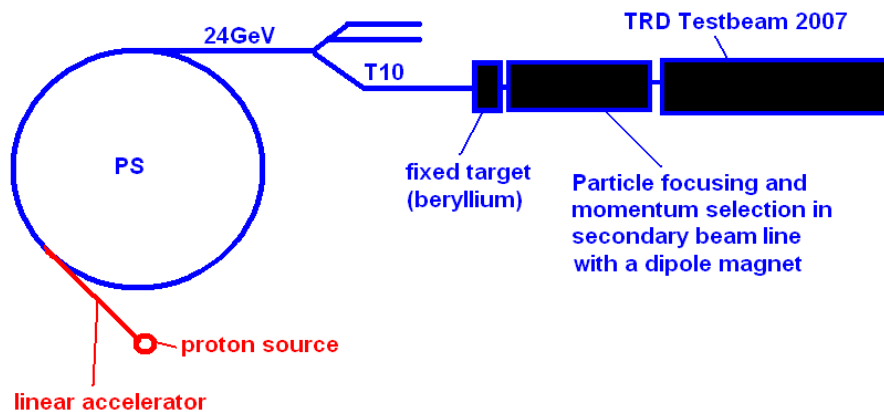


Figure 6.1: Sketch of the creation of the mixed electron/pion beam at the CERN PS during the TRD Testbeam 2007. Details of the experimental setup of the TRD Testbeam 2007 in the experimental hall are given in Fig. 6.2.

hall, where in addition to the TRD some other detectors were arranged along the beam line. A schematic drawing of the experimental setup is shown in Fig. 6.2, which includes

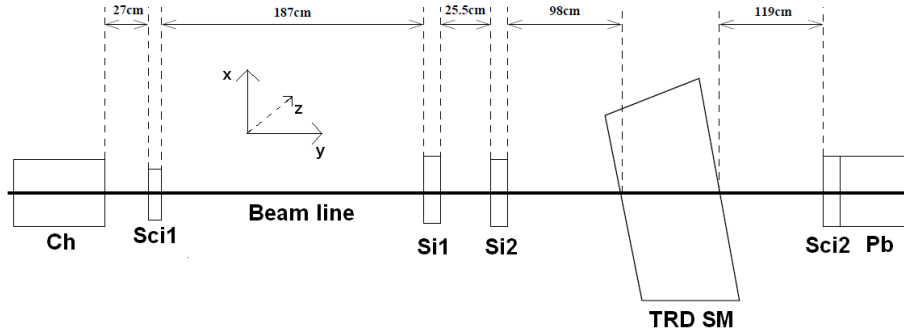


Figure 6.2: Sketch of the installation for the TRD Testbeam at CERN PS, no to scale. Used detectors: Pb: Lead glass calorimeter; Sci1,Sci2: Scintillation trigger detectors; Si1,Si2: Silicon strip detectors; TRD SM: One supermodule of the TRD; Ch: Cherenkov detector. The coordinate system depicted in this figure is defined as follows. The y -axis is parallel to the beam line. The x -axis (vertical direction) and the z -axis (horizontal direction) are perpendicular to the beam line.

the definition of the coordinate system referred to in the following for several times. The y -axis of this coordinate system is parallel to the beam line. The x -axis (vertical direction) and the z -axis (horizontal direction) are perpendicular to the beam line.

The **scintillators** Sci1 and Sci2 indicated in Fig. 6.2 were plastic scintillators, which converted the deposited energy of charged particles into photons in the optical range. Each scintillator was coupled to a photomultiplier tube, in order to convert the photons to an electrical signal. Sci1, which is shown in Fig. 6.3, had an acceptance of $5 \times 7 \text{ cm}^2$

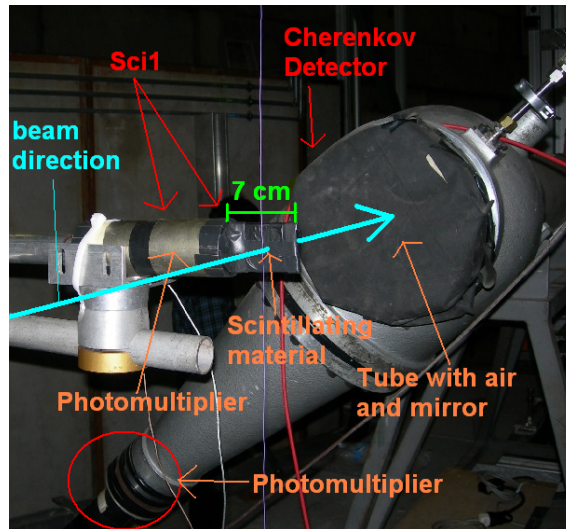


Figure 6.3: Plastic scintillator Sci1 and the Cherenkov detector. The beam direction is indicated with a blue arrow. This photo has been taken from [38].

with 7 cm in the horizontal and the acceptance of Sci2 was $6 \times 6 \text{ cm}^2$.

The **Cherenkov detector** consisted of a tube filled with air at atmospheric pressure, a mirror, which reflected the Cherenkov photons and a photomultiplier tube. A schematic drawing is shown in Fig. 3.6 and a photo of the detector in Fig. 6.3.

The **lead glass calorimeter** consisted of a big block of lead glass ($10 \times 10 \times 35 \text{ cm}^3$) with mirrors on the side surfaces of the block except on the back, in order to collect the produced Cherenkov light within the block. The acceptance in vertical and horizontal direction was each 10 cm. On the back of the block a photomultiplier with a SbKNaCs-photocathode was mounted. The photocathode had a diameter of 15 cm, a sensitivity range from 300 nm to 850 nm and a photon efficiency of about 25%. A sketch of the calorimeter is shown in Fig. 6.4.

Both **silicon strip detectors** Si1 and Si2 had an acceptance of $3.2 \times 3.2 \text{ cm}^2$. The

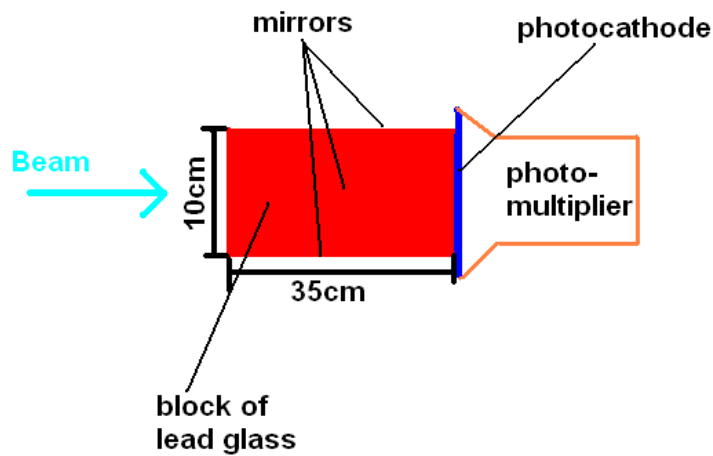


Figure 6.4: Sketch of the lead glass calorimeter.

acceptance of both detectors was filled with 1280 silicon strips, 640 strips in x - and 640 strips in z -direction, each strip with a broadness of $50 \mu\text{m}$ and a thickness of $300 \mu\text{m}$. The strips were mounted in an aluminium frame, where also the readout electronics was placed. A photo of the detector is shown in Fig. 6.5.

The **TRD** detector is described in Chap. 5. The used gas was Xenon and the typical

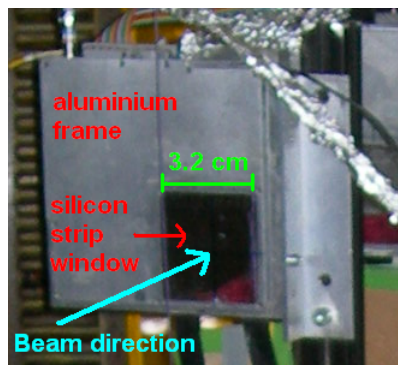


Figure 6.5: One of the two identical silicon strip detectors. This photo of the detector has been taken from [38].

anode voltage was $U_a = 1500$ V. More details can be found in the logbook [38].

Trigger setup

In order to check the performance of the TRD, a clean electron and pion sample was used. During the individual runs of data taking at different momenta triggering on charged particles with Sci1 and Sci2 was performed. A sketch of the setup is shown in Fig. 6.6.

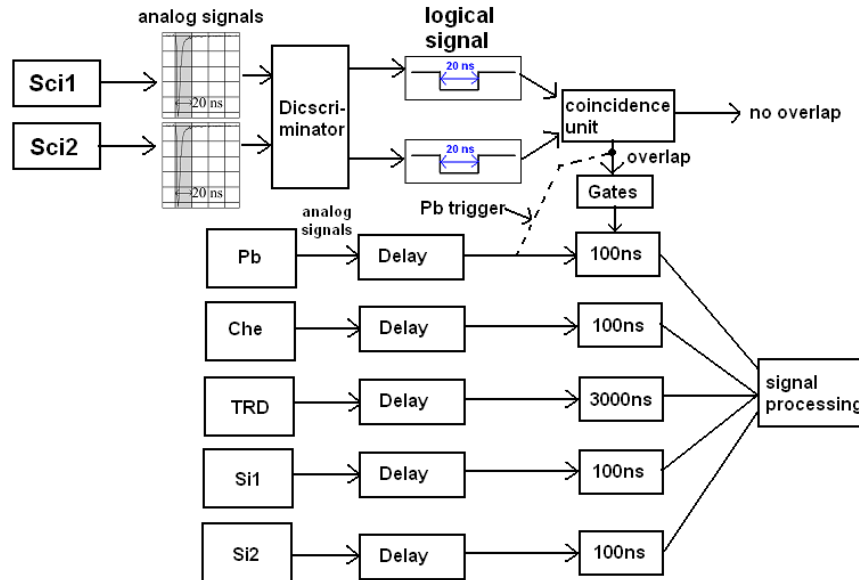


Figure 6.6: Schematic trigger setup of the detectors and electronics used during Testbeam 2007. The dashed line indicated the optional inclusion of the lead glass calorimeter in the trigger decision.

The analog signals of the two scintillation trigger detectors were both converted to a logical signal using a discriminator each signal with a time slot of 20 ns. These logical signals were sent to a coincidence unit. If both time slots overlapped, time gates for the other detectors were opened (see Fig. 6.6). Next, the analog signals of the five indicated detectors were processed, digitized and saved to a file. Since the relative amount of electrons decreased with rising beam momentum, the lead glass calorimeter was involved in the trigger decision for momenta $p > 1$ GeV/ c . In other words, for accepting an event not only an overlap of the logical signal of Sci1 and Sci2 was required, but also the signal of the lead glass calorimeter had to be above a defined threshold, whereas different threshold for different beam momenta were used. This inclusion of the lead glass calorimeter into the trigger decision is indicated in Fig. 6.6. Thus events with higher signal induced in the lead glass calorimeter were favored, i.e. enhancing electrons because they deposited much more energy in the lead glass calorimeter than pions, in the best case all of their energy.

6.2 Data selection and analysis

For reading and analyzing the recorded data the C++ based ALICE Offline Project AliRoot was used which is described in more detail in Chap. 7. A class available in the

AliRoot code was used to process the recorded raw files. `AliTRDtestbeam` was used to convert the raw file, one run, typically some ten thousand events, into a C++ object, which provided with the help of some getters the access to the signals of the different detectors for each event.

In order to get a clean electron sample, whose energy distribution after crossing the TRD is measurable with the lead glass calorimeter, the Cherenkov detector was used to separate the electrons from the pions according to Fig. 3.5.

6.2.1 Cherenkov data

In a first step, the data of the Cherenkov detector was examined. For each momentum and each run the ADC values for some thousand events were filled in one histogram. The term "ADC" is due to a so-called used **A**nalog-to-**D**igital-**C**onverter, which integrated the signal of the Cherenkov detector and converted it to a digital number. The **mean** amount of emitted Cherenkov photons does not depend on the energy in the considered energy range according to Fig. 3.5, where the **mean number** of produced Cherenkov photons per unit length as a function of the particle energy is depicted. Therefore, the detector response is expected to be of Gaussian shape around a mean ADC value. The Gaussian smearing is caused by the fluctuations of the amount of produced Cherenkov photons and the limited resolution of the detector, which is caused by noise of the electronics as well as by fluctuations in the amount of produced photo-electrons in the photocathode. In Fig. 6.7 a typical ADC-distribution for a long run with 182.362 events at a beam momentum $p = 6 \text{ GeV}/c$ is shown. In this distribution two peaks are visible. The narrow peak at

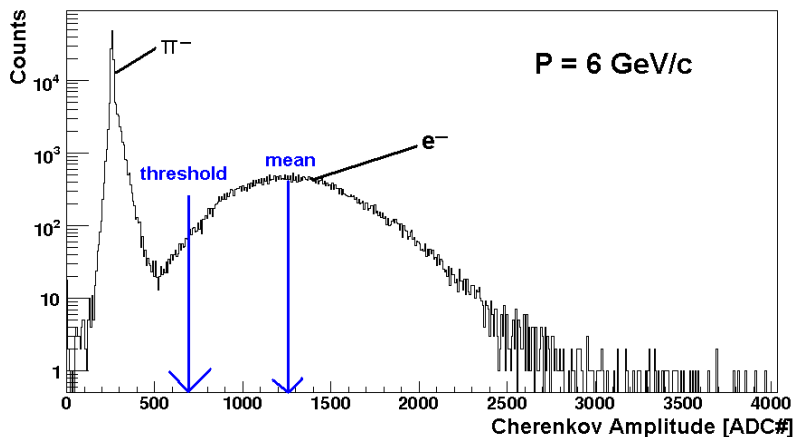


Figure 6.7: Distribution of ADC values of the Cherenkov detector for run 408 at a beam momentum of $p = 6 \text{ GeV}/c$. The arrows indicate the mean of the Gaussian peak caused by the Cherenkov radiation emitted by electrons and the threshold channel for identification as an electron.

lower ADC values is due to detector noise around a pedestal value (≈ 300) because the pions do not produce any Cherenkov light. The right broad peak is due to the Cherenkov light induced by the electrons. For all other runs and energies the plot looks similar except that the mean of the peak of the electrons is moving around by some ten channels due to some instabilities in the detector electronics. The mean of the Gaussian function of the electron signal as a function of run number is displayed in Fig. 6.8 only for runs taken at

a beam momentum of 6 GeV/c. The movement is not significant and thus a successful

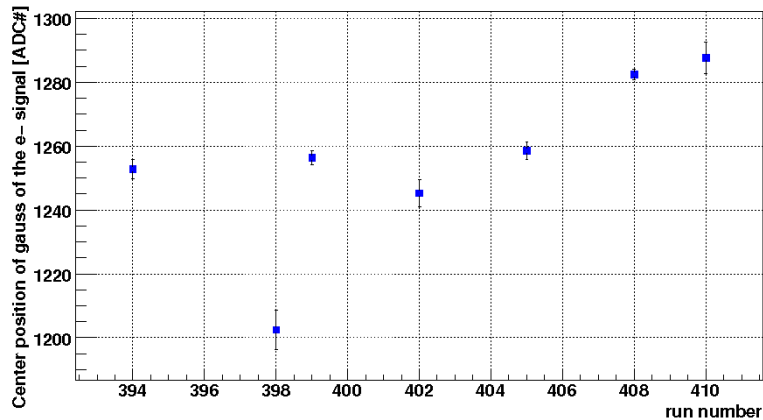


Figure 6.8: Center position of the electron peak for several runs at a beam momentum of $p = 6$ GeV/c.

electron-pion separation is achievable. Thus for every run and beam momentum an ADC threshold for being an electron was determined. As an appropriate value the one, which has a distance of 2σ to the left from the Gaussian mean, was chosen. In the example shown in Fig. 6.7 the corresponding value at channel 664 is visualized by the vertical blue line. Hence all events above this value are identified as electron events. The integrated number of counts above channel 664 is 48.822. Hence for this run 27% ($= 48.822/182.362$) of all events are electron events. However, this does not reflect the real composition of the beam because for a momentum of $p = 6$ GeV/c the lead glass calorimeter was included in the trigger decision, whereas its signal had to be above a defined threshold. This caused a favoring of electron events as described above.

6.2.2 Silicon strip detectors data

The silicon strip detectors located in front of the TRD measured the beam shape. Unfortunately, the acceptance of these two detectors, which was 3.2×3.2 cm², was smaller than the acceptance of the trigger detectors and the lead glass calorimeter. Therefore not all events that were stored had a position information. Moreover, the silicon strip detectors were not perfectly centered in the beam center indicated in Figs. 6.9, 6.11, 6.10 and 6.12. These figures display for both detectors the reconstructed position of the crossing particles for some runs at a beam momentum of $p = 1$ GeV/c in z -direction (horizontal) and x -direction (vertical). The x - z plane is perpendicular to the beam as defined above and visualized in Fig. 6.2. According to these plots, the beam had a FWHM of 5.23 cm in x -direction and a FWHM of 4 cm in z -direction at a beam momentum of $p = 1$ GeV/c. These values were obtained by applying a Gaussian fit to the distributions shown above. The values for the reduced $\chi^2_{red} = \chi^2/NDF$ of all four fits are all in the order of 1 showing good accordance between the used Gaussian fit function and the position distribution in the beam spot at least within the acceptance of the silicon strip detectors. This analysis was also done for beam momenta of 2 GeV/c, 4 GeV/c and 6 GeV/c. For higher momenta the position distributions often and especially in x -direction do not look like a Gaussian function. There, the distributions look more like reversed parabolas. Examples including

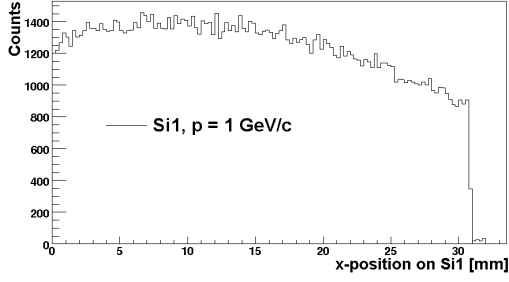


Figure 6.9: Distribution of the x -coordinate on Si1 of crossing charged particles.

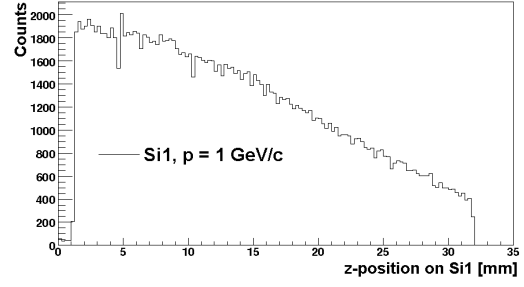


Figure 6.10: Distribution of the z -coordinate on Si1 of crossing charged particles.

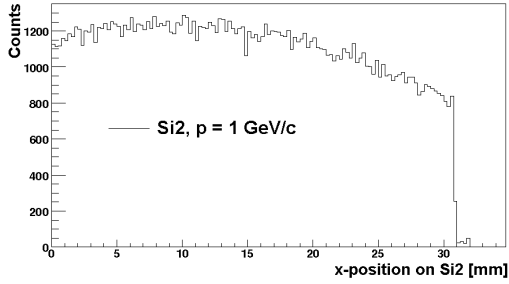


Figure 6.11: Distribution of the x -coordinate on Si2 of crossing charged particles.

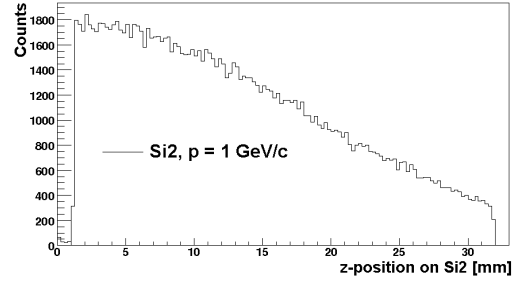


Figure 6.12: Distribution of the z -coordinate on Si2 of crossing charged particles.

the fit parabolas, which are drawn in red, are shown in Fig. 6.13 for a beam momentum of $p = 4$ GeV/ c and in Fig. 6.14 for $p = 6$ GeV/ c . In these cases the beam dimension

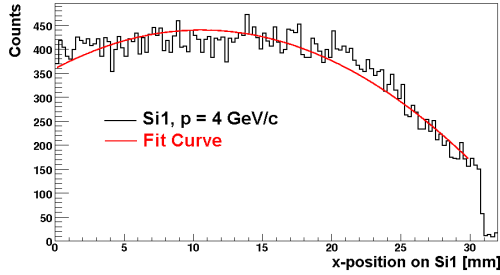


Figure 6.13: Hit distribution of the x -coordinate on Si1 of crossing charged particles at a beam momentum of $p = 4$ GeV/ c . The red curve is the used fit function (reversed parabola).

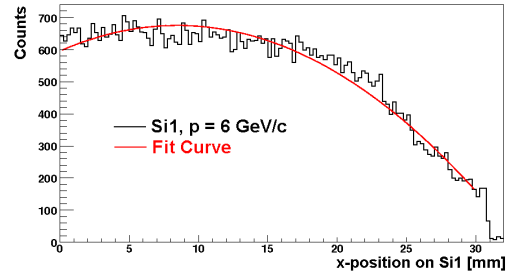


Figure 6.14: Hit Distribution of the x -coordinate on Si1 of crossing charged particles at a beam momentum of $p = 6$ GeV/ c . The red curve is the used fit function (reversed parabola).

parametrized by the FWHM was determined by calculating the distance in from the maximum to half the maximum in signal height.

Moreover, the beam divergence was determined for the four beam momenta. This measurement was possible because there were two silicon strip detectors with a distance of 25.5 cm with respect to each other along the beam line. For a beam momenta of $p = 1$ GeV/ c , $p = 2$ GeV/ c , $p = 4$ GeV/ c and $p = 6$ GeV/ c the residuals in x and z were obtained

and fitted with a Gaussian function. The width σ of this distribution is a measure of the beam divergence which is given by $\sigma_{\phi,\theta} = \arctan \frac{\sigma}{25.5\text{cm}}$ in units of radians. A sketch for illustration is shown in Fig. 6.15 and as an example the residual distribution for a beam momentum of 1 GeV/c in x -direction as well as the corresponding Gaussian fit function are shown in Fig. 6.16. It is not centered at zero because the two silicon strip detectors

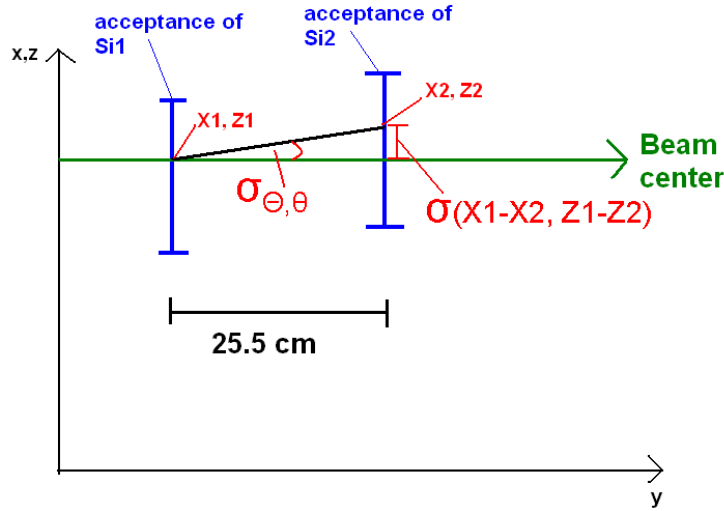


Figure 6.15: Sketch for illustration of the beam divergence. Every particle crosses the silicon strip detector Si1 at position $X1$ ($Z1$) and Si2 at $X2$ ($Z2$). The distribution of the residual $X1 - X2$ ($Z1 - Z2$) is centered at a fixed value due to the misalignment of Si1 with respect to Si2. The width σ of this distribution $\sigma(X1 - X2)$ ($\sigma(Z1 - Z2)$) is a measure of the angular deviation from the nominal direction of the beam.

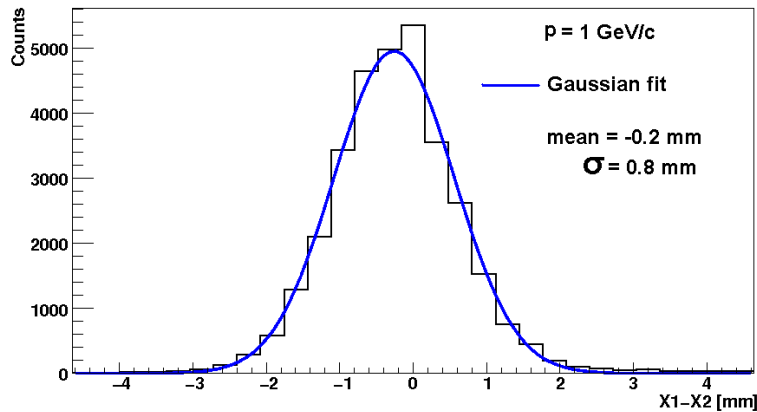


Figure 6.16: Residual in x -direction and the corresponding fit with a Gaussian function (blue solid line).

were not perfectly aligned to each other neither in x - nor in z -direction. Tabular 6.1 summarizes the extracted beam parameters, the widths in x - and z -direction each represented by the FWHM, which describe the size of the beam spot. The widths σ_{ϕ} and σ_{θ}

describing the beam divergency are also listed. For each extracted value for the width the used fit function and the reduced χ^2 of the fit are given. With rising beam energy a clear decreasing of the beam dimensions and the beam divergency is observed. The reason for

p[GeV/c]	width in x (FWHM) [cm]	width in z (FWHM) [cm]	σ_θ [deg.]	σ_ϕ [deg.]
1	5.23 (g,1.1)	4.00 (g,1.2)	0.184	0.175
2	4.76 (p,1.3)	2.70 (g,1.5)	0.130	0.133
4	3.86 (p,1.7)	2.26 (g,2.5)	0.096	0.106
6	3.68 (p,2.1)	1.69 (g,3.3)	0.093	0.099

Table 6.1: Overview of the extracted beam parameters at different beam momenta. The character in parentheses indicates the used fit function - "g" for Gaussian function and "p" for parabola. The number in parentheses after each character is the reduced χ^2 of the fit.

this is, that particles that arrived at the silicon strips had traversed a long distance in air, as shown in Fig. 6.1. As a result, they experienced multiple Coulomb scattering. The mean angular deviation after traversing a fixed path length is proportional to $1/E_{\text{particle}}$ for highly energetic particles.

6.2.3 Lead glass calorimeter data

The most important detector for this thesis is the lead glass calorimeter. The initial idea was, in order to measure the radiation thickness of the TRD, to create an energy spectrum for the electrons that crossed the TRD using the information of the lead glass calorimeter. Since the energy before crossing the TRD was the beam energy, the opinion was that the radiation thickness was extractable from the energy spectrum after crossing the TRD. Therefore, the lead glass data was extensively investigated.

Lead glass spectra without particle identification

The first created histograms were non biased lead glass spectra except for the trigger on charged particles and sometimes the involved lead glass trigger as shown in Fig. 6.6. As an example, two of them are shown in Fig. 6.17 and Fig. 6.18. Figure 6.18 shows an ADC spectrum of a run at a beam momentum of $p = 6$ GeV/c, during which the lead glass was not involved in the trigger decision and therefore counts are visible down to ADC-channel 200, which was the pedestal or offset value of the lead glass calorimeter. In contrary, Fig. 6.17 shows an ADC spectrum of a run with the lead glass detector involved in the trigger decision, where a cut is visible at an ADC value around channel 1500 due to the lead glass trigger cut, which rejected all events with an ADC value below 1500. The single counts below ADC-channel 1500 are due to the fact, that when the lead glass was involved in the trigger decision, a cut on the **amplitude** of the lead glass took place, whereas the ADC values in the spectrum are the **integral** of the signal.

In both cases shown in Fig. 6.17 and in Fig.6.18 two peaks are visible. The left one is due

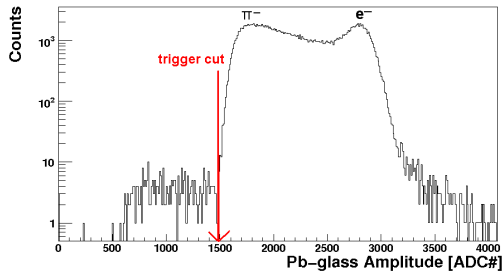


Figure 6.17: Lead glass signal with the lead glass calorimeter part of the trigger decision at a beam momentum $p = 6 \text{ GeV}/c$.

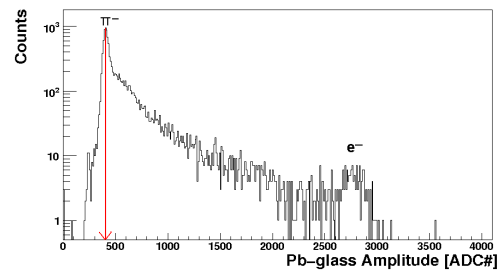


Figure 6.18: Lead glass signal with the lead glass calorimeter **not** part of the trigger decision at a beam momentum $p = 6 \text{ GeV}/c$.

to pion events and the right one is due to electron events. The two main differences between the two distributions are the following.

1. The ratios of the pion and the electron events are different.
2. The pion peak is located at different positions and the shape of the distribution for the pions looks different.

The reason for point one is that the ratio of the pion to electron yield depends dramatically on inclusion of the lead glass in the trigger decision, whereas inclusion means favoring electron events.

The reason for point two is that only in Fig. 6.18 the "real" pion peak is visible, i.e. the most probable ADC value a pion produces in the lead glass calorimeter is about at channel 400 at the position of the peak on the left side. Pions do not create a shower in the lead glass calorimeter but nevertheless emit Cherenkov radiation, which is detected by the photo cathode. In contrary, in Fig. 6.17 not the real pion peak is visible but only the high energetic branch of the pion ADC distribution which is cut on its right side at ADC-channel 1500 and therefore looks like a peak.

At all other beam momenta the distributions look similar besides the fact that the peak of the electrons moves towards lower ADC values with decreasing beam momentum. This is due to the fact that with decreasing beam momentum the electrons produce smaller showers within the lead glass calorimeter thus inducing smaller signals. Switching on and off the lead glass trigger naturally affects the spectra at all other beam momenta the same way as discussed above. Moreover, data was also recorded with the silicon strip detectors in the beam line, which had a non-negligible average radiation thickness X/X_0 of about 2.5% each. An overview of the different experimental setups is shown in Tab. 6.2.

p [GeV/c]	Pb. trigger cut ON	OFF	Si. in beamline	Si. not in beamline
0.3	NO	YES	NO	YES
0.6	NO	YES	NO	YES
1.0	NO	YES	YES	YES
1.5	NO	YES	NO	YES
2.0	YES	YES	YES	YES
3.0	YES	NO	NO	YES
4.0	YES	NO	YES	NO
6.0	YES	NO	YES	NO

Table 6.2: Overview of the experimental setup at different beam momenta. YES means that this setting is available, NO means that it is not available. Pb.: lead glass calorimeter; Si.: silicon strip detectors.

Lead glass spectra of electrons

In the next analysis step lead glass spectra with a cut on the Cherenkov ADC-channels were produced, i.e. switching on particle identification and selecting electrons. The proper value for the Cherenkov ADC-channel to identify electrons was described in Sect. 6.2. The distributions after electron identification are shown for different beam energies E_0 in Fig. 6.19 for $E_0 = 1$ GeV without lead glass trigger cut, in Fig. 6.20 for $E_0 = 2$ GeV without lead glass trigger cut, in Fig. 6.21 for $E_0 = 4$ GeV with lead glass trigger cut and in Fig. 6.22 for $E_0 = 6$ GeV with lead glass trigger cut. For electrons with $p \geq 1$ GeV/c

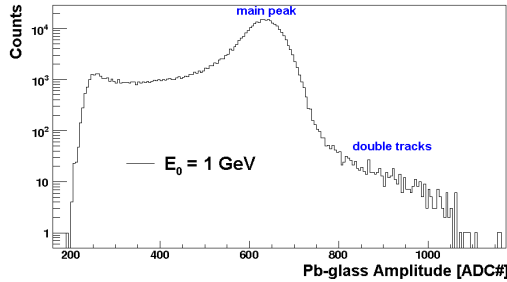


Figure 6.19: Lead glass signal at a beam energy $E_0 = 1$ GeV without lead glass trigger cut.

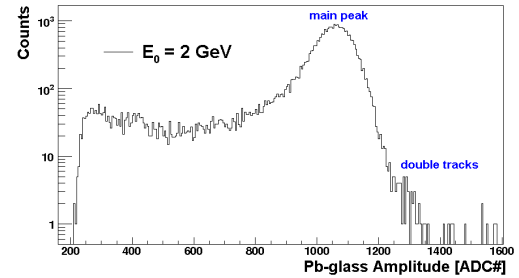


Figure 6.20: Lead glass signal at a beam energy $E_0 = 2$ GeV without lead glass trigger cut.

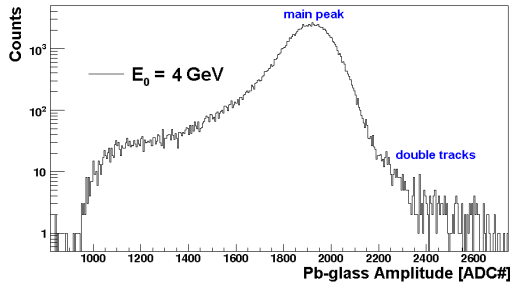


Figure 6.21: Lead glass signal at a beam energy $E_0 = 4$ GeV with lead glass trigger cut.

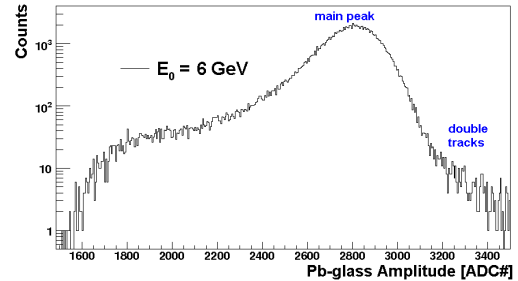


Figure 6.22: Lead glass signal at a beam energy $E_0 = 6$ GeV with lead glass trigger cut.

the energy E_0 is given by $E_0 = p$ since the rest mass of electrons $m_e = 0.5 \cdot 10^{-3}$ GeV/ c^2 is

negligible in this momentum range. As from now, only ADC-distributions of electrons are discussed. Therefore, the expression "beam momentum p " is replaced by the expression "beam energy E_0 " in the following and at the end of this chapter an ADC-channel-to-energy calibration is described.

At first glance the distributions shown in Figs. 6.19, 6.20, 6.21 and 6.22 look as expected. The main peak that moves to higher ADC-channels with increasing beam momentum is due to electrons that have not emitted Bremsstrahlung photons in the TRD but lost a small fraction of their energy due to ionization. The broadening of the main peak is caused by the finite detector resolution, whereas the branch to high ADC values is caused by having more than one particle in one event. The branch down to small ADC values was thought to be due to electrons that emitted hard Bremsstrahlung radiation inside the TRD material. Hence, when neglecting energy loss due to ionization a good approximation of these spectra was thought to be the Bethe-Heitler energy straggling function as shown in Fig. 2.7, additionally convoluted with a Gaussian function. This convolution is needed because the lead glass calorimeter has a finite resolution. This resolution is discussed and parametrized at the end of this chapter. The radiation thickness $X/X_0 = c \cdot \ln 2$ in the Bethe-Heitler function (see Eq. (2.12)) is a free parameter in this case and by fitting the convolution of the Gaussian function and the Bethe-Heitler function to the measured ADC-distributions the average radiation thickness X/X_0 is extractable. Initially, this was the road map to extract the average radiation thickness from the data. However, in order to simulate as many effects as possible that influenced the experimental spectra, e.g. the finite acceptance of the lead glass calorimeter, another approach was chosen. A detailed Monte Carlo simulation based on GEANT3 and the ALICE Offline Project AliRoot was developed to create these spectra. Details are discussed in Chap. 7 and a comparison to Monte Carlo data is given in Chap. 8. It will become clear in Chap. 8 that the detailed Monte Carlo approach turned out to be the better choice. During these studies it became clear that the long tail down to small ADC values was mainly driven by transversal leakage within the lead glass calorimeter and only little by electrons, which suffered Bremsstrahlung processes.

Biased lead glass data

In order to understand the measured electron spectra, in addition to particle identification further cuts were applied and the effects of these cuts were investigated. For instance, only electrons which hit both silicon strip detectors were selected. In Fig. 6.23 for a beam energy $E_0 = 1$ GeV the effect of selecting only electrons that hit both silicon strip detectors is demonstrated. In Fig. 6.24 the same effect is shown for a beam energy $E_0 = 2$ GeV. In both histograms the red distribution represents the sample of electrons hitting the active volume of the silicon strip detectors. The blue distribution represents the unbiased electron sample in terms of a position information bias. At both beam energies a decrease of the counting rate left to the main peak is noticeable if only electrons are selected which hit the active material of the silicon strip detectors. This happens because electrons from the central part of the beam are selected and hit the lead glass calorimeter rather centrally thus causing less lateral leakage within the lead glass calorimeter. Another reason for this behavior is that particles which traverse the silicon strip detectors through their active silicon material experience an additional radiation thickness of $X/X_0 \approx 1.2\%$. In contrary,

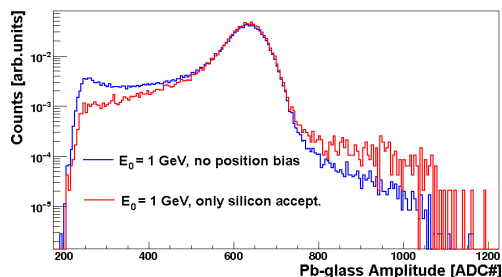


Figure 6.23: Lead glass signal (electrons) at $E_0 = 1$ GeV without the lead glass calorimeter in the trigger decision. ADC values for all electrons which hit the two scintillators Sci1 and Sci2 (blue line). ADC distribution of the electrons which additionally hit the active material of both silicon strip detectors (red line). For comparison both distributions are normalized to unity.

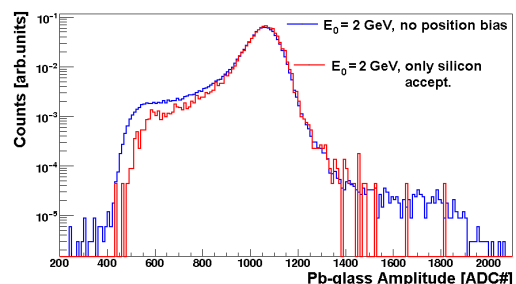


Figure 6.24: Lead glass signal (electrons) at $E_0 = 2$ GeV with the lead glass calorimeter in trigger decision. ADC values for all electrons which hit the two scintillators Sci1 and Sci2 (blue line). ADC distribution of the electrons which additionally hit the active material of both silicon strip detectors (red line). For comparison both distributions are normalized to unity.

particles that traverse the silicon strip detectors through their active silicon material and accidentally sometimes hit the aluminium frame of the detectors experience an additional average radiation thickness of $X/X_0 \approx 5\%$.

Further at a beam energy of $E_0 = 1$ GeV the highly energetic branch right to the main peak of the red biased distribution representing the electron sample traversing the active material of silicon strip detectors rises in comparison to the blue unbiased distribution. This is most probably due to the fact that the particle density in the central part of the beam is higher and thus the probability to get two particles in one event is higher as well. For a beam energy of $E_0 = 2$ GeV the highly energetic branch carries too little statistics for a further analysis.

The influence of the complete removal of the silicon strip detectors from the beam line was also studied. In Fig. 6.25 three different distributions normalized to unity are drawn

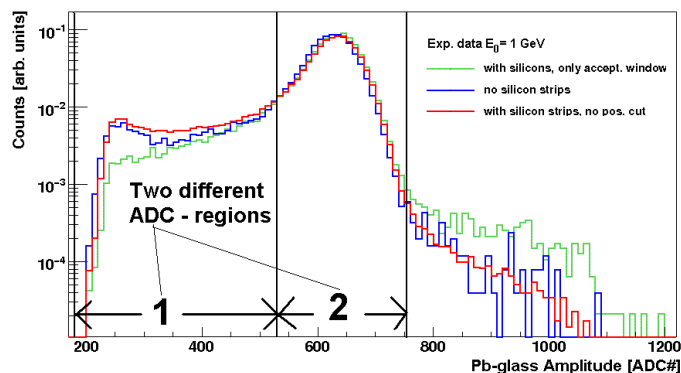


Figure 6.25: The lead glass signal for electrons at a beam energy $E_0 = 1$ GeV/c, normalized to unity. All electrons of a run with the silicon strip detectors in the beam line (red line). The same conditions but now selecting only electrons that hit the active material of the silicon strip detectors (green line). All electrons of a run with no silicon strip detectors in the beam line (blue line).

in one histogram. The red and the green distributions are the same as in Fig. 6.23 but the blue one is a new distribution, showing the ADC spectrum of electrons of one special run, during which the silicon strips were removed from the beam line. Here, a suppression of the low energetic branch in comparison to the distribution of the run with the silicon strip detectors in the beam line is also noticeable. This is due to the fact that the electrons have to cross less material when the silicon strip detectors are not in the beam line. In order to compare the three different cases on an absolute scale, three different ratios $R = R1/R2$ have been calculated. The value $R1$ denotes the total number of events in Region 1 depicted in Fig. 6.25 ranging from ADC-channel 180 to ADC-channel 530. The value $R2$ denotes the total number of events in Region 2 ranging from ADC-channel 531 to ADC-channel 750. Results for R for the three cases described above are shown in Tab. 6.3. As a result, the low energy spectrum at ADC-values below channel 530 is

Ratio $R = R1/R2$	experimental setup
0.354	Silicons in beam line, no position cut
0.327	Silicons not in beam line
0.244	Silicons in beam line, e- traversing the active material

Table 6.3: Overview of the ratio R , which is the number of low ADC-events divided by the number of high ADC-events, for different experimental setups.

more sensitive to changes in the geometry of the beam than to significant changes in the material budget the beam particles had to cross. The ratio R decreases by 31%, namely from $R = 0.354$ to $R = 0.244$, if electrons are selected that crossed the silicon strip detectors through their active silicon material. On the other hand, the complete removal of the silicon strip detectors with a radiation thickness of $X/X_0 \approx 5\%$ leads only to a decrease of ratio R of 8%, namely from $R = 0.354$ to $R = 0.327$. Hence, only detailed Monte-Carlo simulations are suitable for an estimation of the effects mentioned above. These simulations are described in Chap. 7.

Energy-ADC calibration

Another section of the analysis was dedicated to the calibration of the ADC values of all histograms shown in the previous subsections, i.e. to convert the ADC values to energy values. For this purpose Gaussian functions were fitted to the central parts of the main peaks. The corresponding distribution including the obtained Gaussian function is shown in Fig. 6.26 for a beam energy of $E_0 = 4$ GeV. The ADC value of the mean of the Gaussian

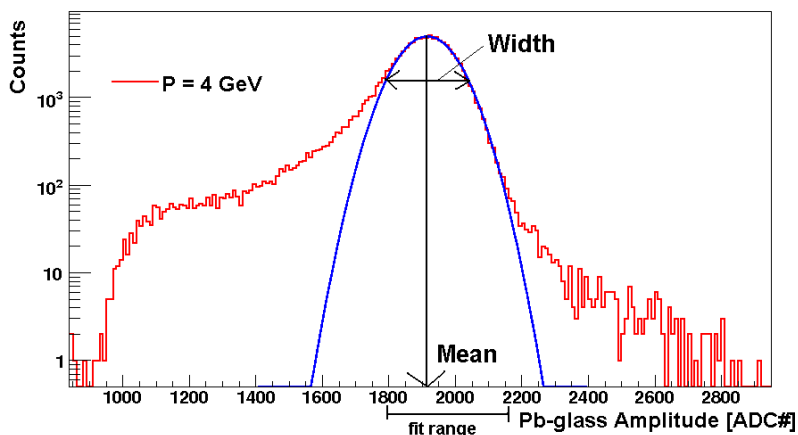


Figure 6.26: The ADC spectrum of the lead glass at for a beam momentum of $E_0 = 4$ GeV (red solid line) and a Gaussian fit (blue solid line) to the main peak. The position of the mean, the fit range and the width are indicated.

fit was assigned to the according beam energy. This is a valid approximation because in the main peak there are only electrons that have lost a rather small fraction of their energy in the TRD and in the silicon strip detectors due to ionization. The energy loss for minimum ionizing electrons due to ionization traversing the silicon strips and the TRD is in the order of some MeV and does not exceed 10 MeV. This is less than 1% of the initial beam energy. A list of the obtained mean ADC values and the corresponding beam energy values are shown in Tab 6.4. The uncertainty in the initial beam energy is $\sigma_i = E_i \cdot 1\%$ [41] and the

Energy [GeV]	Position [ADC#]
1.0	633.5 ± 4
1.5	848.0 ± 4
2.0	1061.0 ± 8
3.0	1474.0 ± 5
4.0	1920.5 ± 11
6.0	2823.0 ± 15

Table 6.4: Position of the mean of the Gaussian function in ADC for different beam energies.

errors of the corresponding ADC mean values were estimated by determining these values for different runs. The statistical fit error of the mean value of the Gaussian function was always below one ADC channel and thus neglected. The result of this energy calibration is shown in Fig. 6.27. A linear fit function $E_0 = a \cdot ADC + b$ was used to describe the data points. The reduced χ^2 , given by $\chi_{\text{red}}^2 = \chi^2/\text{NDF}$ of the fit is 0.88, showing clearly a linear dependence of energy and ADC mean value. The results of the linear fit constants slope a and offset b are:

- slope $a = 0.00232 \pm 0.00002$
- offset $b = -0.467 \pm 0.018$

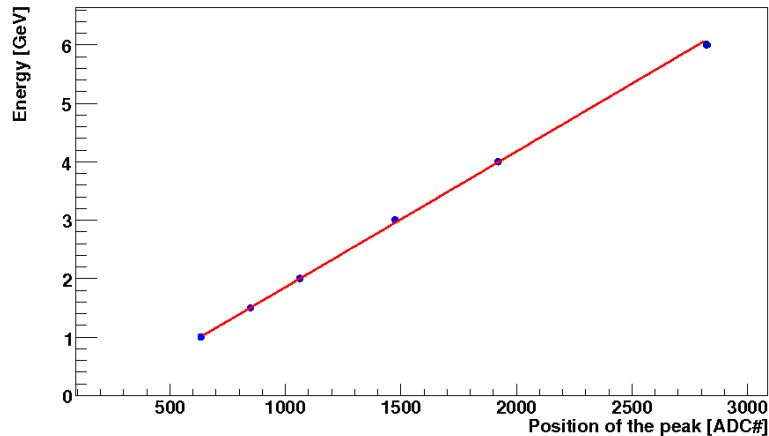


Figure 6.27: Energy in the lead glass calorimeter as a function ADC channel. The solid line shows the result of the linear fit.

Energy resolution

In order to determine an energy dependent resolution curve $\frac{\sigma(E)}{E}$ as input for the Monte-Carlo simulations described in Chap. 7 of the lead glass calorimeter, the widths of the peaks at different beam energies were determined in units of ADC channels as shown in Fig. 6.26. These widths in units of ADC channels were converted to widths in units of GeV making use of the results of the energy-ADC-calibration described above. The obtained values for the relative resolution at different beam energies as well as the widths in ADC channels are summarized in Tab. 6.5. The uncertainty of the beam energy is the same as in case of the energy-ADC-calibration and for the relative resolution the error

Beam energy [GeV]	σ_{ADC} [ADC#]	$\sigma(E)/E$ [%]
0.3	20 ± 2	15.5 ± 1.5
0.6	27 ± 2	10.5 ± 0.8
1.0	33 ± 2	7.7 ± 0.5
1.5	39 ± 3	5.9 ± 0.5
2.0	49 ± 2	5.7 ± 0.2
3.0	61 ± 4	4.7 ± 0.3
4.0	$70 \pm_3^1$	$4.1 \pm_{0.2}^{0.1}$
6.0	98 ± 2	3.8 ± 0.1

Table 6.5: Relative resolution values and widths in ADC for different beam energies.

bars in units of ADC channels were estimated by varying the fit range and by determining the width of the distributions for different runs. The resolution parameterization curve for homogeneous calorimeters as given in Eq. (3.8) was fitted to the data points. The relative resolution as a function of energy and the fit depicted as a red curve are shown in Fig. 6.28. The reduced χ^2 of the fit was 1.25 showing good accordance between the resolution parameterization and the data points. The resulting values for the three fit

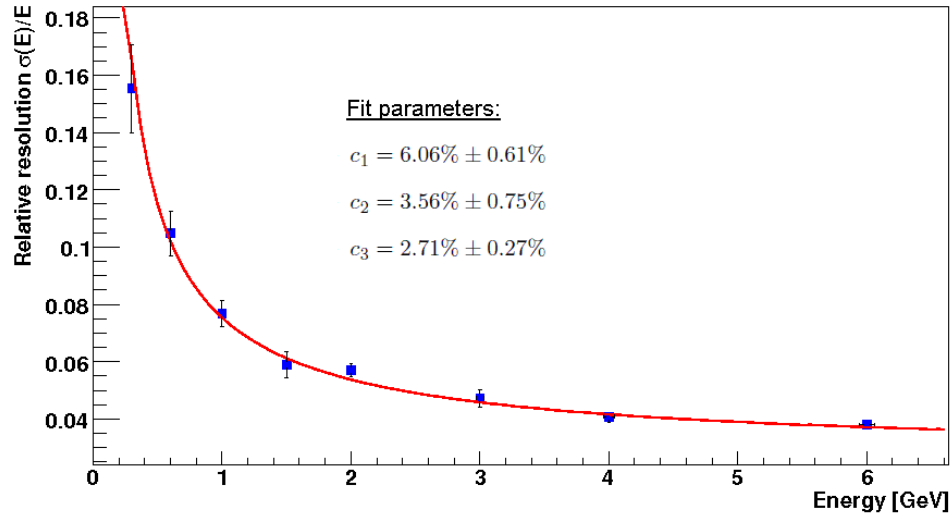


Figure 6.28: Relative resolution $\sigma(E)/E$ as a function of energy (data points) and fit (solid line) by the resolution parametrization curve for homogeneous calorimeters as given in Eq. (3.8).

constants of Eq. (3.8) given by $\frac{\sigma(E)}{E} = \sqrt{\frac{c_1^2}{E} + \frac{c_2^2}{E^2} + c_3^2}$ are

- $c_1 = 6.06\% \pm 0.61\%$
- $c_2 = 3.56\% \pm 0.75\%$
- $c_3 = 2.71\% \pm 0.27\%$.

7 Simulation of the Testbeam data

In order to simulate the data taken during the Testbeam 2007 detailed Monte Carlo simulations were developed. The aim was to simulate the electron spectra measured by the lead glass calorimeter. In these Monte Carlo simulations the average radiation thickness of the TRD is a free parameter. The best fit to the experimental data was expected to determine the radiation thickness X/X_0 of the TRD. This fit procedure is described in Chap. 8. In order to simulate the testbeam properly, the following details were taken into account:

1. Simulation of an **electron particle beam** with the beam dimensions and beam divergence measured by the silicon strip detectors as given in Tab. 6.1. Here, it was taken into account that the silicon strip detectors do not measure the real beam dimension and beam divergence. The shape of the transversal position distribution, which is measured by the silicon strip detectors, is influenced by the two scintillation trigger detectors due to their limited acceptance. The particle sample consisted of electrons that traversed the active material of both scintillation trigger detectors through their active material.
2. Simulation of the **material budget** along the beam line, e.g. air, TRD, scintillation detectors.
3. Simulation of the **energy loss, scattering, etc.** in the material along the beam line.
4. Propagation of **secondary particles** such as Bremsstrahlung photons and secondary electrons produced in the material along the beam line and simulation of the corresponding interaction with matter.
5. Implementation of the **trigger** (logic).
6. Realistic treatment of the **detector response** of the lead glass calorimeter.
7. Simulation of the correct **angles** of the incident beam with respect to the TRD. The azimuthal angle was $\Phi = 10$ degrees with respect to the y -axis as shown in Fig. 7.1 and the polar angle was $\Theta = 16$ degrees with respect to the y -axis.

A sketch of the experimental setup is shown in Fig. 7.1. In order to consider all details, an already existing C++ software framework based on ROOT [42], GEANT3 and the ALICE Offline Framework AliRoot was modified and applied. Some basics about the software package, which are important for this thesis are described in the following section.

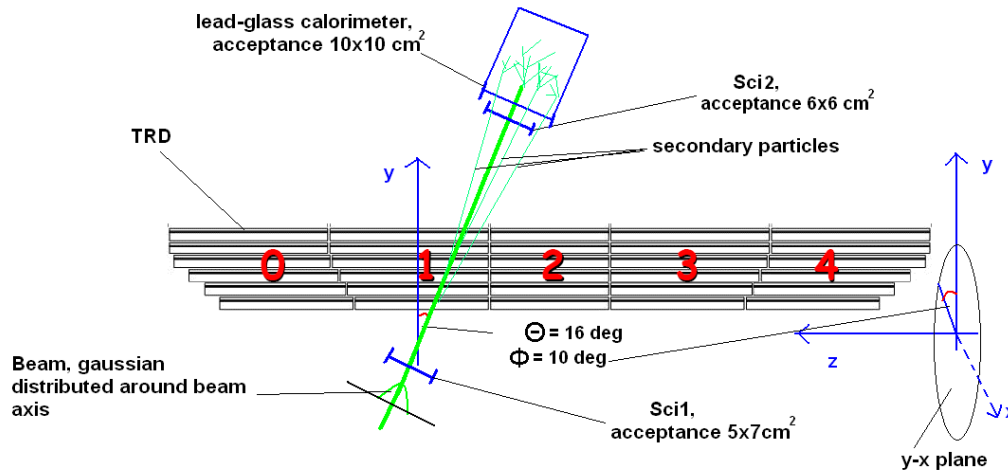


Figure 7.1: Schematic view of the experimental setup as implemented in the Monte Carlo simulations. Sci1, Sci2: scintillation trigger detectors. TRD: one supermodule of the TRD. The lead glass calorimeter, secondary particles, the beam and the coordinate system are depicted. The silicon strip detectors are not shown since they were not included in the simulation. See text for more details.

7.1 Software framework

7.1.1 AliRoot

The ALICE Offline Framework AliRoot is a powerful software framework based on the ROOT [42] framework. The main functionalities of AliRoot are:

- Particle generation via Monte-Carlo event generators.
- Particle propagation.
- Detector geometry and detector response.
- Digitization of the detector response - data format like in real data.
- Reconstruction of the simulated or real data.
- Analysis of the reconstructed simulated or real data; the final data format is called Event Summary Data (ESD).

The flow diagram of the AliRoot framework is depicted in Fig. 7.2. More details about AliRoot can be found in [39]. For the simulation of the Testbeam 2007 only a small fraction of the full functionality of the AliRoot framework was applied, which is marked red in Fig. 7.2. These are:

- Event generation / particle production.
- Simulation of the geometry of the ALICE detectors. Here, only the geometry and the material budget of the TRD detector were implemented.

- Particle transport in the detector material and simulation of their interaction with matter.

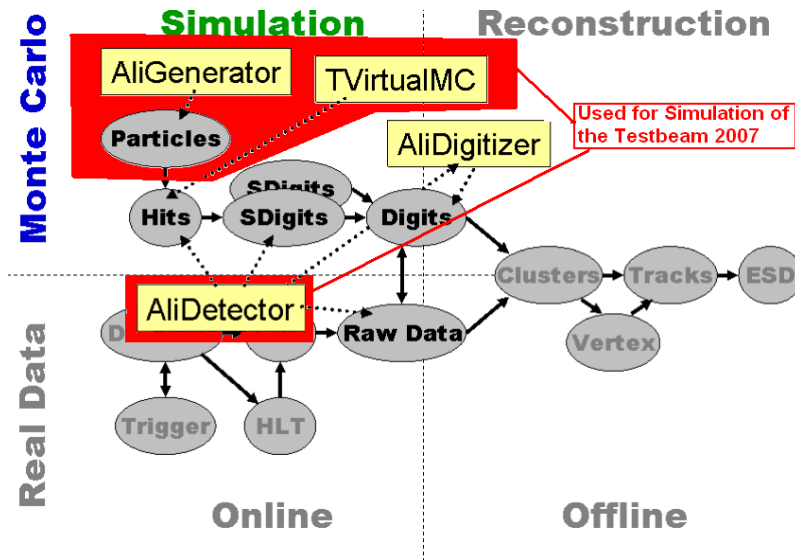


Figure 7.2: Flow diagram of the AliRoot framework. For the simulation of the Testbeam 2007 only a small fraction of the AliRoot functionality (marked red) was modified and applied. This figure has been taken from [44].

All other functions of AliRoot such as signal generation, digitization (see Fig. 7.2) were not applied within this thesis. A more detailed schematic flow diagram of the used AliRoot code, which is marked red in Fig. 7.2, is shown in Fig. 7.3. This part of the code was modified, in order to include the other detectors of the Testbeam 2007, e.g. the scintillation trigger detectors or the lead glass calorimeter. These modifications are discussed later. The most important class of this part of the code is **TVirtualMC**, which is the base class

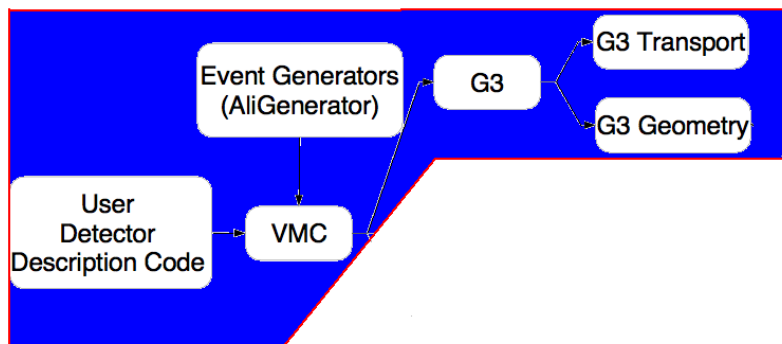


Figure 7.3: Tools within the AliRoot framework applied for the Testbeam 2007 simulation. "G3" denotes GEANT3 and "VMC" Virtual Monte Carlo (see text for more details). This figure has been taken from [44].

for the so called Virtual Monte Carlo (VMC) structure within the AliRoot framework. A detailed description of the Virtual Monte Carlo is given in [43]. The Virtual Monte Carlo structure steers the interaction between the detector description performed by the

class **AliDetector**, particle generation performed by the class **AliGenerator** and particle transport which is done by the program **GEANT3** described in the next subsection. Since **GEANT3** was written in FORTRAN and not in C++, it requires the special interface class **TGeant3** in order to be able to interact with AliRoot. For particle production there are many, sometimes rather complex, event generators available, which parameterize particle distributions for e.g. proton-proton or lead-lead collisions. For this thesis the simple particle generator **AliGenBox** was used, which generates a defined particle species with a defined energy. The position of particle generation, which is defined by three coordinates x , y and z as well as the flight direction defined by two angles Φ and Θ are smeared according to a Gaussian function. The individual width σ of the five variables was set independently.

7.1.2 GEANT3

The core of the Testbeam 2007 simulation is the program **GEANT3** (**Geometry and Tracking**). **GEANT3** is used to simulate the energy loss as well as the creation of secondary particles, applying a Monte-Carlo algorithm, when particles of different species traverse any kind of material. The cross section tables for different energy loss processes are tabularized for different energies of the incident particle. The main processes implemented in **GEANT3** such as cross sections for Bremsstrahlung or cross sections for energy loss of photons are described in detail in Chap. 2. Another important part of the Monte Carlo approach are random number generators. These random number generators and the cross sections interact in **GEANT3** as follows. The probability P_i of a particle not to undergo an interaction i with its according cross section σ_i during a path length x_i is given by

$$P_i = e^{-\eta} \quad \text{with } \eta \propto x_i \cdot \sigma_i \quad (7.1)$$

$$\rightarrow -\ln P_i = \eta \quad \text{with } P_i \in [0, 1].$$

GEANT3 generates a random number between zero and one, whereas the probability for all numbers in the interval $[0,1]$ is equal. This yields a value for η . Thus for each interaction i a value for x_i can be computed, which is different for each interaction. The interaction with the smallest value for x_i is then regarded as occurred and the so called *step length* is set to x_i . The considered particle is transported over a distance x_i . Moreover, continuous processes are considered that occur during the step length, e.g. continuous energy loss due to ionization. At the end of each step the particle parameters such as energy or flight direction are updated. This is done for so called *primary particles*, which are generated with the available particle generators in AliRoot and for *secondary particles* which are produced due to the interaction of the primary particles with the detector material, e.g. Bremsstrahlung photons. More details about **GEANT3** can be found in [47].

7.2 Simulated experimental setup

In order to simulate the experimental setup of the Testbeam 2007 besides one supermodule of the TRD all detectors of the TRD Testbeam 2007 except the Cherenkov detector and the silicon strip detectors were placed in a three-dimensional coordinate system as shown in Fig. 7.1. The axes of this coordinate system are defined by the TRD supermodule

as follows. The y -axis is perpendicular to the chambers and the z -axis is parallel to the longitudinal dimension of the TRD supermodule. The x -axis is perpendicular to the y - and z -axis pointing out of the sheet of paper.

The Cherenkov detector was not considered in the simulation because its amount of material in the beam line was mainly consisting of air and thus negligible. The silicon strip detectors were not considered because their contribution to the total radiation thickness X/X_0 in the beam line was very hard to estimate due to their complicated inner structure. As real testbeam data without the silicon strip detectors in the beam line was available, a comparison between real data and Monte Carlo data was performed as described in Chap. 8. The two scintillation detectors and the lead glass calorimeter were aligned along a nominal beam line as shown in Fig. 6.2 with the proper distances to each other and the beam line centered in the middle of the acceptance of each detector. The nominal beam line shown in Fig. 7.1 in the coordinate system had the same direction and crossing position with respect to the TRD supermodule as during the Testbeam 2007. This information has been taken from [46]. Another coordinate system was defined by the nominal beam line, whereas the beam line was parallel to the y' -axis of the second coordinate system. The x' -axis and the z' -axis were defined by the transversal acceptances of the two scintillation trigger detectors and by the transversal acceptance of the lead glass calorimeter. The particles were generated in a plane perpendicular to the nominal beam line directly in front of the first trigger detector Sci1, which is depicted in Fig. 7.4. An event was defined by the generation of one particle. The position of particle generation described by two coordinates x_0 and z_0 as well as the flight direction described by two angles Φ_0

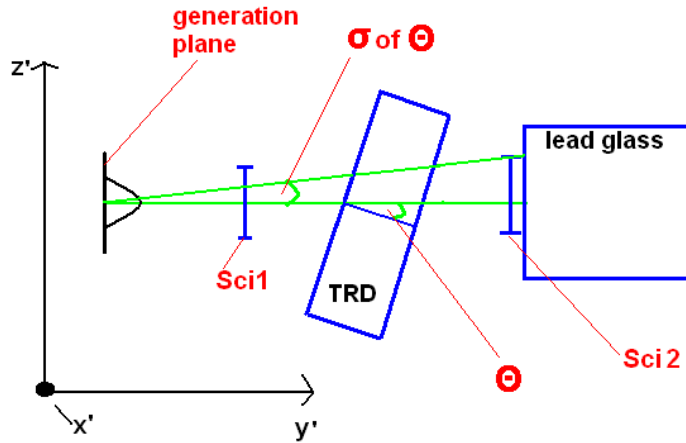


Figure 7.4: Schematic illustration of the detector setup implemented in the Monte Carlo simulation and of the generation of the beam electrons. The electrons were generated in front of Sci1 in the x' - z' -plane. A smearing according to a Gaussian function of the two angles Φ_0 and Θ_0 and the generation position x_0 and z_0 event by event is performed. The dimensions are not to scale.

and Θ_0 were smeared around their mean values according to a Gaussian function. That means that event by event a random number generator was used, which determined the flight direction and the point of creation according to a Gaussian function. In order to

simulate the triggering on charged particles, every charged particle was assigned a flag when it entered or exited one of the trigger detectors Sci1 and Sci2. These flags are so called *Track References* which were stored and assigned to the corresponding event and particle. The criterion on reading out an event was that the event had to have at least one charged particle traversing Sci1 and Sci2. All events not fulfilling this criterion were removed from the data sample.

The average radiation thickness X/X_0 of the TRD was varied within the simulation by multiplying the densities ρ_i of all materials within the TRD geometry using a variable factor F . A factor $F = 1$ corresponds to an average radiation thickness of 25.4% of one active stack of the TRD as described in Chap. 5. Since the average radiation thickness is linear in density a factor $F = 0.5$ e.g. corresponds to a radiation thickness X/X_0 of 12.7%. Figure 7.5 shows a radiation thickness map of one supermodule of the TRD for a factor $F = 1$. The abscissa displays the pseudorapidity η , whereas an η of ± 1 corresponds

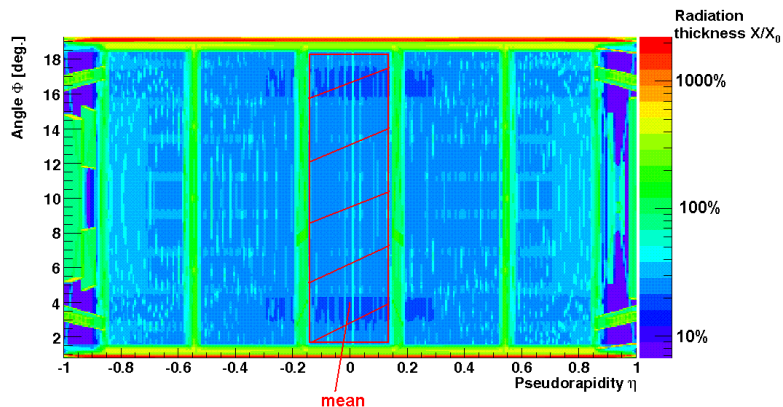


Figure 7.5: Radiation thickness map of one TRD supermodule.

to an polar angle Θ of ± 49.6 degrees with respect to the y -axis in the coordinate system shown in Fig. 7.1. The ordinate displays the azimuthal angle Φ in this coordinate system. When talking about the averaged radiation thickness of the TRD, an average of the red marked area is meant, which is one active stack of the TRD.

The simulation of the signal of the lead glass calorimeter was the most challenging part of the Monte Carlo simulation. First, the signal of the lead glass was considered to be proportional to the energy of the electrons that traversed the material of the TRD and hit the geometrical acceptance of the lead glass calorimeter during one triggered event. Then it turned out that this approximate signal simulation is not accurate enough to describe the experimental data and thus another approach was chosen. Results will be shown in the next section. During the new approach the whole electromagnetic shower within the lead glass calorimeter occurring due to the impact of highly energetic leptons and photons was simulated. A block with the dimensions of $10 \times 10 \times 35 \text{ cm}^3$ consisting of lead glass was placed at the position of the lead glass calorimeter in the experimental setup. In order to have access to the information about the **total track length L of charged particles** within the electromagnetic shower, every charged particle that performed the first step in the lead glass material during one event was flagged and a Track Reference was assigned at that position to the particle. Such a particle has three possibilities do disappear out of

the lead glass block volume.

- It disappears due to an inelastic collision, e.g. due to positron annihilation.
- The energy of the particle falls below a defined energy threshold. In the simulation this energy cutoff was set to $E_{\text{kin}} = 100$ keV because this is the energy threshold for Cherenkov radiation production in lead glass. The refraction index of lead glass is $n = 1.7$.
- The particle leaves the lead glass material without being completely stopped thus causing leakage.

In all of the three cases the particle was flagged and again a Track Reference was assigned to it. Besides energy, momentum and position information such a Track Reference provides information about the total path length already traversed in the simulated experimental coordinate system. Thus, the traversed track length l_i within the lead glass block is extractable for every particle by subtracting the two length values at the two flagged positions. The sum $L = \sum l_i$ for one triggered event is the total track length L of charged particles within the electromagnetic shower in the lead glass calorimeter.

7.3 Results of the Monte-Carlo simulations

The development of the Monte Carlo simulation of the Testbeam 2007 is separated in two main methods.

1. Development of a **fast** simulation including only the simulation of the energy loss within the material of the TRD supermodule and the limited acceptance of the scintillation trigger detectors as well as of the lead glass calorimeter.
2. Development of a **full** simulation including the following effects:
 - Energy loss of the primary electrons in the material of the TRD and the two scintillation trigger detectors.
 - The acceptance of the two scintillation trigger detectors Sci1 and Sci2 as well as the lead glass calorimeter.
 - Secondary particle production in the material of the TRD and in the material of the two scintillation trigger detectors.
 - The detector response of the lead glass calorimeter by simulating the electromagnetic shower.

Simulated data produced by applying both methods was compared with the real testbeam data, which is described in Chap. 8. It turned out that the first method does not reproduce the testbeam data over the full energy range. Thus the results of the second method are presented in detail while the presentation of the first method is kept brief.

7.3.1 Fast simulation

The first aim of the simulation was to create an energy spectrum of the electrons after traversing the material of the TRD. For this purpose electrons with a fixed energy were generated and transported through the material of the TRD supermodule. The azimuthal and polar angle as well as the impact position on the TRD were equal to the situation during the Testbeam 2007. In Fig. 7.6 the energy distributions of electrons after traversing one supermodule of the TRD at two different incident energies $E_0 = 1$ GeV and $E_0 = 6$ GeV are shown. The main energy loss for electrons in this energy range is Bremsstrahlung.

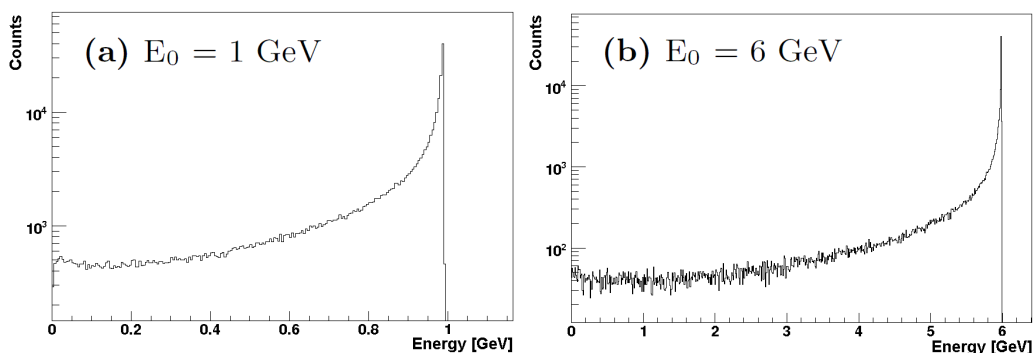


Figure 7.6: Simulated energy spectra of electrons after traversing one supermodule with an incident energy $E_0 = 1$ GeV (a) and $E_0 = 6$ GeV (b).

Therefore these spectra resemble the Bethe-Heitler Bremsstrahlung straggling function as shown in Fig. 2.7 because all the other energy loss processes such as ionization including δ -rays are negligible in comparison to Bremsstrahlung in this energy region. In a "perfect" experiment neglecting secondary particles produced in the material of the TRD the energy spectrum of the electrons, which impact on the lead glass calorimeter, would look similar to the spectra shown in Fig. 7.6. Thus when neglecting leakage the expected lead glass calorimeter signal looks like these distributions additionally folded with the energy dependent resolution curve shown in Fig. 6.28. However, the beam of the Testbeam 2007 had finite spatial dimensions in x' and z' and the scintillation trigger detectors as well as the lead glass calorimeter had a finite acceptance, which introduced bias on the selected electron sample. In order to investigate these effects an electron beam with a width $\sigma = 1.7$ cm in x' - and z' -direction was generated. Next, only electrons were selected which hit the acceptance of Sci1 and Sci2. Electrons, which hit the acceptance of Sci2, never miss the lead glass calorimeter because the scintillation trigger detector Sci2 is mounted directly in front of the lead glass calorimeter as shown in Fig. 6.2. The resulting energy spectrum of the selected electrons is shown in Fig. 7.7 for a beam energy of $E_0 = 1$ GeV. For comparison, the energy spectrum of all electrons without any cut is also shown. In both histograms the area below the distribution is normalized to unity. The distribution with the selected electrons starts to decrease at an energy of about $E = 0.6$ GeV, whereas the unbiased distribution levels off at a constant value. In other words, electrons which have lost a significant fraction of their energy due to Bremsstrahlung change their flight direction and therefore do not hit the trigger detector Sci2 anymore.

In order to simulate the finite resolution of the lead glass calorimeter and create an ex-

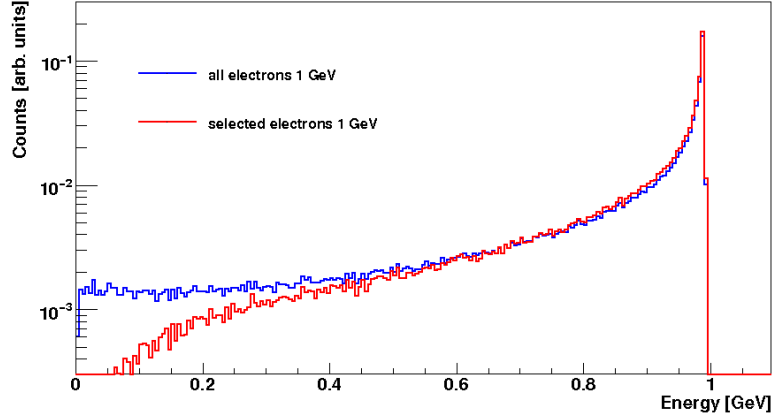


Figure 7.7: Normalized energy spectra of electrons at $E_0 = 1$ GeV which traversed the material of one TRD supermodule. Blue distribution: All electrons. Red distribution: only electrons, that hit the acceptance of Sci1 and Sci2.

pected lead glass calorimeter signal from these energy distributions, the energy values on the abscissa of these spectra were smeared along the abscissa according to a Gaussian function. For this purpose an internal random number generator was used. For each energy value the resolution $\sigma(E)$ of this Gaussian function was set to a calculated value, following the resolution curve $\sigma(E)/E$ shown in Fig. 6.28. The mean of the Gauss-function was set to the bin center energy. In Fig. 7.8 the effect of this procedure is demonstrated. The red energy distribution in this figure is for electrons which traversed the active material of Sci1 and Sci2 similar to the red distribution shown in Fig. 7.7. The green distribution is the energy distribution of the selected electrons after the convolution procedure described above. The difference between both distributions is the different width of the main peak

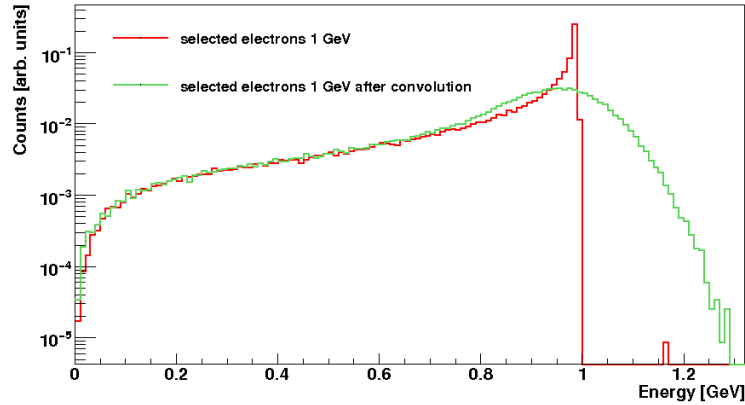


Figure 7.8: The energy distribution of electrons which traversed the acceptance of Sci1 and Sci2 at a beam energy $E_0 = 1$ GeV (red line). The same energy distribution after the convolution procedure described in the text (green line). Both distributions are normalized to unity.

at $E_0 = 1$ GeV. The influence of the variation of the radiation thickness X/X_0 of the TRD

ranging from 17.6% to 25.2% on a sample of selected electrons after the convolution procedure as shown in Fig. 7.8 is shown in Fig. 7.9 for a beam energy of $E_0 = 1$ GeV. The value

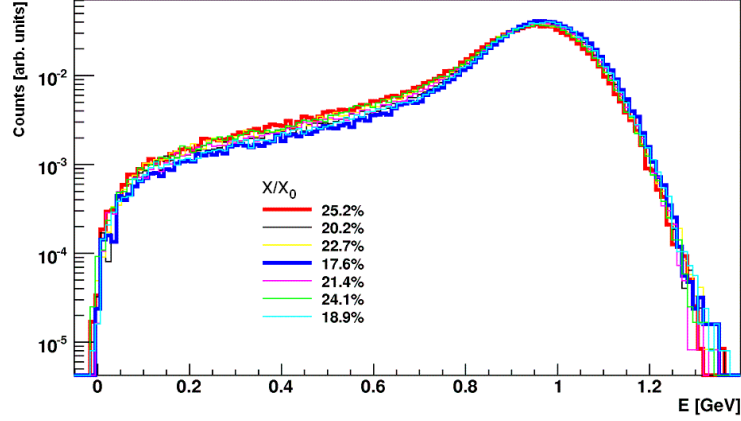


Figure 7.9: Energy spectrum of an electron sample additionally folded with a finite energy resolution at different radiation thicknesses X/X_0 for an incident energy of $E_0 = 1$ GeV. The electron sample consists only of electrons which hit the acceptance of Sci1 and Sci2. The distributions with the highest (red line, $X/X_0 = 25.2\%$) and the lowest (blue line, $X/X_0 = 17.6\%$) radiation thicknesses are drawn in highlighted.

of the radiation thickness affects the low energetic part of the convoluted distribution. It moves slightly up with rising radiation thickness X/X_0 .

7.3.2 Full simulation

The most important effect introduced in the full simulation of the testbeam simulation was the simulation of secondary particles. This allowed a full shower simulation within the lead glass block of the calorimeter and the production of secondary particles within the material of the TRD due to the impact of the primary beam electrons. Figure 7.10 shows the simulated spectrum of the emitted Bremsstrahlung photons of 250.000 electrons which traversed one TRD supermodule. Figure 7.10a shows the energy range from 0 GeV to 1 GeV and Fig. 7.10b shows the energy range from 10 keV to 1 MeV. The maximal

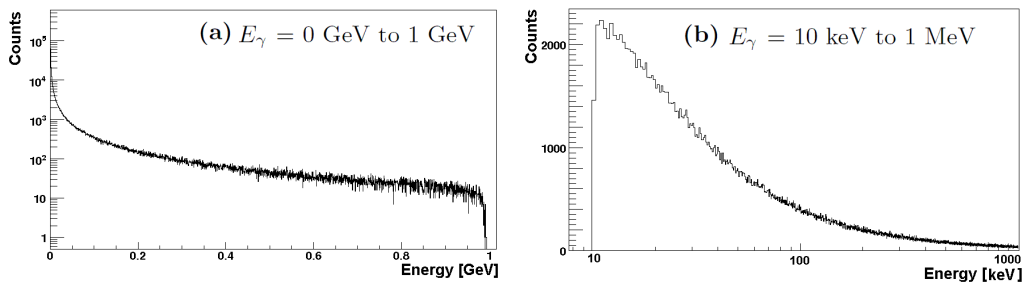


Figure 7.10: Simulated energy spectrum of Bremsstrahlung photons emitted by incident electrons with an Energy of 1 GeV traversing the TRD. Spectrum of all Bremsstrahlung photons (a) and a zoom in showing only the soft Bremsstrahlung photons (b).

energy that an electron with an energy of $E = 1$ GeV can impart on a Bremsstrahlung

photon is $E = 1$ GeV as visible in Fig. 7.10a. Figure 7.10b displays that the minimum photon energy adjustable in GEANT3 is 10 keV since a cut at this energy is observable. Below a photon energy of 10 keV Bremsstrahlung is not treated as a discrete process anymore by usage of cross sections. Instead an average energy loss is computed by means of look-up-tables. Fortunately the energy loss below a photon energy of 10 keV is a negligible fraction of the total energy loss due to Bremsstrahlung. According to these histograms, the mean energy loss per one electron in the total energy range is 215.6 MeV. This corresponds to an experienced radiation thickness of $X/X_0 = 24.3\%$ according to the following calculation:

$$E = E_0 \cdot e^{-X/X_0} \rightarrow X/X_0 = -\ln\left(\frac{E}{E_0}\right) = \frac{1 \text{ GeV} - 215.6 \text{ MeV}}{1 \text{ GeV}} = 24.3\% \quad (7.2)$$

In case of this simulation run the factor F described above was set to $F = 1$. The according mean for $F = 1$ for the average radiation thickness over one active stack of the TRD is $X/X_0 = 25.4\%$ (see Fig. 7.5). The value for the radiation thickness X/X_0 calculated with usage of the spectra shown in Fig. 7.10 is thus lower by 1.1%. This is due to the fact that the value for the radiation thickness $X/X_0 = 25.4\%$ given above is a mean over one stack, whereas the value of $X/X_0 = 24.3\%$ as given in Eq. (7.2) is for electrons which traversed the TRD at a defined position. The position of the beam spot on the TRD is equal to the position as during the Testbeam 2007.

According to Fig. 7.10 the energy loss due to soft Bremsstrahlung in an energy range of 10 keV to 1 MeV is 0.3 MeV and the energy loss due to hard Bremsstrahlung, i.e. in the energy range above 1 MeV is 215.3 MeV per electron. Thus 99.9% of the energy loss due to Bremsstrahlung is caused by hard Bremsstrahlung photons. According to Fig. 2.9, the emission angle of the Bremsstrahlung photons with respect to the flight direction of the primary electron is in the order of 0.2 degrees to 0.6 degrees. Hence, the transversal distance between the primary electron and its according Bremsstrahlung photon is in the order of 0.4 cm to 1.5 cm after a path length of 120 cm, which is the distance from the TRD to the lead glass calorimeter. Thus the lead glass calorimeter with an acceptance of

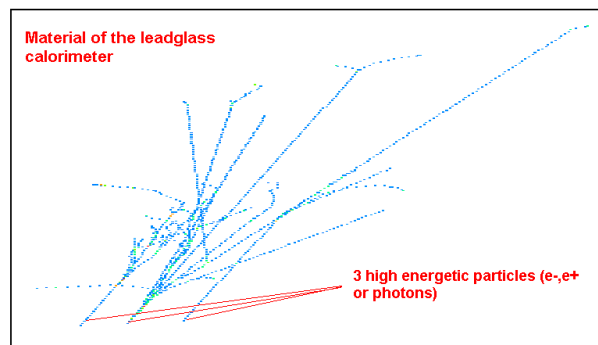


Figure 7.11: Simulated electromagnetic shower in the lead glass calorimeter (one event). The incident electron with an energy of $E_0 = 1$ GeV traversed the TRD and produced at least 2 energetic secondary particles depicted in the figure. The primary electron and the two highly energetic leptons or photons, whereas the particle species is not visible in the figure, hit the lead glass and caused an electromagnetic shower. For better visibility only particles with an energy above 10 MeV are displayed in this figure.

$10 \times 10 \text{ cm}^2$ mainly measures the energy of the primary electron and a fraction of the energy of its corresponding Bremsstrahlung photons. The resulting influence on the simulated lead glass calorimeter signal due to this effect is shown later in this section.

A simulated shower for one event within the lead glass block for an incident electron with an energy of $E_0 = 1 \text{ GeV}$ is shown in Fig. 7.11. For better visibility only particle tracks with an energy above 10 MeV are displayed. Three highly energetic particles each either a lepton or photon hit the lead glass block. They are produced inside the material of the TRD in front of the lead glass calorimeter due to the impact of one beam electron with an energy of $E_0 = 1 \text{ GeV}$. A difference between leptons and photons is not indicated in the picture. Each particle causes a particle shower when entering the lead glass calorimeter volume. In Fig. 7.12 the longitudinal shower profile for an incident particle energy of $E_0 = 1 \text{ GeV}$ is shown. The number of produced charged shower particles as a function of

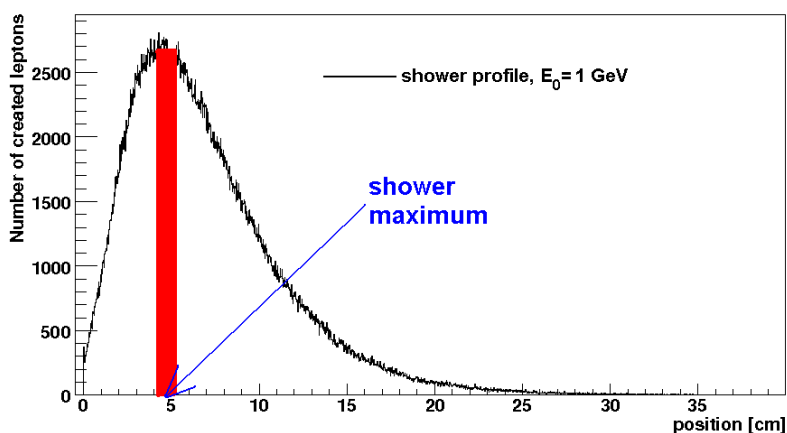


Figure 7.12: Number of created secondary charged particles (electrons and positrons) as a function of the longitudinal coordinate of the lead glass block.

the longitudinal position within the lead glass calorimeter for 500 events is displayed here. The lead glass calorimeter has a depth of 35 cm, which is 28 times the radiation length X_0 of lead glass. This corresponds to a radiation thickness X/X_0 of 2800%. It is observed that there is no longitudinal leakage and that the position of the maximum production rate of charged particles, which represents the shower maximum, is located at around 4 to 6 cm, which is in good accordance with theoretical predictions. According to Eq. (3.3) the shower maximum is located at a position of about 5.3 cm.

Distributions of the total track length L of charged particles

The simulation of the distribution of the total track length L of charged particles was the main aim of the detailed Monte Carlo approach. These distributions of the total track length L of charged particles were namely expected to reproduce the ADC spectra of the lead glass calorimeter shown in Chap. 6. A detailed qualitative analysis of these distributions made clear that the shape of the distributions depends on a large number of parameters, which can be set before each run of data production. Moreover, the influence of the parameter variations on the shape of the distributions of the total track length L

of charged particles are not independent of each other. The most important discovered parameter settings are:

1. The absolute values for the polar angle Θ and the azimuthal angle Φ (see Fig. 7.1 and Fig. 7.4) of the generated particles in front of the first trigger detector Sci1.
2. The widths $\sigma_{\Theta, \Phi}$ of the angle values (see Fig. 7.4) of the generated particles in front of the first trigger detector Sci1.
3. Switching off and on the generation and tracking of secondary particles produced within the material of the TRD due to the impact of the primary beam electrons. In **both** cases the energy loss of the primary beam electrons is simulated.
4. The average radiation thickness X/X_0 of the TRD supermodule.

Figure 7.13 shows three different simulated distributions of the total track length L of charged particles normalized to unity. The average radiation thickness $X/X_0 = 25.4\%$, the energy of the incident electrons $E_0 = 1$ GeV and the beam parameters are equal in

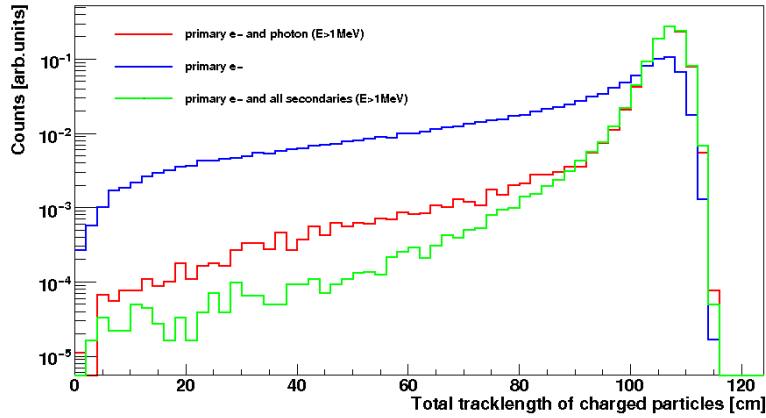


Figure 7.13: Normalized distributions of the total track length L of charged particles in the lead glass calorimeter for different settings in the simulation setup.

all three cases. The values for $\sigma_{\Theta, \Phi}$ were set to 0.05 degrees, σ_x to 2.3 cm and σ_z to 1.7 cm. The blue distribution of the total track length L of charged particles depicts the case, if the production of secondary particles within the material of the TRD is switched off. Then the showers in the lead glass block are caused by the primary electrons, which have traversed one TRD supermodule. The red distribution of the total track length L of charged particles depicts the scenario, if the generation and tracking of only secondary Bremsstrahlung photons created in the TRD supermodule above an energy of 1 MeV are included in the simulation. The green distribution depicts the case, if all secondary particles such as Bremsstrahlung photons as well as electrons and positrons above 1 MeV are generated and tracked within the TRD supermodule. In the low L -region for $L < 80$ cm the difference of the primary electron distribution (blue line) and the distribution representing the scenario when secondary particles are propagated within the the TRD (green line) is of the order of 1 to 2 orders of magnitude in the counting rate. This effect has already been predicted above while discussing Fig. 7.10, where the spectrum and the polar

angular distribution of the Bremsstrahlung photons created in the material of the TRD have been discussed qualitatively.

Another strong effect that influences the shape of the distribution of the total track length L of charged particles is caused by the variation of the initial beam parameters $\sigma_{\Theta,\Phi}$ and $\sigma_{x,z}$ as well as by the variation of the beam direction with respect to the TRD parameterized by the mean values of the angles Θ and Φ . Detailed investigations show that the most important parameters are the mean values of Θ and Φ and their according widths σ parameterized by $\sigma_{\Theta,\Phi}$. The influence of the variation of $\sigma_{x,z}$ on the distributions of the total track length L of charged particles is small as long as both values σ_x and σ_z are varied within the range of 0.7 cm to 2.4 cm given in Tab. 6.1.

According to Tab. 6.1 the values for $\sigma_{\Theta,\Phi}$ were within the range of 0.09 to 0.2 degrees during the Testbeam 2007. However, the measurement of these parameters was performed after the first trigger detector with a limited acceptance in the transversal plane, whereas the values for $\sigma_{\Theta,\Phi}$ adjustable for a simulation run as described above denote the real beam divergence in front of the first trigger detector. The highest angular deviation from the mean angular values given by $\Phi = 10$ degrees and $\Theta = 16$ degrees with respect to the TRD that an electron was allowed to have in the electron sample measured by the lead glass calorimeter was ± 0.8 degrees. If this deviation was higher, the electron did not traverse both trigger detectors and triggering on this electron did not take place. This circumstance is depicted in Fig. 7.14. Thus the shape of the distribution of the total track length

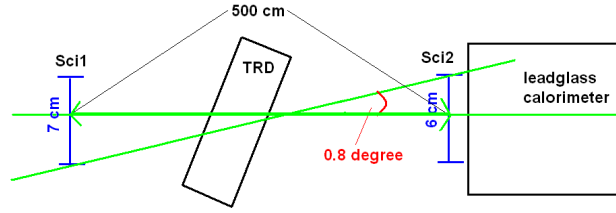


Figure 7.14: The maximum allowed angular deviation of the beam direction according to the geometrical constraints of Sci1 and Sci2 detectors.

length L of charged particles changes if $\sigma_{\Theta,\Phi}$ is varied within an interval of $[0,1]$ degrees, whereas the dependence on $\sigma_{\Theta,\Phi}$ is very small if $\sigma_{\Theta,\Phi}$ is higher than 1.0 degrees. Figure 7.15 shows the shapes of several distributions of the total track length L of charged particles for different $\sigma_{\Theta,\Phi}$ for a beam energy of $E_0 = 1$ GeV. Here, the settings for the widths $\sigma_{x,z}$ are not altered. In Fig. 7.15a the pink curve is a distribution of the total track length L of charged particles for $\sigma_{\Theta,\Phi} = 0.05$ degrees and the blue curve for $\sigma_{\Theta,\Phi} = 1.0$ degrees. For $L < 80$ cm the distribution representing the scenario with a small angular width of $\sigma_{\Theta,\Phi} = 0.05$ degrees (pink line) is suppressed by about a factor of 2 at $L = 80$ cm up to a factor of 100 at $L = 1$ cm in comparison to the distribution representing the scenario with a large angular width of $\sigma_{\Theta,\Phi} = 1.0$ degrees (blue line). Figure 7.15b shows a comparison between a distribution of the total track length L of charged particles with $\sigma_{\Theta,\Phi} = 1.0$ degrees (pink line) and a distribution of the total track length L of charged particles with $\sigma_{\Theta,\Phi} = 2.0$ degrees (blue line). Here, only a small shift of the main peak of the distribution of the total track length L of charged particles with $\sigma_{\Theta,\Phi} = 2.0$ degrees (blue line) to lower L -values in comparison to the distribution of the total track length L of charged particles with $\sigma_{\Theta,\Phi} = 1.0$ degrees (pink line) and a deviation of the order of a

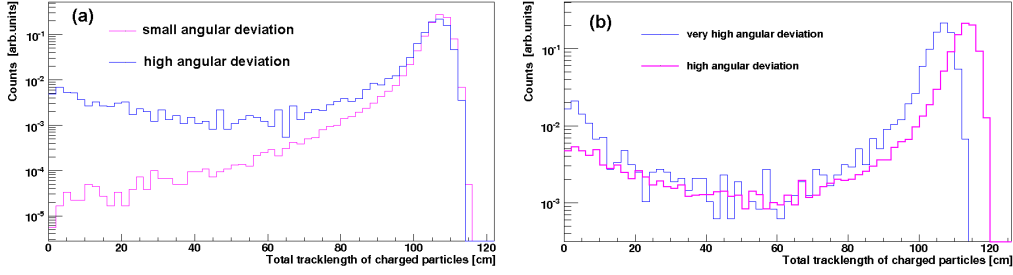


Figure 7.15: Distributions of the total track length L of charged particles for electrons at an energy of 1 GeV at (a) $\sigma_{\Theta,\Phi} = 0.05$ degrees (pink line) and $\sigma_{\Theta,\Phi} = 1.0$ degrees (blue line) as well as at (b) $\sigma_{\Theta,\Phi} = 1.0$ degrees (pink line) and $\sigma_{\Theta,\Phi} = 2.0$ degrees (blue line).

factor 2 to 5 at small L -values $L < 10$ cm is noticeable. The reason for this behavior is that if $\sigma_{\Theta,\Phi}$ is set to a high value, it is more likely that the primary electrons and their corresponding Bremsstrahlung photons hit the lead glass calorimeter not perpendicularly with respect to the front side but with a smaller angle than 90 degrees. Particles that hit the lead glass not perpendicularly cause more transversal leakage because the double Molière Radius as given in Eq. (3.4) for lead glass with $2R_m = 5.5$ cm is in the order of the transversal dimension 10×10 cm² of the lead glass calorimeter. Moreover, besides the impact angle the impact position is important. If $\sigma_{\Theta,\Phi}$ is set to a high value, it is more likely that the Bremsstrahlung photons hit the lead glass calorimeter at a significant distance from the beam center. It is not necessary that the Bremsstrahlung photons cross the trigger detector Sci2 in order to trigger on an event because the two trigger detectors are only sensitive to charged particles. Hence, the spread of the two distributions in Fig. 7.15a is due to more transversal leakage in case of the blue distribution with higher values for $\sigma_{\Theta,\Phi}$.

As shown in Fig. 7.15 the amount of transversal leakage is not further increased by incrementing $\sigma_{\Theta,\Phi}$ to values larger than 1.0 degrees because of the circumstance depicted in Fig. 7.14. If $\sigma_{\Theta,\Phi}$ is incremented to a larger value than 1.0 degrees, the only effect is that the total counting rate decreases because more electrons traverse only one of the two trigger detectors. However, the amount of transversal leakage can be further increased by changing the mean values of Φ and Θ instead of their corresponding width σ . A very

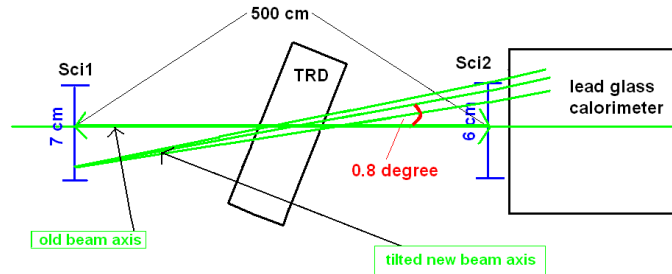


Figure 7.16: Illustration of a scenario where the amount of transversal leakage is expected to be very high. The dimensions are not to scale.

high amount of transversal leakage is expected, if Φ is set to a value of 10.8 degrees and

its corresponding value for the width σ to a considerably smaller value than 1.0 degrees, e.g. to 0.2 degrees. In this case most of the electrons traverse the distance between the two trigger detectors as depicted in Fig. 7.16 causing large lateral leakage within the lead glass calorimeter. The amount of transversal leakage is even higher if the situation for Θ is equal as for Φ , i.e. if Θ is set to 16.8 degrees and its corresponding width σ to 0.2 degrees. Figure 7.17 shows a comparison between a distribution of the total track length L of charged particles for $\Phi = 10.0$ degrees, $\Theta = 16.0$ degrees, $\sigma_{\Theta, \Phi} = 1.0$ degrees (pink

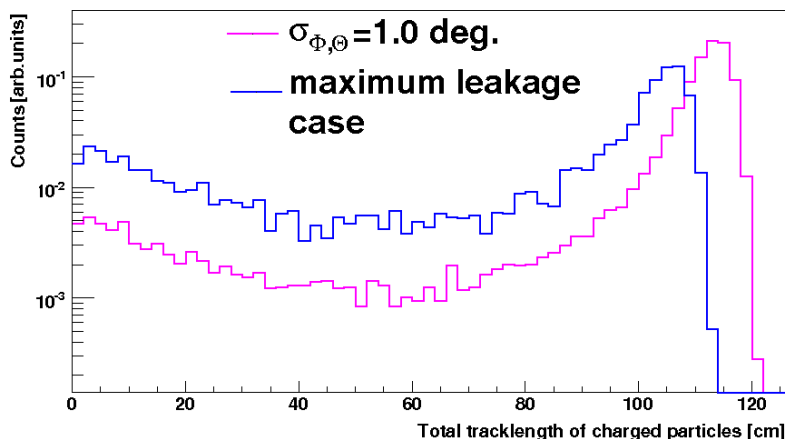


Figure 7.17: Comparison between a distribution of the total track length L of charged particles for the "maximum leakage case" (blue line, see text) and a distribution of the total track length L of charged particles (pink line) for $\Phi = 10.0$ degrees, $\Theta = 16.0$ degrees (parallel to the nominal beam direction) and $\sigma_{\Theta, \Phi} = 1.0$ degrees.

line) and a distribution of the total track length L of charged particles for the "maximum leakage case" if the situation for Φ and Θ and their according widths $\sigma_{\Theta, \Phi}$ is as described above. Besides a shift of the peak of the distribution representing the "maximum leakage case" (blue line) to lower L -values in comparison to the distribution representing the simulation run with the width $\sigma_{\Theta, \Phi} = 1.0$ degrees and the beam parallel to the nominal beam direction (pink line) an overall higher count rate of a factor of 5 to 8 of the blue distribution for $L < 90$ cm is observable.

The last effect presented in this section is the variation of the average radiation thickness X/X_0 of the TRD. The influence of this variation is depicted in Fig. 7.18 for the settings $\sigma_{\Theta, \Phi} = 0.05$ degrees and $E_0 = 1$ GeV. The increase of the radiation thickness yields a suppression factor in the order of 2 to 10 when comparing e.g. the distribution with a radiation thickness $X/X_0 = 12.5\%$ (red line) and the distribution with a radiation thickness $X/X_0 = 25\%$ (pink line).

When comparing the behavior of the distributions shown above in Fig. 7.15 and in Fig. 7.17 with the distributions depicted in Fig. 7.18 it becomes clear that the variation of the amount of lateral leakage within the lead glass calorimeter by changing the beam parameters and the variation of the average radiation thickness X/X_0 of the TRD have a comparable effect on the distributions of the total track length L of charged particles. In other words, the counting rate in the distribution of the total track length L of charged particles for $L < 90$ cm increases if the amount of lateral leakage is incremented and the

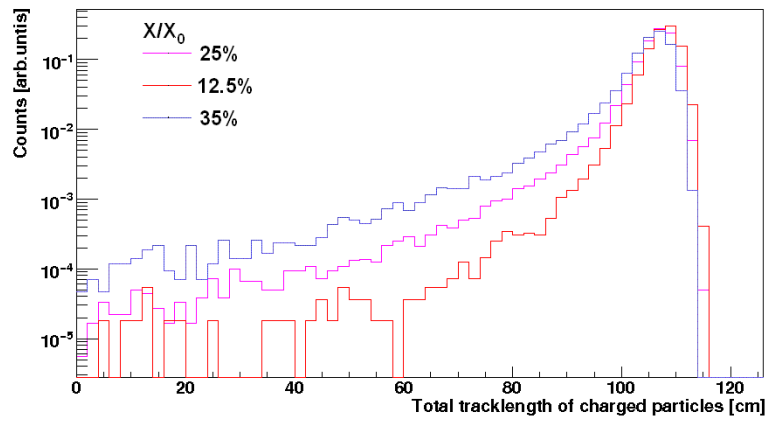


Figure 7.18: Distributions of the total track length L of charged particles for different radiation thicknesses of the TRD supermodule: $X/X_0 = 12.5\%$ (red), $X/X_0 = 25\%$ (pink), $X/X_0 = 35\%$ (blue).

same happens if the radiation thickness X/X_0 is incremented.

8 Monte Carlo - data comparison

In this chapter a comparison between experimental data described in Chap. 6 and the simulated distributions as described in Chap. 7 is given. This chapter is separated into two parts. The first part is dedicated to the comparison between the Monte-Carlo data obtained by the fast simulation and the testbeam data. The second part is dedicated to the comparison between the Monte-Carlo data obtained by the full simulation and the testbeam data. In order to get comparable distributions, the ADC values on the abscissae of the measured distributions were converted to energy values in case of the fast simulation method. The variable parametrizing the abscissa is the energy E in this case. In case of the full simulation method the values of the distributions of the total track length L of charged particles were converted to ADC values. In that case the variable parametrizing the abscissa is the lead glass amplitude in ADC. Details are given in the according sections below.

In both cases the χ^2 -test was used to estimate the goodness of the fit. The χ^2 -test is a common tool in physics, which is used to compare measured and simulated/computed distributions. The χ^2 -test provides an answer to the question whether the theory or the Monte Carlo simulation being the basis of the simulated/computed distribution is adequate when describing the data. The value, which is extracted from this comparison, is the reduced $\chi^2 = \chi_{\text{red}}^2$ given by

$$\chi_{\text{red}}^2 = \frac{1}{N-1} \cdot \sum_{i=1}^{i=N} \frac{(E_i - O_i)^2}{\sigma_i^2} \quad (8.1)$$

with E_i denoting the number of expected entries in the i -th bin provided by the simulated/computed distribution, O_i the number of observed entries in the i -th bin provided by the measured distribution, N the total number of bins and σ_i the uncertainty of the number of observed entries in the i -th bin.

According to literature [52, 53] the theory being the basis for the simulated/computed distribution is assumed to be adequate if the reduced χ^2 is **below** a threshold $\chi_{\text{red},0}^2$. This threshold depends on the number of degrees of freedom NDF which is given by $NDF = N - 1$. Tables listing this threshold as a function of number of degrees of freedom NDF are given e.g. in [54]. In Tab. 8.1 the thresholds $\chi_{\text{red},0}^2$ for several values for the number of degrees of freedom NDF are listed.

NDF	threshold $\chi_{\text{red},0}^2$
10	1.83
30	1.46
50	1.35
100	1.24

Table 8.1: The threshold $\chi_{\text{red},0}^2$ for several values for the number of degrees of freedom NDF .

8.1 Fast simulation

In order to convert the values for the amplitude in units of ADC-channels on the abscissa of the lead glass calorimeter as shown e.g. in Fig. 6.19 the ADC-to-energy calibration fit function given at the end of Chap. 6 was applied. Figure 8.1 depicts the comparison of the

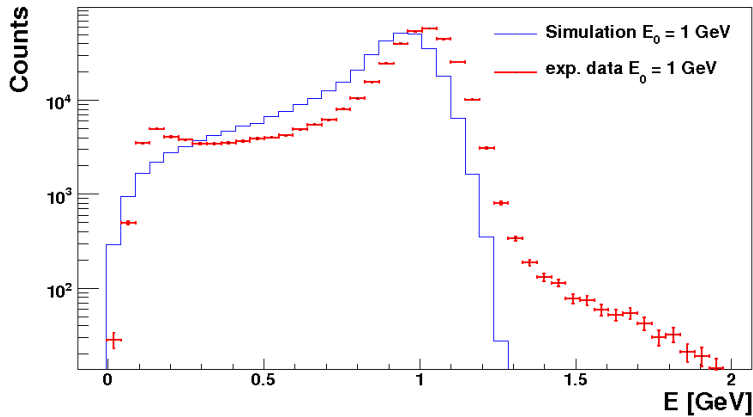


Figure 8.1: Comparison between the measured energy distribution (red line) and the simulated energy distribution (blue line) of electrons that hit the detector volume of the lead glass calorimeter.

simulated energy distribution (blue line) and the measured ADC spectrum (red line) after conversion of the ADC values to energy values at a beam energy of $E_0 = 1$ GeV. In the simulation the radiation thickness of the TRD was set to $X/X_0 = 25\%$. Four differences between the two distributions are visible.

1. The main peaks are located at different positions.
2. The low energetic part for $E < 0.8$ GeV of the simulated distribution is higher in comparison to the measured distribution.
3. There are no counts above $E = 1.3$ GeV in case of the simulated distribution in contrast to the measured distribution.
4. At low energies for $E < 0.3$ GeV the simulated distribution drops when moving to smaller energies, whereas the measured distribution rises.

The reason for the first point is that the ADC-to-energy calibration constants given at the end of Chap. 6, offset and slope, have an error and for the conversion of the ADC values to energy values of the measured distribution only one set of the two parameters was used consisting of the mean values. The second point is due to the fact that in case of the fast simulation secondary particles were not considered although secondary radiation plays an important role as shown in Fig. 7.13. The reason for the third point is that the highly energetic part of the experimental distribution is caused by contamination with events with more than one particle being either a pion or an electron in one event. In simulation the prerequisite is always one particle per event. Finally, the fourth point is due to the same reason as the second point. The fast simulation method does not reproduce the shape of

the measured distribution at energies below 0.8 GeV because many important details such as leakage within the lead glass calorimeter or secondary radiation are not considered. In order to describe the measured distribution in an energy range, where an adequate description is possible, the following procedure was performed. The ADC-to-energy calibration parameters, offset and slope, as well as the three resolution constants parameterizing the energy dependent detector resolution (see Eq. 3.8) were varied so that the reduced χ^2 of the measured and simulated histogram was minimized. The variation range for the offset and the slope was less than $\pm 10\%$ of the initial values and for the three resolution constants c_1 , c_2 and c_3 not more three times their uncertainty. This procedure was applied for different values of the radiation thickness X/X_0 for a beam energy of $E_0 = 1$ GeV and $E_0 = 2$ GeV. The fit range in case of a beam energy of $E_0 = 1$ GeV was 0.35 GeV to 1.2 GeV and in case of $E_0 = 2$ GeV the fit range was 0.5 GeV to 2.3 GeV. The flow diagram of this procedure is shown in Fig. 8.2. Figure 8.3 shows the two distributions of Fig. 8.1 after the described fit procedure. The fit range is also depicted in this figure. The

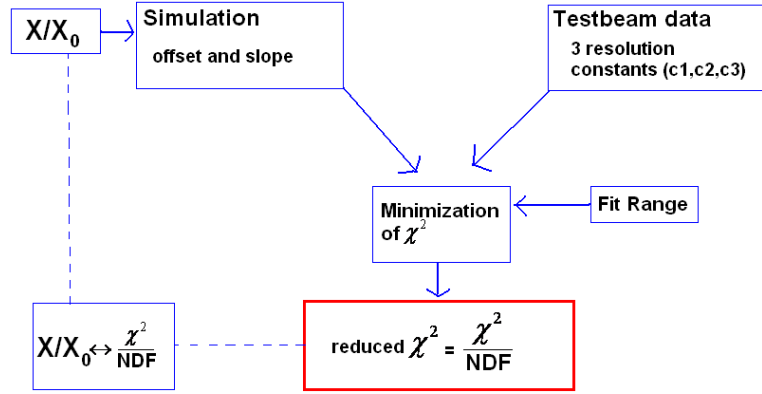


Figure 8.2: Flow diagram of the χ^2 -minimization procedure between the simulated energy distribution and the measured energy distribution of the leadglass calorimeter.

χ^2 -test of the two distributions within the fit range yields a high value for the reduced χ^2 of 10.0 due to the difference of the two distributions in the low energetic range from 0.35 GeV to 0.8 GeV. If the radiation thickness X/X_0 is decreased, the reduced χ^2 decreases because the low energetic part of the simulated distribution drops with decreasing radiation thickness X/X_0 as shown in Fig. 7.9. Figure 8.4 shows the reduced χ^2 of the χ^2 -test between the simulated and the measured energy distributions of the lead glass calorimeter for a beam energy of $E_0 = 1$ GeV (red line) and $E_0 = 2$ GeV (blue line) as a function of the average radiation thickness X/X_0 of the TRD set within the simulation. The minimum of the reduced- χ^2 -curve for an energy of 1 GeV is located at a radiation thickness X/X_0 of 20.7% and at 17.0% in case of the blue curve for an energy of 2 GeV.

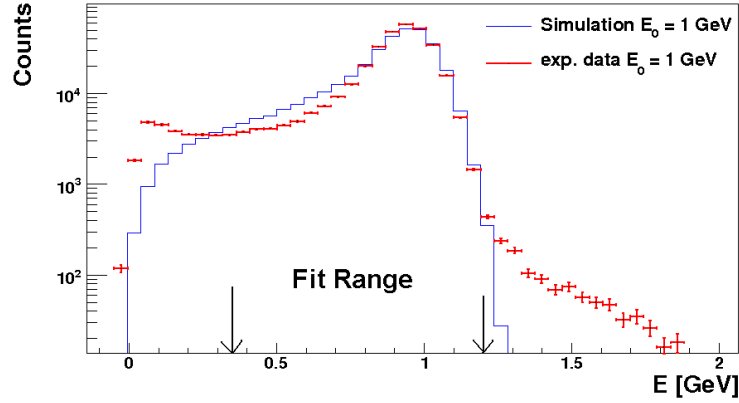


Figure 8.3: Measured (red line) and simulated (blue line) energy distribution of the lead glass calorimeter after the fit procedure. The radiation thickness X/X_0 is set to 25% in case of the simulated distribution. The arrows indicate the fit range.

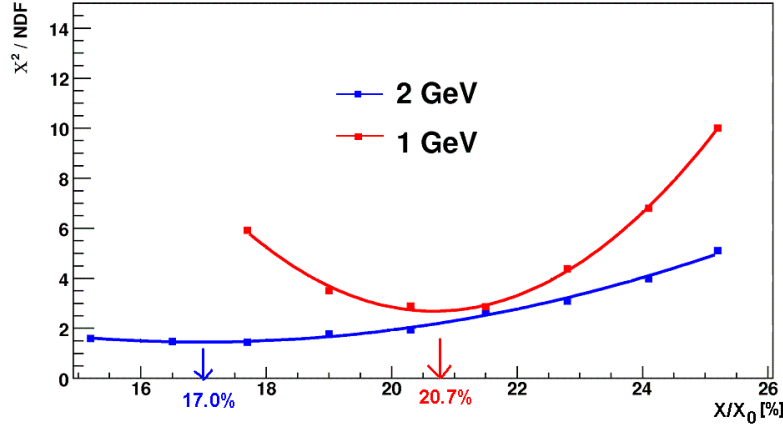


Figure 8.4: The reduced χ^2 of the χ^2 -test between the simulated and the measured energy distributions of the lead glass calorimeter for a beam energy of $E_0 = 1$ GeV (red line) and $E_0 = 2$ GeV (blue line) as a function of the average radiation thickness X/X_0 of the TRD set within the simulation. The positions of the minima of the two curves are indicated in the figure.

There are two main open issues when having a closer look at the results.

1. The simulated distributions do not reproduce the measured distributions in the total energy range.
2. The result for the radiation thickness X/X_0 is dependent on the beam energy. In contrast, the radiation length and thus also the radiation thickness are independent of the energy according to Eq. (2.10).

These issues occur because there are important details missing in the fast simulation such as production and propagation of secondary particles on the one hand and leakage within the lead glass calorimeter on the other hand. If secondary particles are considered the low energetic part of these distributions drops dramatically. This is shown in Fig. 7.13.

The reason for this suppression of the low energetic part is that the lead glass calorimeter measures the energy of the beam electrons and a large fraction of the energy of their corresponding Bremsstrahlung photons. If leakage within the leadglass calorimeter is considered the low energetic part of these distributions rises with increasing amount of lateral leakage as demonstrated in Fig. 7.15. Hence, the obtained values for the radiation thickness X/X_0 of the analysis of this section (fast simulation) shown in Fig. 8.4 are interpreted as a first rough estimation of the of the radiation thickness X/X_0 of the TRD. Moreover, this analysis was performed at a time as the contribution X/X_0^s of the silicon strip detectors to the X/X_0 experienced by the traversing electrons was considered to be negligible. As ADC spectra of runs with the silicon strip detectors in the beam line have more statistics than the runs without the silicon strip detectors, the former ones were used. However, after this analysis it was found that the contribution of the silicon strip detectors to the total X/X_0 experienced by the electrons is not negligible, but less than 5%. Therefore, the results of the rough estimation for the radiation thickness X/X_0 of the TRD are given by

- $X/X_0 = X/X_0^{1\text{GeV}} - X/X_0^s = 20.7\% - 5\% = 16\%$, for a beam energy of $E_0 = 1$ GeV.
- $X/X_0 = X/X_0^{2\text{GeV}} - X/X_0^s = 17.0\% - 5\% = 12\%$, for a beam energy of $E_0 = 2$ GeV.

8.2 Full simulation

In case of the detailed simulation the values for the track length L in units of cm on the abscissae of the distributions of the total track length L of charged particles were converted to ADC-values applying the following procedure. A L-value of 0 cm was assigned to the pedestal value (see Fig. 6.27) of 201 in units of ADC-channels of the lead glass calorimeter. The peak position of the according distribution of the total track length L of charged particles was assigned to the peak position in units of ADC-channels at the considered beam energy. These are given in Tab. 6.4. With the four values an L-to-ADC assignment could be performed using a linear formula given by

$$\text{Pb-glass Amplitude [ADC\#]} = a \cdot L[\text{cm}] + b.$$

Since the peak position in the distribution of the total track length L of charged particles moved less than 10% when the simulation settings were changed, e.g. the beam divergency $\sigma_{\Theta,\Phi}$ (see Fig. 7.15b), the values for the calibration constants a and b were varied not more than 10% of their mean values. For the comparison between the simulated ADC-distribution of the lead glass calorimeter and the measured one those parameters a and b were chosen, that yielded the smallest reduced χ^2 when performing a χ^2 -test between both distributions. The mean values for a and b were obtained by using different values for the peak position of different simulation runs having different settings for the simulation parameters such as the beam divergency $\sigma_{\Theta,\Phi}$. The reason for the circumstance that the variable on the abscissa in case of the full simulation is the amplitude of the lead glass calorimeter in units of ADC-channels and not the energy is as follows. At the beginning of the analysis of the Testbeam data and also during the development of the fast simulation the values on the abscissa of the measured ADC spectra were thought to correspond to real energies of the beam electrons. Each measured value of the amplitude of the lead

glass calorimeter was assigned to the energy of one beam electron. During the analysis and development of the full simulation it became clear that this is not the case. The values on the abscissae of the measured ADC spectra correspond to the deposit of a unknown fraction of the energy of the beam electrons and of the energy of the Bremsstrahlung photons. The main peaks of the measured ADC spectra at the different beam energies corresponds to the beam energies. They are located at values for the lead glass calorimeter amplitudes, which correspond to the full energy deposits of electrons, which have lost a small fraction of their initial energy within the TRD. Therefore, the ADC-to-energy calibration as shown at the end of Chap. 6 is correct. However, in the ADC regions left to the main peaks it makes no sense to parametrize the abscissa with the variable energy E due to the effect described above. In this case the adequate parameterization of the abscissa is performed by using the variable "amplitude of the lead glass calorimeter" in units of ADC-channels. In the following, comparisons between the measured ADC spectra of the lead glass calorimeter and the simulated distributions of the total track length L of charged particles after the above described L-to-ADC calibration are shown.

Figure 8.5 shows a comparison between three simulated distributions of the total track length L of charged particles after the above described L-to-ADC calibration (black, green and red blue line) and the measured ADC spectrum of the lead glass calorimeter at a beam energy of $E_0 = 1$ GeV (red line). The measured distribution is from a run, during which the silicon strip detectors were not in the beam line. The three simulated distributions have been already shown in Fig. 7.13. One obvious difference between the simulated

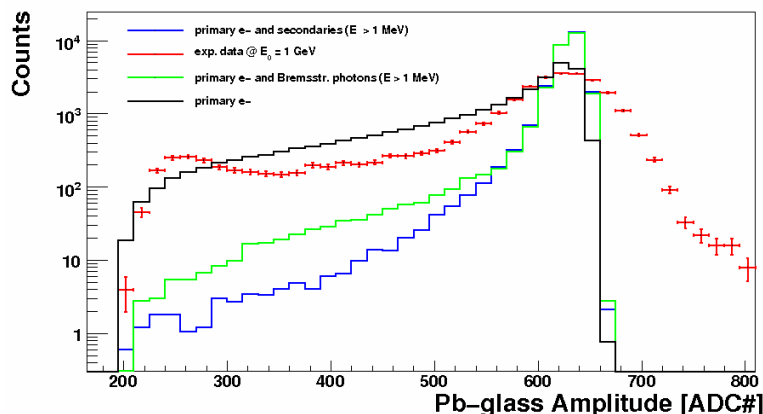


Figure 8.5: Comparison between the measured ADC spectrum of the lead glass calorimeter at beam energy of 1 GeV (red line) and the simulated distributions of the total track length L of charged particles after a L-to-ADC calibration (black, green and blue line) for different simulation settings (see legend).

distributions and the measured distribution is the different width of the main peaks. This width is different because the statistical fluctuation of the total track length L of charged particles within the lead glass calorimeter, which is responsible for the width of the main peak of the simulated distributions, is not the only source for a finite energy resolution. Further sources are described in Chap. 3. In order to include the additional fluctuations, the simulated ADC values have to be smeared along the abscissa using a Gaussian function as in case of the simulated energy values in the fast simulation method shown in Fig. 7.9. The width σ of the Gaussian function is energy dependent as shown before. This depen-

dence is given by the resolution-curve shown in Fig. 6.28. In case of the simulated ADC spectra in Fig. 8.5 this resolution-curve can not be applied because the peaks of these simulated spectra have already a width in the order of a 8 ADC-channels. This width is due to the statistical fluctuation of the total track length L of charged particles within the lead glass calorimeter. However, all contributions including the statistical fluctuation of the total track length L of charged particles to the finite energy resolution of the lead glass calorimeter are included in the resolution-curve. If this curve was used for the smearing of the ADC-values as described above, the contribution of the statistical fluctuation of the total track length L of charged particles would contribute twice to the total width of the main peak. This problem was circumvented by decreasing the calibration constant c_1 of the resolution-curve by 10% to 20% of its nominal value. The contribution of the statistical fluctuation of the total track length L of charged particles is proportional to $\sqrt{\frac{1}{E}}$. Therefore the constant c_1 is the adequate constant to be decreased in order to exclude the contribution of the statistical fluctuation of the total track L length of charged particles. Next, the resolution-curve with the decreased calibration constant c_1 was used for the smearing of the ADC-values of the spectra shown in Fig. 8.5 according to a Gauss function. The assignment of energy E being the variable in the resolution-curve to the lead glass amplitude in units of ADC-channels being the variable on the abscissa in all histograms showed in this section was possible at any time by using the ADC-to-energy calibration shown in Fig. 6.27.

For comparison between the measured and simulated ADC-spectrum of the lead glass calorimeter the value for c_1 with the smallest reduced χ^2 was chosen. Figure 8.6 shows a comparison between the measured ADC spectrum of the lead glass calorimeter at a

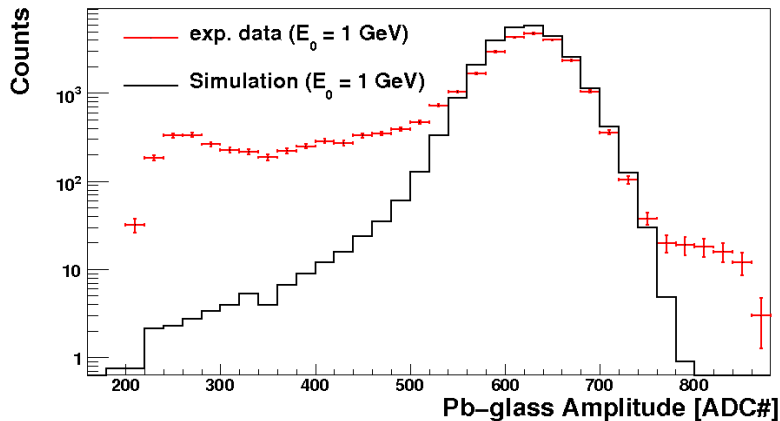


Figure 8.6: Comparison between a measured ADC spectrum at $E_0 = 1$ GeV (red line) and an according simulated ADC spectrum for a beam divergency of $\sigma_{\Theta, \Phi}$ of 0.05 degrees and a radiation thickness of the TRD of 25% (black line).

beam energy of $E_0 = 1$ GeV and an distribution of the total track length L of charged particles after an L-to-ADC calibration and after the procedure described above with simulation parameters representing the "low leakage case". The "low leakage case" is the simulation scenario which ensures that the amount of transversal leakage within the lead glass calorimeter is low. In case of the simulated distribution in Figure 8.6 the radiation thickness X/X_0 is set to 25%. The other simulation parameters are specified in Tab. 8.2.

The generation and tracking of secondary particles within the material of the TRD is

Figure	X/X_0 [%]	E_0 [GeV]	Φ [deg.]	σ_Φ [deg.]	Θ [deg.]	σ_Θ [deg.]	χ^2/NDF
8.6	25	1.0	10.0	± 0.05	16.0	± 0.05	> 10.0
8.7	50	1.0	10.0	± 0.05	16.0	± 0.05	> 10.0
8.8	50	1.0	10.0	± 0.40	16.0	± 0.40	> 10.0
8.8	65	1.0	10.0	± 0.40	16.0	± 0.40	7.0

Table 8.2: Overview of the simulation parameters for several comparisons between the measured ADC spectrum of the lead glass calorimeter and the simulated ADC distributions for the "low leakage case" ensuring that the amount of lateral leakage within the lead glass calorimeter is low. "Figure" denotes the figure number, where the comparison is displayed, X/X_0 the radiation thickness of the TRD set within the simulation, E_0 the beam energy, Φ and Θ the values for the two angles parameterizing the direction of the beam set within the simulation, σ_Φ and σ_Θ the widths of the two angles set within the simulation and χ^2/NDF the reduced χ^2 obtained by comparing the simulated and measured distribution. The beam direction is equal to the nominal beam direction if Θ is set to 16.0 degrees and Φ to 10.0 degrees.

switched on for this and for all following comparisons. The simulated spectrum does not reproduce the measured spectrum in the low ADC region. This part of the spectrum is most important because it is sensitive to the radiation thickness X/X_0 of the TRD. The high ADC region is not shown here because the difference between the simulated and the measured spectrum in this region is caused by more than one particle in one event and is not sensitive to changes in the radiation thickness X/X_0 of the TRD.

If all simulation parameters such as $\sigma_{\Theta,\Phi}$ or the beam energy are not altered except the radiation thickness X/X_0 , which is doubled, the counting rate in the low ADC region of the simulated ADC spectrum rises. In Fig. 8.7 a simulated spectrum for a radiation thickness X/X_0 of 50% and the according measured ADC spectrum are shown (red line).

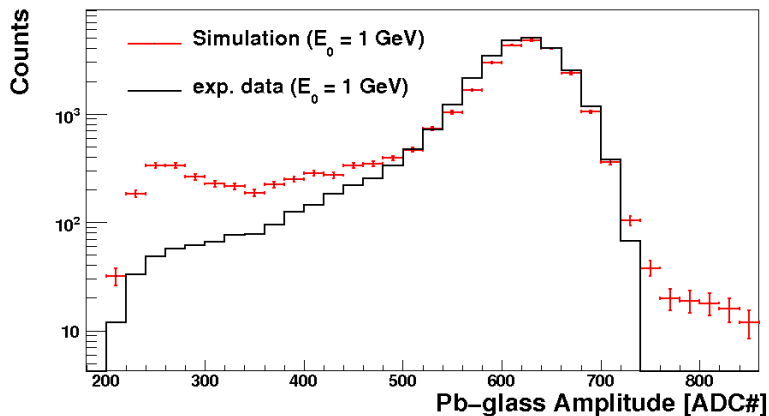


Figure 8.7: Comparison between a measured ADC spectrum ($E = 1$ GeV) of electrons (black) and an according simulated ADC spectrum for a $\sigma_{\Theta,\Phi}$ of 0.05 degrees and a radiation thickness of the TRD of 50%.

This value for the radiation thickness X/X_0 is twice the estimated value of 25% according to the technical design estimations as given in Chap. 5. Even in that extreme case the experimental data is underestimated by up to a factor of 5 at ADC values below channel 350. Moreover, the simulated ADC distribution does not reproduce the shape of the measured

distribution qualitatively. Below ADC-channel 350 the measured ADC distributions rises resulting in a peak at an ADC-channel around 250, whereas the simulated ADC spectrum decreases continuously as a function of the lead glass calorimeter amplitude when moving from ADC-channel 600 to 200.

The counting rate below ADC-channel 600 increases if the value for the beam divergency $\sigma_{\Theta,\Phi}$ is enhanced. Figure 8.8 shows a comparison between the measured ADC spectrum of the lead glass calorimeter (red line) and three different simulated ADC spectra at a beam

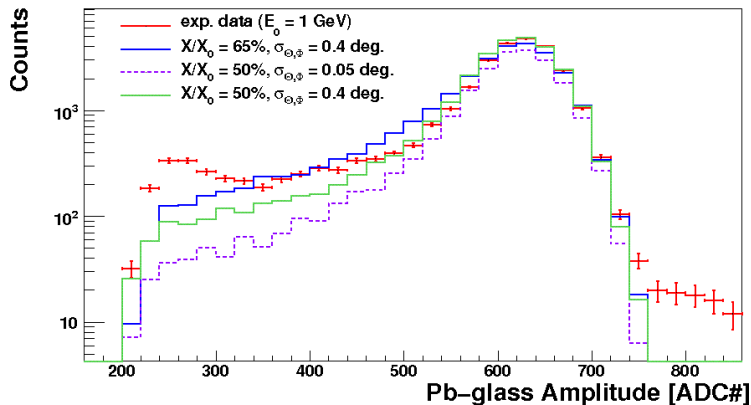


Figure 8.8: Comparison between the measured ADC spectrum at a beam energy of $E = 1$ GeV for electrons (red line) and three simulated ADC spectra at a X/X_0 of 50% (green line), 65% (blue line) and 50% (purple, dashed line). $\sigma_{\Theta,\Phi}$ is set to 0.4 degrees in case of the distributions drawn in with solid lines and 0.05 degrees in case of the distribution drawn in with a dashed line.

energy of $E_0 = 1$ GeV. There are two distributions with a radiation thickness X/X_0 of 50% (purple dashed and green solid line) and one distribution with a radiation thickness X/X_0 of 65% (blue line). An overview of the other simulation parameters is given in Tab. 8.2. The difference between the two simulated distributions at a radiation thickness of 50% (purple dashed and green solid line) is the setting for the width $\sigma_{\Theta,\Phi}$. In case of the purple dashed distribution $\sigma_{\Theta,\Phi}$ was set to 0.05 degrees and in case of the green distribution $\sigma_{\Theta,\Phi}$ was set to 0.4 degrees. A clear increase of the counting rate for ADC values below channel 600 is noticeable when comparing both simulated distributions. Additionally, a distribution for a beam divergency of $\sigma_{\Theta,\Phi}$ of 0.4 degrees and a radiation thickness X/X_0 of 65% is drawn in (blue line). The lowest reduced χ^2 is obtained when comparing this distribution and the measured data. The χ^2 -test yields a value of 7.0 in this case. This value is rather high because the shape of the measured distribution is not reproduced as in case of $\sigma_{\Theta,\Phi} = 0.05$ degrees as described above. This shape is reproducible if $\sigma_{\Theta,\Phi}$ is set to a high value of 1.0 degrees and thus further increasing the amount of transversal leakage in the lead glass calorimeter. Figure 8.9 shows a comparison between the measured ADC spectrum of the lead glass calorimeter at a beam energy of $E_0 = 1$ GeV and four simulated ADC spectra with four different values for the radiation thickness X/X_0 of the TRD and a beam divergency of $\sigma_{\Theta,\Phi}$ of 1.0 degrees. The beam direction is still parallel to the nominal beam direction. This case represents the scenario "medium leakage case". An overview of the simulation parameters is given in Tab. 8.3.

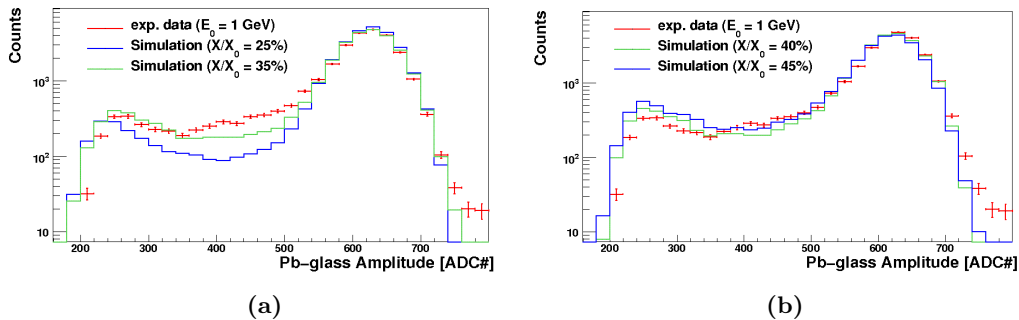


Figure 8.9: (a) Comparison between the measured ADC spectrum at a beam energy of $E_0 = 1$ GeV of the lead glass calorimeter (red line) with two simulated ADC spectra at a radiation thickness X/X_0 of 25% (blue line) and 35% (green line). (b) Comparison between the measured ADC spectrum at a beam energy of $E_0 = 1$ GeV of the lead glass calorimeter (red line) with two simulated ADC spectra at a radiation thickness X/X_0 of 45% (blue line) and 40% (green line). The beam divergency $\sigma_{\Theta, \Phi}$ is set to 1.0 degrees in case of all simulated ADC spectra.

Figure	X/X_0 [%]	E_0 [GeV]	Φ [deg.]	σ_{Φ} [deg.]	Θ [deg.]	σ_{Θ} [deg.]	χ^2/NDF
8.9a	25	1.0	10.0	± 1.0	16.0	± 1.0	> 10.0
8.9a	35	1.0	10.0	± 1.0	16.0	± 1.0	2.3
8.9b	40	1.0	10.0	± 1.0	16.0	± 1.0	2.0
8.9b	45	1.0	10.0	± 1.0	16.0	± 1.0	3.5
8.11a	25	2.0	10.0	± 1.0	16.0	± 1.0	5.1
8.11b	35	2.0	10.0	± 1.0	16.0	± 1.0	1.9
8.11a	40	2.0	10.0	± 1.0	16.0	± 1.0	1.1
8.11b	45	2.0	10.0	± 1.0	16.0	± 1.0	1.5

Table 8.3: Overview of the simulation parameters for several comparisons between the measured ADC spectrum of the lead glass calorimeter and the simulated ADC distributions for the "medium leakage case" ensuring that the amount of lateral leakage within the lead glass calorimeter is medium. "Figure" denotes the figure number, where the comparison is displayed, X/X_0 the radiation thickness of the TRD set within the simulation, E_0 the beam energy, Φ and Θ the values for the two angles parameterizing the direction of the beam set within the simulation, σ_{Φ} and σ_{Θ} the widths of the two angles set within the simulation and χ^2/NDF the reduced χ^2 obtained by comparing the simulated and measured distribution. The beam direction is equal to the nominal beam direction if Θ is set to 16.0 degrees and Φ to 10.0 degrees.

The measured ADC distribution is reproduced best by the simulated ADC distribution at a radiation thickness X/X_0 of 40%. The χ^2 -test yields a value of $\chi^2/NDF = 2.0$ in an abscissa range from ADC-channel 100 to ADC-channel 750 in this case. The value for the reduced χ^2 is still high because the counting rate is too high below an ADC-channel 280. The qualitative shape is reproduced by these simulated distributions with a beam divergency $\sigma_{\Theta, \Phi} = 1.0$ degrees except for the ratio between the counting rate in the very low ADC-channel region ranging from channel 180 to 280 and the medium ADC region ranging from channel 280 to 550. This ratio is different in comparison to the measured distribution. This systematic deviation occurs also in all comparisons at a beam energy of $E_0 = 1$ GeV shown below for altered beam parameters such as the beam divergency $\sigma_{\Theta, \Phi}$ or the angle values Φ and Θ . The reason for this deviation is not yet fully understood.

The amount of transversal leakage, which increases the counting rate in the medium and low ADC range of the simulated spectra, is not maximal even if $\sigma_{\Theta, \Phi}$ is set to 1.0 degrees in the simulation. The largest transversal leakage occurs if the values for Φ and Θ are increased by 0.8 degrees. This scenario is depicted in Fig. 7.16. Figure 8.10 shows the comparison between the measured ADC spectrum for a beam energy of $E_0 = 1$ GeV (red line) and three different simulated ADC distributions at various radiation thicknesses

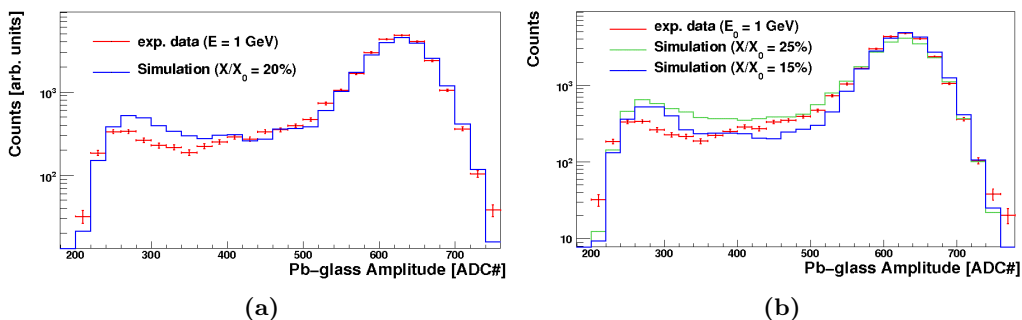


Figure 8.10: (a) Comparison between the measured ADC spectrum at a beam energy of $E_0 = 1$ GeV of the lead glass calorimeter (red line) and a simulated ADC spectrum at a radiation thickness X/X_0 of 20% (blue line) and values for the angle Θ of 16.8 degrees and 10.8 degrees for Φ . (b) Comparison between the measured ADC spectrum at a beam energy of $E_0 = 1$ GeV of electrons (red line) with two simulated ADC spectra at a radiation thickness X/X_0 of 15% (blue line) and 25% (green line) and values for the angle Θ of 16.8 degrees and 10.8 degrees for Φ . The value for $\sigma_{\Theta, \Phi}$ is set to 0.2 degrees in case of all simulated ADC spectra.

X/X_0 of the TRD. The values for the two angles Θ and Φ as well as for $\sigma_{\Theta, \Phi}$ are the same as in case of the "maximum leakage case" shown in Fig. 7.16. An overview of the simulation parameters is shown in Tab. 8.4. The lowest reduced χ^2 is obtained when the

Figure	X/X_0 [%]	E_0 [GeV]	Φ [deg.]	σ_{Φ} [deg.]	Θ [deg.]	σ_{Θ} [deg.]	χ^2/NDF
8.10b	15	1.0	10.8	± 0.2	16.8	± 0.2	1.7
8.10a	20	1.0	10.8	± 0.2	16.8	± 0.2	1.6
8.10b	25	1.0	10.8	± 0.2	16.8	± 0.2	3.6
8.12	10	2.0	10.8	± 0.2	16.8	± 0.2	1.8
n.s.	20	2.0	10.8	± 0.2	16.8	± 0.2	2.9
n.s.	25	2.0	10.8	± 0.2	16.8	± 0.2	4.9

Table 8.4: Overview of the simulation parameters for several comparisons between the measured ADC spectrum of the lead glass calorimeter and the simulated ADC distributions for the "maximum leakage case" ensuring that the amount of lateral leakage within the lead glass calorimeter is maximal. "Figure" denotes the figure number displaying the comparison, "n.s." that the comparison is not shown, X/X_0 the radiation thickness of the TRD set within the simulation, E_0 the beam energy, Φ and Θ the values for the two angles parametrizing the direction of the beam set within the simulation, σ_{Φ} and σ_{Θ} the widths of the two angles set within the simulation and χ^2/NDF the reduced χ^2 obtained by comparing the simulated and measured distribution. The beam direction is equal to the nominal beam direction if Θ is set to 16.0 degrees and Φ to 10.0 degrees.

radiation thickness X/X_0 is set to 20%. The χ^2 -test yields a value of 1.6 in this case. As in case of Fig. 8.9 the ratio between the counting rate in the very low ADC region ranging

from channel 180 to 280 and the medium ADC region ranging from channel 280 to 550 is too high in comparison to the measured distribution due to an unknown effect.

The amount of transversal leakage within the lead glass calorimeter softly lowers if the value for Θ is decreased from 16.8 (scenario "maximum leakage case") to 16.5, respectively from 10.8 to 10.5 for Φ . This case represents the "high leakage case". The amount of transversal leakage is high in this case. In this case the simulated distributions look similar to those shown in Fig. 8.10 unless the best accordance between measured data and simulation is achieved at a radiation thickness X/X_0 of 30%. The χ^2 -test yields a value of $\chi^2/NDF = 1.9$ in this case. An overview of the simulation parameters and the obtained reduced χ^2 is given in Tab. 8.5.

Figure	X/X_0 [%]	E_0 [GeV]	Φ [deg.]	σ_Φ [deg.]	Θ [deg.]	σ_Θ [deg.]	χ^2/NDF
n.s.	25	1.0	10.5	± 0.2	16.5	± 0.2	3.9
n.s.	30	1.0	10.5	± 0.2	16.5	± 0.2	1.9
n.s.	35	1.0	10.5	± 0.2	16.5	± 0.2	3.5

Table 8.5: Overview of the simulation parameters for several comparisons between the measured ADC spectrum of the lead glass calorimeter and the simulated ADC distributions for the "high leakage case" ensuring that the amount of lateral leakage within the lead glass calorimeter is high. "Figure" denotes the figure number displaying the comparison, "n.s." that the comparison is not shown, X/X_0 the radiation thickness of the TRD set within the simulation, E_0 the beam energy, Φ and Θ the values for the two angles parametrizing the direction of the beam set within the simulation, σ_Φ and σ_Θ the widths of the two angles set within the simulation and χ^2/NDF the reduced χ^2 obtained by comparing the simulated and measured distribution. The beam direction is equal to the nominal beam direction if Θ is set to 16.0 degrees and Φ to 10.0 degrees.

In order to perform a cross check at a beam energy of 2 GeV, the same analysis was performed for two sets of simulation parameters specified above, namely for for the "maximum leakage case" (see Tab. 8.4) and for the "medium leakage case" (see Tab. 8.3). In case of a beam energy of $E_0 = 2$ GeV the ADC spectrum measured by the lead glass calorimeter only ranges down to ADC-channel 550 (see Fig. 6.24) because there is no data available without the silicon strip detectors in the beam line and without the lead glass calorimeter involved in the trigger decision. In order to be able to fully trust the results of such a complicated quantitative study as described above for a beam energy of $E_0 = 1$ GeV, it is essential that the full ADC spectrum down to the pedestal ADC-channel 200 of the lead glass calorimeter is available. Since this is not the case for a beam energy of $E_0 = 2$ GeV, the check at this energy described below was performed in order to investigate if the results at the two beam energies are consistent and not to find precise values for the upper and lower limit of the radiation thickness X/X_0 for a beam energy of $E_0 = 2$ GeV. These values are extractable from the analysis of the data at a beam energy of $E_0 = 1$ GeV and they are given at the end of this chapter. In the following, the two representative cases for the simulation settings at a beam energy of 2 GeV are described.

Figure 8.11 shows a comparison between the ADC spectrum of electrons measured by the lead glass calorimeter at a beam energy of $E_0 = 2$ GeV (red line) and four simulated ADC spectra for four different radiation thicknesses X/X_0 and the parameter setting as for the "medium leakage case". The simulation parameters are specified in Tab. 8.3. The data is reproduced best at a radiation thickness X/X_0 of 40% as in case of a beam energy of $E_0 = 1$ GeV as shown in Fig. 8.9.

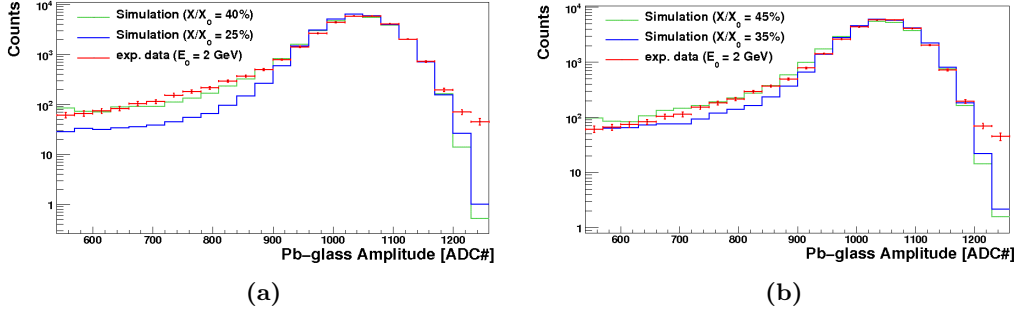


Figure 8.11: (a) Comparison between the measured ADC spectrum at a beam energy of $E = 2$ GeV of electrons (red line) with two simulated ADC spectra at a X/X_0 of 25% (blue line) and 40% (green line). (b) Comparison between the measured ADC spectrum at a beam energy of $E = 2$ GeV of electrons (red line) with two simulated ADC spectra at a X/X_0 of 35% (blue line) and 45% (green line). The value for $\sigma_{\Theta, \Phi}$ is set to 1.0 degrees, to 16.0 degrees for Θ and to 10.0 degrees for Φ in case of all simulated ADC spectra.

The second analysis for a beam energy of $E_0 = 2$ GeV was performed for the "maximum leakage case" as discussed in Fig. 8.10 for 1 GeV. The simulation parameters are specified in Tab. 8.4. Here the simulated ADC distribution of electrons does not reproduce the measured data even if the radiation thickness X/X_0 is set to a small value of 10%. The counting rate in the ADC region below 1000 is still too high up to factor 2.5 in case of the simulated distribution. This situation is depicted in Fig. 8.12. In this figure a comparison between the measured ADC spectrum of the lead glass calorimeter (red line) at a beam

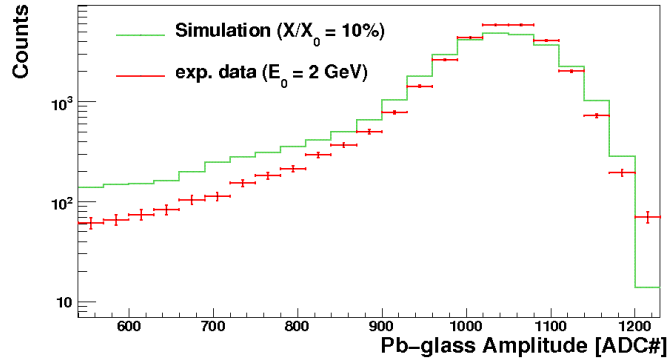


Figure 8.12: Comparison between the measured ADC spectrum at a beam energy of $E = 2$ GeV of electrons (red line) with a simulated ADC spectrum at a X/X_0 of 10% (green line). The value for Θ is 16.8 degrees, respectively 10.8 degrees for Φ , and the value for $\sigma_{\Theta, \Phi}$ is set to 0.2 degrees in case of the simulated distribution (green line). This settings represent the "maximum leakage case".

energy of $E_0 = 2$ GeV and the simulated ADC spectrum for a radiation thickness X/X_0 of 10% (green line) and for simulation settings as given for the "maximum leakage case" described above is shown. Hence, if the simulation settings are given as in the "maximum leakage case", the amount of transversal leakage within the lead glass calorimeter is overestimated for a beam energy of $E_0 = 2$ GeV.

Summary

In order to extract the radiation thickness X/X_0 of the TRD for each set of simulation parameters, the reduced χ^2 obtained for every case by comparing the measured ADC spectrum of the lead glass calorimeter and the simulated spectrum was plotted as a function of the radiation thickness X/X_0 . A parabola was fitted to the resulting data points. Next, the position of the minimum on the abscissa of the curve was determined. Figure 8.13

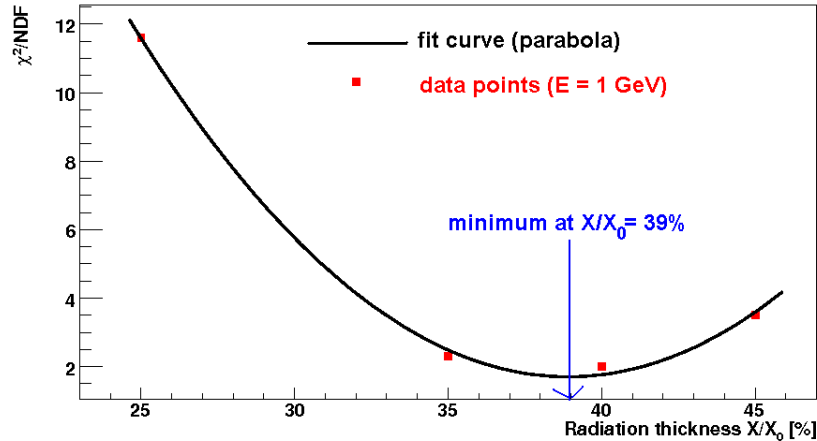


Figure 8.13: The reduced χ^2 as a function of the radiation thickness X/X_0 set within the simulation for a beam energy of 1 GeV and simulation parameters as for the "medium leakage case" (see Tab. 8.3). The black curve depicts the fit to the four data points. The minimum of the fit curve is located at a radiation thickness of 39%.

shows the reduced χ^2 as a function of the radiation thickness X/X_0 for a beam energy of $E_0 = 1$ GeV and simulation settings as for the "medium leakage case" (see Tab. 8.3). The minimum of the fit function shown in Fig. 8.13 is located at a X/X_0 of 39%. In the following, a list of the obtained values for the radiation thickness X/X_0 for different sets of simulation parameters applying the procedure described above is given. The list begins with simulation parameters, which assured that the amount of transversal leakage within the lead glass calorimeter was low and then continues with increasing amount of transversal leakage.

1. Low leakage (see Tab. 8.2)

Beam energy $E_0 = 1$ GeV. A value for the radiation thickness X/X_0 was not extractable applying the procedure described above because the simulated ADC spectrum does not reproduce the shape of the measured one. The lowest reduced χ^2 is given by an unacceptable value of 7.0 at a X/X_0 of 65%. A X/X_0 of 65% is more than twice the estimated value for the radiation thickness given in Chap. 5.

2. Medium leakage (see Tab. 8.3)

- Beam energy $E_0 = 1$ GeV. The radiation thickness was extractable in this case and amounts to $X/X_0 = 39\%$.
- Beam energy $E_0 = 2$ GeV. The radiation thickness was extractable in this case and amounts to $X/X_0 = 41\%$.

3. High leakage (see Tab. 8.5)

- Beam energy $E_0 = 1$ GeV. The radiation thickness was extractable in this case and amounts to $X/X_0 = 30\%$.

4. Maximum leakage (see Tab. 8.4)

- Beam energy $E_0 = 1$ GeV. The radiation thickness was extractable in this case and amounts to $X/X_0 = 18\%$.
- Beam energy $E_0 = 2$ GeV. A value for the radiation thickness X/X_0 was not extractable applying the procedure described above because the counting rate of the simulated ADC spectrum in the low ADC region is too high even for $X/X_0 = 10\%$ as shown in Fig. 8.12. A value of $X/X_0 = 10\%$ is less than half the estimated value for the radiation thickness given in Chap. 5.

The results listed above are shown graphically in Fig. 8.14, where the measured average radiation thickness X/X_0 as a function of the amount of lateral leakage is shown.

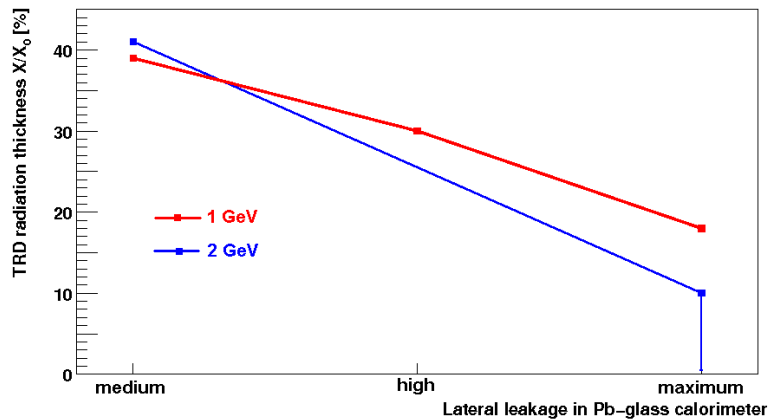


Figure 8.14: Measured average radiation thickness X/X_0 as a function of the amount of lateral leakage within the lead glass calorimeter for a beam energy of $E_0 = 1$ GeV (red line) and $E_0 = 2$ GeV (blue line). The large error bar for the second data point for $E_0 = 2$ GeV indicates that the value for the radiation thickness is between $X/X_0 = 0\%$ and $X/X_0 = 10\%$, for details see text above.

The abscissa of the diagram displays the amount of lateral leakage within the lead glass calorimeter in arbitrary units. There are three cases: medium, high and maximum. The corresponding simulation settings for the three scenarios are given in Tabs. 8.2, 8.3, 8.5, 8.4. The ordinate displays the radiation thickness X/X_0 of the TRD in units of per cent.

9 Summary and Outlook

Within this thesis an analysis of data taken during the TRD Testbeam 2007 at CERN was performed. The testbeam setup consisted of one TRD supermodule, two trigger detectors, two silicon strip detectors, a Cherenkov detector and an electromagnetic lead glass calorimeter placed in a beam line of an electron/pion beam. Electron events were separated from pion events using the particle identification capability of the Cherenkov detector. The ADC distributions of electrons measured by the lead glass calorimeter were investigated. In order to estimate the radiation thickness X/X_0 of the TRD these distributions were reproduced applying Monte Carlo simulations. Two different methods were developed in order to reproduce the signal of the lead glass calorimeter. The first one, a rather primitive simulation with poor accuracy, provided first rough estimations of the radiation thickness $X/X_0 = 12\%$ at a beam energy of $E_0 = 1$ GeV and $X/X_0 = 16\%$ at a beam energy of $E_0 = 2$ GeV. The second method was more detailed revealing the inaccuracy of the first one, in which a very important detail was not included - the generation and tracking of secondary particles within the material of the TRD and within the active volume of the lead glass calorimeter. It turned out that the signal of the lead glass calorimeter is sensitive to the introduced beam parameters such as the beam angles Θ , Φ or the beam divergency parametrized by the widths $\sigma_{\Theta, \Phi}$. The measured ADC-distributions are sensitive to the radiation thickness X/X_0 and the beam parameters in the same ADC range, which made the measurement of the X/X_0 inaccurate. The reason for this behavior is the fact, that the lead glass calorimeter did not measure the energy of the beam electron during one triggered event but always the energy of the beam electron and an unknown fraction of the energy of its according Bremsstrahlung photons created within the material of the TRD. This fraction depended crucially on the beam parameters mentioned above. The number of Bremsstrahlung photons, which disappeared within the material of the TRD due to pair conversion was low, and even the created electron-positron pairs due to the impact of the Bremsstrahlung photons contributed to the measured signal of the lead glass calorimeter. Therefore, the measured ADC-distribution of the lead glass calorimeter in the low ADC range was mainly driven by the impact position parameter distribution of the incident leptons and photons and not by the energy distribution of the primary beam electrons after traversing the material of the TRD. If most of the incident leptons and photons hit the lead glass calorimeter during one triggered event rather at the edges of its transversal acceptance, the resulting ADC value was low. If most of the incident particles hit the lead glass rather centrally, the ADC value was high.

Because of the described effects only the upper and lower limits within a large range of the radiation thickness X/X_0 of the TRD were extracted in the analysis. In case of a beam energy of $E_0 = 1$ GeV the upper limit is given by $X/X_0^{up} = 39\%$ extracted from a simulation run, during in the amount of transversal leakage within the lead glass calorimeter was medium. The lower limit is given by $X/X_0^{low} = 18\%$ using a simulation run, in which the amount of transversal leakage was high. A similar analysis of a run with

a beam energy of $E_0 = 2$ GeV used as cross check to the analysis at a beam energy of $E_0 = 1$ GeV revealed that the upper limit is given by $X/X_0^{up} = 41\%$. The lower limit was not extractable by applying the full simulation method for this beam energy. The results are visualized in Fig. 9.1. They are consistent with estimated radiation thickness X/X_0 based on technical design estimations.

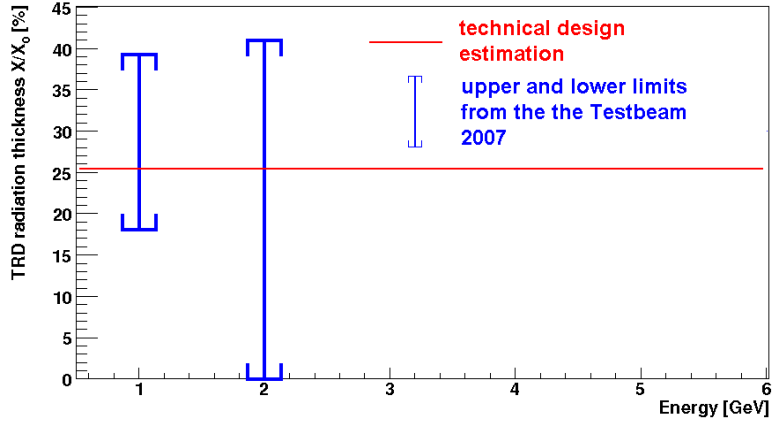


Figure 9.1: Estimations of the radiation thickness X/X_0 of the TRD as a function of beam energy based on technical design estimations (red line) and based on the analysis of the TRD Testbeam 2007 (blue error bars).

Outlook

The experimental setup of the Testbeam 2007 allowed only a determination of the lower and upper limit of the radiation thickness of the TRD. A proposal for an experimental setup that allows a precise measurement of the TRD radiation thickness X/X_0 in the future is described in the following. In order to separate the Bremsstrahlung photons from the primary beam electrons and prevent them from hitting the lead glass calorimeter the experimental setup as shown in Fig. 6.2 has to be modified. A magnetic dipole field **after** the TRD should be installed. The proposed experimental setup is shown in Fig 9.2.

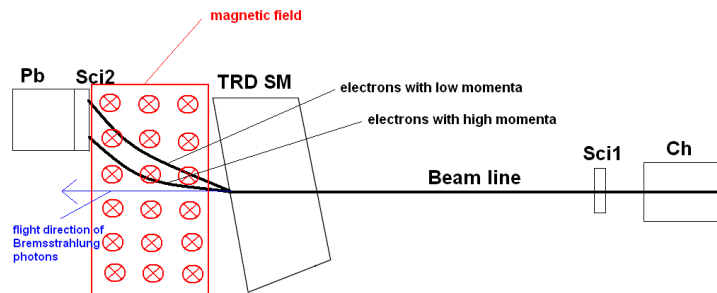


Figure 9.2: Proposal for an experimental setup that allows a precise measurement of the TRD radiation thickness X/X_0 . Pb: Lead glass calorimeter; Sci1,Sci2: Scintillation trigger detectors; TRD SM: One supermodule of the TRD; Ch: Cherenkov detector.

Electrons with high momenta are less deflected than electrons with low momenta in the magnetic field. Further, it must be ensured that the dimensions of the lead glass calorimeter shown in Fig. 9.2 are sufficient so that the amount of transversal and lateral leakage is kept as low as possible. Moreover, a silicon strip detector with a known radiation thickness X/X_0 could be installed directly in front the lead glass calorimeter in order to select electrons, which hit the lead glass calorimeter centrally. This would introduce a bias on the electron sample. However, this could be studied precisely with the Monte Carlo simulations developed in this thesis.

Bibliography

- [1] L Yan, P. Zhuang and N. Xu, Phys. Rev. Lett. **97** (2006) 232301.
- [2] M. Djordjevic and M. Gyulassy, Acta. Phys. Hung. **A24** (2005).
- [3] B. Zhang, L.W. Chen and C-M. Ko, Phys. Rev. **C72** (2005).
- [4] P. Braun-Munzinger and J. Stachel, Nucl. Phys. **A690** (2001) 119c.
- [5] A. Andronic et al., Phys. Lett. **B571** (2003) 36.
- [6] H. Satz and T. Matsui, Phys. Lett. **B178** (1986) 416.
- [7] P. Braun-Munzinger and J. Stachel, Phys. Lett. **B490** (2000) 196.
- [8] R.L. Thews, M. Schroedter and J. Rafelski, Phys. Rev. **C63** (2001) 054905.
- [9] L. Grandchamp et al., Phys. Rev. **C73** (2006) 064906.
- [10] B. Zhang, Phys. Lett. **B647** (2007) 249.
- [11] V. Greco, C.M. Ko, R. Rapp, Phys. Lett. **B595** (2004) 202.
- [12] Z.W. Lin and D. Molnar, Phys. Rev. **C68** (2003) 044901.
- [13] A. Adare *et al.*, Phys. Rev. Lett. **98** (2007) 232301.
- [14] A. Andronic *et al.*, Phys. Lett. **B652** (2007) 259.
- [15] K. Kleinknecht, "Detektoren für Teilchenstrahlung", Teubner-Verlag, Mainz (2005).
- [16] C. Amsler *et al.*, Phys. Lett. **B667**, (2008) 1.
- [17] G. Musiol, J. Ranft, R. Reif, D. Seeliger, "Kern- und Elementarteilchenphysik", VCH Verlagsgesellschaft, Weinheim (1988).
- [18] W. Heitler, "The Quantum Theory of Radiation", Clarendon Pr. , Oxford (1954).
- [19] K.H. Meier, private communication, "Physics of Particle Detectors", lecture, University of Heidelberg (2008).
- [20] S. Seltzer and M. Berger, Atomic Data and Nuclear Data Tables, **35**, (1986) 345.
- [21] S. Seltzer and M. Berger, Nuc. Instr. and Meth., **B12**, (1985) 95.
- [22] B. Rossi, "High Energy Particles", Prentice-Hall, Inc., Englewood Cliffs, NJ (1952).
- [23] B. Dolgoshein, Nucl. Inst. and Meth., **A326**, (1993) 434.

- [24] M. Cherry *et al.* Phys. Rev. **D10** (1974).
- [25] O. Klein, Y. Nishina, Z. Phys. 52 (1929) 83.
- [26] P. Marmier, E. Sheldon, "Physics of Nuclei and Particles" Vol.I, Academic Press, New York (1969).
- [27] V. Kartvelishvilia and ATLAS Collaboration, Nucl. Phys. B, Vol. 172, (2007) 208.
- [28] J. E. Moyal, "Theory of Ionizational Fluctuations", Ser. 7, Vol. 46, No. 374 (1955).
- [29] Claus Grupen, "Teilchendetektoren", BI-Wissenschaftsverlag, Siegen (1993).
- [30] U. Amaldi, Physica Scripta 23 (1981) 409.
- [31] W. R. Nelson *et al.*, SLAC-265 (1985).
- [32] E. Longo, I. Sestili, Nucl. Inst. and Meth. 128 (1985) 283.
- [33] C. Adler, private communication,
<http://www.physi.uni-heidelberg.de/~adler/TRD/Radiation%20Length/Radiationlength.pdf>
- [34] Y. S. Tsai, Rev. Mod. Phys. **46**, (1974) 815.
- [35] S. Eidelman *et al.*, Phys Lett. **B592**, (2004) 1.
- [36] The ALICE Collaboration, Technical Design Report, CERN/LHCC 2001-021, (2001).
- [37] W. Sommer, Ph.D. thesis, Institut für Kernphysik, Frankfurt (2008).
- [38] Anton Andronic, private communication,
<http://www-linux.gsi.de/~andronic/trd/tests/nov07/>.
- [39] The ALICE Offline Project AliRoot,
<http://aliceinfo.cern.ch/Offline/>.
- [40] Univ. Doz. DI. Dr. M. Krammer, lecture, "Detektoren in der Hochenergiephysik", Institut für Hochenergiephysik der ÖAW, Wien (2005)
- [41] L. Durieu, O. Ferrando, J.-Y. Hémerly, J. -P. Riinaud, B. Williams, "The CERN PS east area in the LHC era", CERN (1998),
<http://accelconf.web.cern.ch/accelconf/pac97/papers/pdf/8P008.PDF>.
- [42] ROOT Homepage,
<http://root.cern.ch/root/>.
- [43] Virtual Monte Carlo homepage,
<http://root.cern.ch/root/vmc/VirtualMC.html>.
- [44] The ALICE Offline Bible, Version 0.00 (Rev. 406).
- [45] David Emschermann, private communication,
<http://www.physi.uni-heidelberg.de/~demscher>.

- [46] A. Andronic, private communication.
- [47] GEANT3 manual,
http://wwwasdoc.web.cern.ch/wwwasdoc/geant_html3/geantall.html.
- [48] CERN homepage,
<http://www.cern.ch>.
- [49] <http://doc.cern.ch//archive/electronic/cern/others/multimedia/poster/poster-2004-004.pdf>
- [50] ALICE Collaboration, J. Phys. G: Nucl. Part. Phys. **32** (2006), 1295-2040.
- [51] ALICE Collaboration, J. Phys. G: Nucl. Part. Phys. **30** (2004), 1517-1763.
- [52] K. Pearson, 1904. "On the Theory of Contingency and Its Relation to Association and Normal Correlation", Drapers' Co. Memoirs, Biometric Series No. 1, London (1904).
- [53] N. Gagunashvili, "Test for comparison of weighted and unweighted histograms". Statistical Problems in Particle Physics, Astrophysics and Cosmology, Proceedings of PHYSTAT05, Oxford, UK, Imperial College Press, London, **43** (2006).
- [54] <http://www.faes.de/Basis/Basis-Statistik/Basis-Statistik-Chi-Quad-Test/Basis-Statistik-Chi-Quad-Tabel/basis-statistik-chi-quad-tabel.html>

Acknowledgements

At this point I would like to express my gratitude to the people who made this thesis possible and supported me:

I'm deeply grateful to my supervisor Dr. Kai Schweda who gave me the unique opportunity to work in such an interesting field such as high energy physics with the ALICE TRD detector. Due to his knowledge and experience I profited from many fruitful discussions about physics with him during my year as diploma student. He always listened patiently to my questions and problems and was always interested in the current status of my work. I'm thankful that Prof. Dr. Hans-Christian Schultz-Coulon agreed to be the second corrector of this thesis.

Dr. C. Yvonne Pachmayer I'd like to thank for reading my thesis to reduce mistakes and her suggestions which improved this thesis.

Dr. Anton Andronic from GSI in Darmstadt I thank for providing me information about many important details concerning the Testbeam 2007 at CERN and for problem resolving discussions.

Prof. Dr. Johanna Stachel as well as all members of the ALICE TRD group in Heidelberg I'd like to thank for useful hints during my talks about my work in our meetings.

Concerning solving any kind of computer and software problems special thanks go to Prof. Dr. Christoph Blume from the University of Frankfurt, Dr. Sylwester Radomski, Dr. Minjung Kweon, Dipl. Phys. Dirk Krumbhorn and to Dipl. Phys. Clemens Haltebourg.

Finally, I want to thank my parents as well as my girlfriend for their encouragement and support, which made my studies possible.

This work has been supported by the Helmholtz Association under contract number VH-NG-147 and and the Federal Ministry of Education and Research under promotional reference 06HD197D.

Erklärung

Ich versichere, dass ich diese Arbeit selbständig verfasst und keine anderen als die angegebenen Quellen und Hilfsmittel benutzt habe.

Heidelberg, den 31.01.2009

.....
Robert Grajcarek